Stellar Population Trends in S0 Galaxies

Leslie Prochaska Chamberlain

A dissertation submitted to the faculty of the University of North Carolina at Chapel Hill in partial fulfillment of the requirements for the degree of Doctor of Philosophy in the Department of Physics & Astronomy.

Chapel Hill
2009

Approved by:

James A. Rose, Advisor
Bruce W. Carney, Reader
Chris Clemens, Reader
Arthur E. Champagne, Reader
Sheila Kannappan, Reader

ABSTRACT

LESLIE PROCHASKA CHAMBERLAIN: Stellar Population Trends in S0 Galaxies
(Under the Direction of James A. Rose)

We present stellar population age and metallicity trends for a sample of fifty-nine S0 galaxies based on optical SDSS and NIR J & H photometry. When combined with optical g and r passband imaging data from the SDSS archive and stellar population models, we calculate radial age and metallicity gradients out to at least 5 effective radii for most of the galaxies in our sample. The sample covers a range in stellar mass, light concentration, and environmental density. We find an average central light-weighted age of $\sim$3 Gyr and central metallicity [Z/H]$\sim$0.5 dex. Almost all galaxies show a negative metallicity gradient from the center out, with an average value of Δ[Z/H]/Δlog(r) = -0.5. We observe an increase in age with radius for 41% of our sample, a decrease for 17%, and small change for 42%. Galaxies with both lower mass and lower concentration have younger light-weighted ages than other galaxies in our sample. For 20% of our sample, the light-weighted ages of the outer regions are greater than 10 Gyr. In order to understand if the old regions of these galaxies are dominated by a disk component, we have performed galactic component decompositions of a sub-sample of 22 S0 galaxies. The sub-sample focuses on the S0 galaxies with a substantially old outer regions and includes additional galaxies for comparison. Our decomposition routine uses a generalized Sersic component for the bulge and an exponential profile for the disk. Nearly all galaxies that were decomposed show outer regions that are disk dominated. Our results indicate that the disk component is responsible for the old ages in the outer regions. The ages of the disks of these galaxies place a constraint on models of hierarchical merging, requiring no major merger to have occurred for these galaxies in a very long time (since z $\sim$ 2, using an age of 10 Gyr). For the sub-sample of galaxies that we analyze with profile decompositions, we derive a mean

n of 2.0 $\pm$ 0.6, a mean ratio of bulge and disk scale lengths, r_e/h, of 0.41 $\pm$ 0.40, and a mean $(B/D)_{tot}$ of 1.8 $\pm$ 3.1. We find a correlation between n and $(B/D)_{tot}$ such that galaxies with larger n are more bulge dominated.

In Memory of **Jack R. Blann:** my beloved grandfather who has provided me with abounding support and inspiration.

ACKNOWLEDGMENTS

To my mother, **Bette,** who deserves my greatest gratitude. You nurtured my curiosity as a child, provided comfort and encouragement whenever it was needed, and always understood my dreams. The values you have taught me are the core or my goals. Thank you for being my confidant, role model, and best friend.

To my husband and soul-mate, **Charlie,** for teaching me to not take myself so seriously but to enjoy everyday to its fullest. I am grateful for the hours of laughter we share. Thank you for being my composer, butler, counselor, and chauffeur during the long days of graduate school, and most importantly for your willingness to share my dreams.

To my grandmother, **Fafa (Lavonne),** for all of the love and support you have given me. You are an exceptional woman leading an exemplary life. I aspire to share your generous, loving, and charismatic nature. I am grateful for the many conversations that we share - without those, graduate school would have been much more draining!

To my brothers, **Drew and David,** for inspiring me to live wholly, with love and conviction in everything I do. I admire your strength, determination, and wit. You make me proud to be a Prochaska.

To **Jim.** Wow, it's been a long, but terrific, journey! Thank you for pushing me to do things I didn't know I could do, encouraging rest and relaxation, and allowing me the freedom to learn in my own style. I appreciate your patience when I struggled and your excitement for the results when I did not. I admire your passion for science, your commitment to your family, and your enthusiasm for life.

To **Stephane,** for your exceptional commitment not only to my project, but to

my career as a whole. I was fortunate to have two remarkable advisors for my thesis project and I owe so much of this to you. Thank you for the many good times in La Palma, Kingston, and Hawaii, for the thoughtful discussions, and for the energy you consistently bring into my research.

To my new family, **Sue, Charles, Katie, Ian, and Thomas,** for believing in me and making my days off absolutely enjoyable. My productivity is always at its highest after a nice visit at the lake.

To **Peter,** for showing me the way and always believing that I can get there.

Thank you to everyone who has made this PhD possible: Sheila, Jesse, Mike, Joel, Lorenza, Matt, Rachel, Hell's Kitchen ladies, Capoeira Brasil, Chapel Hill coffee shops, running trails, UCCH, Meagan, Leandra, Bonnie, Sherry, and Rachel.

May the words of my mouth and the meditation of my heart be acceptable in your sight, O Lord, my rock and my Redeemer. Psalm 19:14

Leslie Prochaska Chamberlain.

October 29, 2009

CONTENTS

LIST OF TABLES

LIST OF FIGURES

LIST OF ABBREVIATIONS

NED	NASA/IPAC Extragalactic Database
IR	Infrared
NIR	Near-infrared
SP	Stellar Population
HST	Hubble Space Telescope
SDSS	Sloan Digital Sky Survey
PSF	Point Spread Function
FWHM	Full Width at Half Maximum
SB	Surface Brightness
SSP	Simple Stellar Population
BC03	Bruzual & Charlot (2003)
TP-AGB	Thermal-Pulsating Asymptotic Giant Branch
OOPS	Old Outer Population S0
K-S	Kolmogorov-Smirnov
SFH	Star Formation History
B/D	Bulge-to-Disk
M09	McDonald et al. (2009a)

LIST OF SYMBOLS

R_e	Total effective radius
z	redshift
C_{28}	Concentration parameter
$M_\odot$	Solar mass
τ	Time constant
n	Sersic index
r_e/h	Ratio of bulge and disk scale lengths
$(B/D)_{tot}$	Bulge-to-disk ratio for total radial range
$(B/D)_{bin}$	Bulge-to-disk ratio for a limited radial range
r_e	Bulge effective radius
μ_e	Surface brightness in magnitudes
μ_o	Central surface brightness in magnitudes
h	Disk scale length
χ^2	Reduced χ^2 merit function

Chapter 1

Introduction

Many processes of galaxy formation have been proposed over the years ranging from the classic models of monolithic collapse (Eggen et al 1962, Larson 1975) and hierarchical merging (Toomre and Toomre 1972, White & Ress 1978, Kauffman et al 1993) to secondary processes such as the secular formation of the bulge (Kormendy & Kennicutt 2004) and gas stripping in the disk (Quilis et al. 2000; Kronberger et al. 2008). Which mechanisms are most important in forming galaxies along the Hubble sequence is a key question in galaxy evolution studies. In the classical morphological sequence, S0 galaxies occupy an intermediate position between elliptical and spiral galaxies (Hubble 1936). The combination of the morphological position and relatively smooth disks of S0 galaxies provides us with a unique opportunity to study galaxy evolution. In this thesis, we use optical and near-IR colors to explore the age and metallicity gradients in S0 galaxies and then use a profile fitting technique to examine which component, the disk or the bulge, is contributing to the age and metallicity along the galaxy.

We begin with an overview of galaxy formation theories, a summary of current views on the formation of S0 galaxies, and a description of our observational techniques. In chapter 2, we present a study of the radial trends in stellar populations that will soon be submitted to the astronomical journal for publication. Chapter 3 presents a study of bulge and disk decompositions and their relation with stellar pop-

ulation parameters. This study is also expected to be submitted for publication. In chapter 4, we summarize the results from both studies and discuss the implications of the results on galaxy evolution. In chapter 5, we outline future work.

1.1 Galaxy Formation Theories

There are 2 major classes of classic galaxy formation theories. The simplest models have ellipticals and spheroids forming at high redshift in a rapid collapse and monolithic burst of star formation (Eggen et al 1962, Larson 1975). In this "monolithic collapse" scenario, the stellar populations of spheroids age passively, with no further star formation. Observations in support of monolithic collapse are those suggesting homogeneity in elliptical galaxies, such as the small dispersion observed in the color-luminosity relation in the Coma cluster Bower et al. (1992). Alternatively, observations of nearby elliptical galaxies indicate that recent star formation is taking place in these galaxies, thereby rejecting the idea that elliptical galaxies were formed in a monolithic collapse with no further star formation (Schade et al. 1999; Huang & Gu 2009).

More recently, formation models have focused on the more complex star formation histories resulting from hierarchical growth (White & Ress 1978, Kauffman et al 1993). In this model, structures form in a bottom up, hierarchical manner by which smaller fragments merge together to form more massive systems. According to the hierarchical paradigm, most stars are thought to be born in disks while stellar spheroids arise as the remnants of subsequent merger events (Abadi et al. 2003; Mihos & Hernquist 1996). Gradual accretion of cooled gas from the hot gaseous halo will result in a newly formed disk around the spheroid. In this scenario, galaxy morphology can thus fluctuate between being disk and spheroid dominated (Scannapieco & Tissera 2003; Abadi et al. 2003).

The hierarchical merging model has been very successful at reproducing observations on large scales. However, a number of issues remain to be resolved at the

galaxy-scale regime. (Primack 2007, Moore et al 1999). These concerns, such as the "anti-hierarchical" observations of younger ages for low mass galaxies, are explained in modern theories of hierarchical merging by the use of feedback mechanisms (De Lucia et al. 2006) or even as a natural consequence of the bottom-up cluster process (Neistein et al. 2006). As well, concerns of too few disk-dominated systems in hierarchical predictions compared to observations can be ameliorated by accounting for the role of gas in mergers (Hopkins et al. 2009).

A robust prediction of both of the above classic models of galaxy formation is that the stellar populations in the spheroids of disk galaxies will lack recent star formation. Detailed observations, however, show galaxies containing circumnuclear star formation in galactic bulges (Benedict et al. 2002; Jogee et al. 2002; Buta et al. 2000; Maoz et al. 2001) (also see review by Kormendy & Kennicutt (2004)). An alternative origin for stellar bulges, particularly the small bulges of late-type spirals, has been outlined in several internal secular evolution models that propose the growth of bulges from instabilities of preexisting disks which may cause star formation in the central regions (Sellwood 1981; Pfenniger & Friedli 1991; Athanassoula 2003). Secular evolution may also be caused by external drivers such as minor mergers. Observed correlations of blue-centered galaxies with morphological peculiarities suggest the importance of mergers in in-situ bulge growth (Kannappan et al. 2004) and simulations outline the plausibility of bulge growth through minor accretion (Weinzirl et al. 2009; Scannapieco & Tissera 2003; Eliche-Moral et al. 2005). Supporting both internal and external secular evolution theories are observations of these so called "pseudobulges" retaining a memory of their disky origin, such as having flatter shapes than classical bulges (Kormendy 1993; Carollo 1999; Fisher & Drory 2008) and a correlation of bulge and disk scalengths (Courteau et al. 1996; MacArthur et al. 2003; Barway et al. 2007).

The disk of the galaxy can continue to change after the initial assembly of the galaxy has occurred. Many recent theories outline the removal of gas and subsequent halting of star formation in the disk through mechanisms such as: interactions with other galaxies (Icke 1985; Barnes 2002), harassment (Moore et al. 1996), ram pressure

and/or viscous stripping (Quilis et al. 2000; Kronberger et al. 2008), strangulation (Kawata & Mulchaey 2008), or cluster tidal effects (Byrd & Valtonen 1990). Kenney et al. (2008) studied the distribution of HII regions of two companion galaxies in the Virgo cluster, M86 and NGC4438, and found evidence for both a collision between the two galaxies and a truncation of star formation at 30% of the optical radius, thus supporting the role of gravitational interactions in transforming galaxies. The models of Hernquist & Mihos (1995) show that a 10 to 1 merger can drive up to 50% of the disk gas in to the center of the galaxy, thereby increasing star formation in the center and suppressing it in the disk.

A picture is now being developed where each of the above outlined formation scenarios is likely to play some role in galaxy formation and evolution. To decipher the relative importance of these, observers need to measure physical, dynamical, and stellar population properties of galaxies from which to compare realistic simulations.

1.2 S0 Galaxies

S0 galaxies are a particular class of disk galaxies that lack observed spiral structure. This class offers a unique opportunity to study disk formation from both the observational perspective and the galaxy evolution perspective. Observationally, they are relatively simple systems to study. In general, the light from their disks is significantly less contaminated by the knots of young star formation and dust that overwhelms the light of spiral galaxies. Also, the relatively smooth light distributions of a large fraction of S0 galaxies enable robust surface brightness fitting of their photometric components.

From the galaxy evolution side, S0 galaxies lie in a unique morphological position between gas-rich spiral galaxies and gas-poor ellipticals. Observational studies of S0 galaxies can broaden our understanding on three scales: (1) how this class of galaxies has formed; is nature or nurture more important? (2) the formation of galaxies in general; is the Hubble sequence a continuous sequence from elliptical to late-type spirals? and (3) the cosmological structure; the rate of evolution of S0 galaxies can

be used to constrain formation scenarios.

Popular theories suggest that at least a class of S0 galaxies are by-products of secondary events in galaxy formation rather than products of some particular set of initial conditions. In particular, S0s are thought to originate as spiral galaxies that have had their star formation halted through a gas removal mechanism (Icke 1985; Moore et al. 1996; Boselli et al. 2008; Quilis et al. 2000; Byrd & Valtonen 1990). The observational evidence of an increasing fraction of S0-to-spiral galaxies in local clusters as compared to higher redshift clusters certainly supports this idea (Butcher & Oemler 1978; Dressler & Gunn 1983). Additionally, Barr et al. (2007) studied globular cluster frequency in S0 galaxies and found results consistent with the hypothesis that these S0 galaxies have formed from spirals. However, our understanding of which mechanisms are most important in the possible morphological transformation of spiral into S0 galaxies is poor.

An alternate view is that S0s are more closely related to ellipticals. This view is supported by observations of the close similarities between elliptical and S0s, in particular high mass S0s, in their stellar populations, gas content, and location on the fundamental plane (Jorgensen et al. 1996). Most likely, multiple evolutionary paths exist for the formation of these systems. In fact, recent work suggests a difference in star formation histories for bright and faint S0s, suggesting that only faint S0s have descended from spirals (Jorgensen & Franx 1994; Barway et al. 2007; Bedregal et al. 2008).

1.3 Testing Model Predictions With Observations

The study of extragalactic astronomy beyond our local group of galaxies is based on light that has been integrated along a given line of sight, reddened by the dust that it travels through, and smeared by atmospheric turbulence. From this light, we strive to learn how galaxies have formed and evolved. There are a wide variety of techniques used to accomplish this goal, ranging from dynamical to stellar population studies and

from studies of distant galaxies at large look-back times to local galaxies containing fossil records. In my thesis work I have focused on analyzing the stellar populations and physical characteristics of nearby S0 galaxies. We now describe how stellar populations and physical characteristics can increase our understanding of galaxy formation and then outline our observational technique.

The dynamical events that lead to the production of S0 galaxies produce imprints on the galaxy's star formation history. Our goal is to study the radial stellar population (hereafter, SP) gradients, which are like a fossil record, to piece together the galaxies' formation history and distinguish between possible scenarios for galaxy formation. Because the light that we observe is an integration of many stars, the age and metallicity that we measure is a light-weighted mean age and metallicity of all stars contributing to the light. Trends of light-weighted mean age and metallicity with radius in disk galaxies may therefore reflect the transition from bulge dominated light to disk dominated light if the stars in the two components are of a different age. As discussed above, the hierarchical paradigm predicts that most stars are born in disks while stellar spheroids arise as the remnants of merger events (Abadi et al. 2003). Any remaining accretion of cooled gas will create a disk around the spheroid. Under this formation scenario, the stars in the spheroids would thus be older than those in the disk, resulting in decreasing ages with radius. Trends of age with radius may also reflect the formation of individual components. For example, most hierarchical models of disk formation predict an inside-out accretion of disk gas from the hot gaseous halo, again creating ages that decrease outward in the galaxy (Fall & Efstathiou 1980). Alternatively, the model of the formation of a disk from the dissipational collapse of gas as simulated by Roškar et al. (2008) predicts that the outer region of the galaxy will have an increase in light-weighted age with radius.

Secondary events in galaxy formation also affect radial trends with age. Many of the theories predicting the transformation from a spiral to an S0 galaxy, as discussed in § 1.2, predict a resultant trend of increasing light-weighted age with radius caused by gas preferentially removed in the outer regions and sometimes an enhancement of

star formation in the central regions (Quilis et al. 2000; Kawata & Mulchaey 2008; Kronberger et al. 2008).

Radial trends in metallicity are also expected to vary depending on the formation mechanism. In the simulations of Kobayashi (2004), galaxies that form monolithically are found to have steeper metallicity gradients than those undergoing major mergers. However, within the framework of hierarchical merging, a central starburst could strengthen a negative metallicity gradient (Barnes & Hernquist 1991).

Another method to increase our knowledge of galaxy formation is to study the relation between the SPs and global properties of these systems, such as mass and light concentration, and their environment. Strong tidal interactions and major mergers between galaxies are more effective in low density environments as opposed to within rich clusters, while galaxy evolution in clusters may be driven by interactions with the intracluster medium. The mechanisms of various environments may leave different imprints on the galaxies age and metallicity trends. The mass of a galaxy is also closely tied to its star formation history. Observations of older SPs in S0 galaxies with higher velocity dispersion (an indication of higher mass) may place requirements of feedback (De Lucia et al. 2006) on hierarchical models which originally predicted the reverse trend (Navarro et al. 1995).

In summary, we find that different physical processes are expected to lead to different radial trends with age and metallicity. We can explore the evolutionary paths of S0s by studying the age and metallicity gradients of these galaxies.

Our analysis of radial SP trends is based on the photometric images of nearby S0 galaxies. Our database consists of deep H and/or J images of 59 S0 galaxies covering a representative range of mass, light concentrations, and environments. In order to interpret the light emitted from galaxies, we use an evolutionary population synthesis technique. In this approach, colors inferred from stellar population synthesis models covering a range in age and chemical composition are compared to the observed colors to derive the stellar population parameters of that galaxy, namely the light-weighted mean ages and metallicities. The combination of a primarily age sensitive color (such

as g-r) with a primarily metallicity sensitive color (such as r-H) provides a better separation in age and metallicity than using optical colors alone. The simple stellar population (hereafter, SSP) models that we use for our analysis predict the evolution in colors of a coeval population of stars with the same chemical composition and specified initial mass function. While this is clearly an over-simplification of the actual star formation histories in S0 galaxies, it represents a straightforward way to obtain a *light-weighted* age and metallicity. Radial age and metallicity gradients out to at least 5 effective radii are derived from comparison of the observed g-r and r-H (and/or r-J) colors to SSP models of Bruzual & Charlot (2003).

Once ages and metallicities are derived for the stellar populations in galaxies, it is important to understand which physical component is contributing to the majority of the light. The light distribution in S0 galaxies is often separated into a bulge and disk component, which are assumed to be physically and dynamically distinct. The disk component is flat and governed by rotational dynamics. The spherical bulge component is dynamically a much hotter system than the disk. Separating both components using only the surface photometry of a galaxy has been a long standing problem. Many different decomposition techniques can be found in the literature. Most frequently the disk is fit with an exponential function and the bulge with either a general Sersic, or a more special case of $r^{1/4}$. The analysis presented here uses a generalized Sersic component for the 'bulge' and an exponential profile for the 'disk'.

Chapter 2

Stellar Population Gradients in S0 Galaxies

L. C. Prochaska Chamberlain

Department of Physics and Astronomy, CB 3255, University of North Carolina, Chapel Hill, NC 27599

chaska@physics.unc.edu

Stéphane Courteau

Department of Physics, Engineering Physics and Astronomy, Queens University, Kingston, ON, Canada

courteau@astro.queensu.ca

Mike McDonald

University of Maryland, College Park, MD

mcdonald@astro.umd.edu

James A. Rose

Department of Physics and Astronomy, CB 3255, University of North Carolina, Chapel Hill, NC 27599

jim@physics.unc.edu

ABSTRACT

We present stellar population age and metallicity trends for a sample of fifty-nine S0 galaxies based on optical SDSS and NIR J & H photometry. When combined with optical g and r passband imaging data from the SDSS archive and stellar population models, we calculate radial age and metallicity gradients out to at least 5 effective radii for most of the galaxies in our sample. The sample covers a range in stellar mass, light concentration, and environmental density. We find an average central light-weighted age of $\sim$3 Gyr and central metallicity [Z/H]$\sim$0.5 dex. Almost all galaxies show a negative metallicity gradient from the center out, with an average value of Δ[Z/H]/Δlog(r) = -0.5. However, we observe an increase in light-weighted age with radius for 41% of our sample, a decrease for 17%, and little change for 42%. For 20% of our sample, the light-weighted age of the outer region is greater than 10 Gyr. Galaxies with both lower mass and lower concentration have younger light-weighted ages than other galaxies in our sample.

2.1 Introduction

The unique status of S0 galaxies between gas-poor and gas-rich galaxies makes their origin a key ingredient of galaxy formation and evolution models. Numerous hypotheses suggest that at least a class of S0 galaxies are by-products of secondary events in galaxy formation that transform spiral galaxies into S0 galaxies, rather than products specific initial conditions (Icke 1985; Moore et al. 1996; Boselli et al. 2008; Quilis et al. 2000; Byrd & Valtonen 1990). These theories involve the removal of gas and subsequent halting of star formation and can include the following secondary formation mechanisms: interactions with other galaxies (Icke 1985; Barnes 2002), harassment (Moore et al. 1996), ram pressure and/or viscous stripping (Quilis et al. 2000; Kronberger et al. 2008), strangulation (Kawata & Mulchaey 2008), and cluster tidal effects (Byrd & Valtonen 1990). Observational evidence for a higher fraction of S0-to-spiral galaxies in local clusters as compared to higher redshift clusters certainly

supports the idea that S0 galaxies are primarily created through evolutionary processes (Butcher & Oemler 1978; Dressler & Gunn 1983). However, obstacles to theories of a simple transformation from a spiral to a lenticular galaxy do exist. For example, the bulge-to-disk ratios of S0 galaxies appear to be on average larger than those of spirals in all density regimes (Dressler 1980), thus creating problems for a straightforward disk-quenching scenario, although not for other scenarios such as merging. The dichotomy between massive and low mass S0s suggests different formation scenarios for the two mass groups (van den Bergh 1994; Bedregal et al. 2008). In this paper we study the stellar populations in S0 galaxies to better constrain their possible formation processes.

Observations of radial stellar population (hereafter, SP) gradients in S0 galaxies may help to distinguish between possible scenarios for S0 galaxy formation, since the dynamical events that lead to the production of S0s may produce or erase imprints on the galaxy's star formation history. For example, hierarchical models of galaxy formation predict an inside-out accretion of disk gas from the hot gaseous halo, resulting in ages that decrease outward in the galaxy (Fall & Efstathiou 1980). On the other hand, secondary formation events, such as the mechanisms outlined above that transform a spiral galaxy into an S0, could alter this trend of age with radius.

SP trends in the inner regions of S0 galaxies yield a broad picture. Peletier et al. (1999) examined the bulges of S0 galaxies using Hubble Space Telescope images and found an average bulge light-weighted age of 9 Gyr, with only a small spread in age around that mean value. Balcells & Peletier (1994) determined that the bulges of S0s are bluer than ellipticals of similar mass, and attribute this to metallicity differences. There is also literature documenting radial trends in ages in the inner region and bulges of S0s. Sil'chenko (2006) found from spectroscopic analysis that the nuclear regions of S0 galaxies are on average younger than the bulges in any type of environment. Using Hβ line strengths of nine edge-on galaxies, Fisher et al. (1996) suggested that the outer parts of S0 bulges (r $>$ 1 R_e) are dominated by stars that are older and more metal-poor than in their centers. Serra et al. (2008) also found younger central stellar populations for HI-poor S0 galaxies, but not for low mass, HI-rich galaxies. Most

theories detailing the transformation from spiral to S0 galaxies predict a resulting central gas concentration that leads to a young stellar population in the center of the S0 remnant (Icke 1985; Moore et al. 1996; Kronberger et al. 2008), consistent with spectroscopic studies. Although Peletier et al. (1999) found redder colors in the very central regions of S0s compared to further out, they attributed this to dust effects (which more strongly affect photometric colors than spectroscopic indices), as opposed to age differences.

Less is known about the SP trends in S0 galaxies at larger radii. Caldwell (1983) and Bothun & Gregg (1990) proposed that a population of stars in the disks of S0 galaxies is younger than the population in bulges. These conclusions, however, are not based on SP modeling, and hence are subject to an age-metallicity degeneracy (e.g., Worthey 1994; MacArthur et al. 2004). Peletier & Balcells (1996) and Mehlert et al. (2003) found color differences between bulges and inner disks of S0s that are significantly smaller than those reported in Bothun & Gregg (1990). Finally, Fisher et al. (1996) found that the centers of S0s are dominated by populations younger than the disk. Peletier & Balcells (1996) note that this difference in age trends may be due to the greater radial coverage, in r/Re, of the Fisher et al. (1996) sample compared to theirs. More recently, a few detailed studies have been carried out for the SP of individual S0 galaxies. While Norris et al. (2006) find that the bulge of the S0 NGC3115 is older than the disk, Tikhonov et al. (2003) find that in the nearby dwarf S0 NGC404, the bulge is younger than the disk. In addition, MacArthur et al. (2004) observed a sample spanning all Hubble types out to 1.5 to 5.0 disk scale lengths and found that four S0 galaxies have an increase in age for increasing radius, i.e. a positive age gradient. They found different trends for galaxies of different Hubble types. The conclusion that emerges is that larger samples with photometry extending beyond a few effective radii are required to firm up SP trends and ultimately enable general conclusions about S0 formation.

In addition to establishing radial SP gradients in S0 galaxies, one must assess whether the SP gradients are linked to global properties such as the total galaxy stellar

mass, the central light concentration, and the environment surrounding the galaxy. In regard to environment, the correlation between the fraction of star forming galaxies and local environmental density has been known since Hubble & Humason (1931), and is perhaps the clearest signature of the effect of environment on the formation and evolution of galaxies. The idea of an environmental dependence on galaxy evolution is additionally supported by the observed lack of evolution of the fraction of spheroidal to disk systems for field galaxies (Griffiths et al. 1994) as compared to cluster galaxies (Butcher & Oemler 1978; Dressler & Gunn 1983; Postman et al. 2005). Strong tidal interactions and major mergers between galaxies are more effective in the low velocity dispersion group environment as opposed to within rich clusters. On the other hand, galaxy evolution in clusters may be driven by ram pressure from the intracluster medium (Gunn & Gott 1972; Boselli & Gavazzi 2006 and references therein) and/or through frequent impulsive gravitational interactions, i.e., "harassment" (Moore et al. 1996, 1998). The different mechanisms that may transform gas-rich disk galaxies into quiescent S0s may also leave different imprints on the radial star formation histories of S0s that depend on environment.

The degree to which light is concentrated towards the center of the galaxy is also connected to a galaxy's formation history. Secondary galaxy evolution processes are believed capable of increasing the size of the central region either through secular build-up or through accretion of satellites (Kormendy & Kennicutt 2004). On the other hand, the relative size of the central component, or the bulge, may influence the outcome of galaxy formation processes, such as those transforming spiral galaxies. For example, harassment preferentially selects bulge-dominated galaxies to be stripped of their spiral structure and turned to S0s, since disk-dominated galaxies will instead be shredded down to a dwarf system (Moore et al. 1996). Either way, the light concentration of the galaxy is closely connected with galaxy evolution processes. Previous studies have related galaxy formation to concentration. McDonald et al. (2009b) find a lack of low surface brightness galaxies with high concentration as well as high surface brightness galaxies with low concentration. They suggest from these results the pos-

sibility that galaxies with high concentration can only form through major mergers. Other studies have related the size of the bulge and the bulge-to-disk ratio, which is related to concentration, to the evolution of S0 galaxies. Balcells & Peletier (1994) studied the color gradients of 45 early-type disk galaxies and found that galaxies with larger bulges are redder and also find larger color gradients for smaller bulges. However, at high redshift ($0.73 < z < 1.04$), Koo et al. (2005) found from a study of 86 galaxies with a range of Hubble type that the change in color between the bulge and disk is not related to the bulge-to-disk ratio. They also find no difference in bulge colors between disk-dominated galaxies and bulge-dominated galaxies, suggesting that B/D ratio has little correlation with stellar populations at this redshift.

Finally, the mass of a galaxy is closely tied to its formation history. Hierarchical assembly predicts that larger galaxy dark matter halos are formed through mergers later than smaller halos (Navarro et al. 1995). However, semi-analytic models can produce "anti-hierarchical" star formation histories in a ΛCDM universe despite the hierarchical assembly of these galaxies (De Lucia et al. 2006). As well, Neistein et al. (2006) derived anti-hierarchical evolution analytically showing it can be a natural outcome of bottom-up clustering. Such anti-hierarchical evolution is more consistent with actual observational trends of stellar populations with galaxy mass for all Hubble types, including S0s (MacArthur et al. 2004). For example, an increasing fraction of S0 galaxies with recent star formation has been observed for decreasing luminosities (an indicator of stellar mass) (Poggianti et al. 2001; Balcells & Peletier 1994). Additionally, a correlation of older stellar populations in S0 galaxies with higher velocity dispersion (an indicator of dynamic mass) has been observed (Bedregal et al. 2008; Sil'chenko 2006; Mehlert et al. 2003). These studies support different star formation histories for high and low mass S0 galaxies, but have largely focused on the stellar populations in the inner regions of galaxies.

Despite recent progress, observational studies of radial SP trends in S0 galaxies as a function of the global properties of mass, concentration, and environment are still open-ended and have seldom explored the outer regions of S0 galaxies. Instead,

efforts have focused on age and chemical composition determinations within one effective radius. In this paper we use deep optical-IR color gradients to explore age and metallicity gradients in S0 galaxies out to typically 5 R_e, and with a large enough sample to cover a substantial range in galaxy mass, light concentration, and local environment. The focus of this paper is largely on empirical radial trends in stellar populations; separate bulge and disk trends that result from model decompositions of the galaxy image will be presented in a forthcoming publication. Our S0 galaxy sample is presented in § 2.2, while our observations and data reduction techniques are discussed in § 2.3 and § 2.4, respectively. Measurements of global galaxy properties are presented in § 2.5 and the stellar population models are described in § 2.6. Our results on age and chemical composition trends in S0 galaxies are presented in § 2.7, while the implications of our results are discussed in § 2.8. A summary of our conclusions is presented in § 2.9.

Table 2.1: UH 2.2-m Observations

Galaxy	T(sec)[1]	date	Z.P.(mag)[2]	σ [3]	NS[4]
UGC04330J	480	April 2007	-1.916	0.224	10
UGC04596H	480	March 2008	-1.805	0.004	3
UGC04599J	480	April 2007	-1.713	0.029	11
UGC04631J	480	April 2007	-1.707	0.037	7
UGC04639J	480	April 2007	-1.628	0.621	9
UGC04737H	480	March 2008	-1.819	0.251	10
UGC04869H	480	March 2008	-1.853	—	0
UGC04901J	480	April 2007	-1.596	—	0
UGC04910J	480	April 2007	-1.579	0.263	7
UGC04916J	480	April 2007	-1.694	0.084	7
UGC04989J	480	April 2007	-1.729	0.040	8
UGC05075J	480	April 2007	-1.777	0.046	8
UGC05094H	480	March 2008	-1.851	—	0

Table 2.1: UH 2.2-m Observations

Galaxy	T(sec)[1]	date	Z.P.(mag)[2]	σ [3]	NS[4]
UGC05182H	480	March 2008	-1.775	—	0
UGC05403H	480	March 2008	-1.844	0.059	4
UGC05419H	480	March 2008	-1.864	—	0
UGC05503J	960	April 2007	-1.927	—	0
UGC05568H	480	March 2008	-1.939	—	0
UGC05766H	480	March 2008	-1.939	—	0
UGC05952J	480	April 2007	-1.739	—	0
UGC08800J	480	April 2007	-1.454	0.090	6
UGC08886H	480	April 2007	-1.968	—	0
UGC08986J	480	April 2007	-1.676	—	0
UGC08997J	480	April 2007	-1.528	0.001	7
UGC09003J	480	April 2007	-2.020	—	0
UGC09087J	480	April 2007	-1.558	—	0
UGC09156J	480	April 2007	-1.587	—	0
UGC09212J	480	April 2007	-1.615	—-	0
UGC09280J	480	April 2007	-1.556	—	0
UGC09280H	480	April 2007	-1.977	—	0
UGC09321H	480	April 2007	-1.902	0.072	4
UGC09387J	480	April 2007	-1.584	—	0
UGC09400J	480	April 2007	-1.577	0.060	9
UGC09400H	480	April 2007	-1.898	0.472	11
UGC09434H	480	April 2007	-1.899	—	0
UGC09514H	480	April 2007	-1.867	0.026	8
UGC09592H	480	April 2007	-1.933	—	0
UGC09693H	480	April 2007	-1.907	—	0
UGC09705J	480	April 2007	-1.622	—	0

Table 2.1: UH 2.2-m Observations

Galaxy	T(sec)[1]	date	Z.P.(mag)[2]	σ [3]	NS[4]
UGC09705H	480	April 2007	-1.899	—	0
UGC09713J	480	April 2007	-1.613	0.168	5
UGC09713H	480	April 2007	-1.681	0.129	3
UGC09939H	480	April 2007	-1.867	—	0
UGC09967J	480	April 2007	-1.626	0.150	7
UGC09967H	480	April 2007	-1.965	0.067	10
UGC09999H	480	April 2007	-1.916	—	0
UGC10029J	480	April 2007	-1.643	0.351	9
UGC10029H	480	April 2007	-2.071	0.295	10
UGC10048H	480	April 2007	-1.916	0.891	7
UGC10084J	480	April 2007	-1.613	0.178	8
UGC10084H	480	April 2007	-1.994	—	0
UGC10112J	480	April 2007	-1.671	0.020	5
UGC10112H	480	April 2007	-2.055	0.248	10
UGC10158J	480	April 2007	-1.659	0.115	6
UGC10158H	480	April 2007	-2.085	0.125	9
UGC10163J	480	April 2007	-1.630	0.180	8
UGC10163H	480	April 2007	-1.977	0.173	8
UGC10272H	480	April 2007	-2.006	0.324	10
UGC10371H	480	April 2007	-2.010	0.330	8
UGC10381H	480	April 2007	-2.055	—	0
UGC10391J	960	April 2007	-1.902	0.195	6
UGC10391H	480	April 2007	-1.997	0.414	9
VCC0545H	480	April 2005	-1.907	0.025	4
VCC1196H	480	March 2008	-1.786	—	0
VCC1412H	480	April 2007	-1.756	—	0

Table 2.1: UH 2.2-m Observations

Galaxy	T(sec)[1]	date	Z.P.(mag)[2]	σ [3]	NS[4]
VCC1512H	480	April 2006	-2.162	—	0
VCC1614H	480	April 2007	-1.966	0.040	7
VCC1809H	480	April 2005	-1.850	—	0
VCC1833H	480	April 2005	-1.932	—	0
VCC1906H	480	March 2008	-1.843	—	0

2.2 Sample

A large sample of 1088 S0 galaxies was selected from the UGC catalog (Nilson 1973) to have S0, S0a and S0B morphological classes and blue Galactic extinction ≤ 0.5. That sample was further restricted to areas of the sky covered by the Sloan Digital Sky Survey (York et al. 2000, hereafter, SDSS) bringing down the sample to 542 galaxies. Figure 2.1 shows color images from SDSS for a few galaxies in our sample. Various observational constraints limited us to NIR data for $\sim 15\%$ of the SDSS sub-sample. A NIR sample of 90 galaxies was selected to cover a representative range of mass and light concentrations and was later pruned to our final sample of 59 galaxies. Eight Virgo cluster S0 galaxies come from the sample by McDonald et al. (2009a) (hereafter M09); they were observed with the same equipment.

[1]Total exposure time in seconds

[2]Calibration zero point

[3]Uncertainty in calibration zero point

[4]Number of standard stars in the field

Table 2.2: Galaxy Characteristics

Galaxy	Type[1]	a[3](')	b[3](')	radial velocity[2](km s^{-1})	Distance[4](Mpc^{-3})	Inclination[5](°)	Type[6]
UGC04330	SB0	1.1	1.0	4865	69.4	34.61	B
UGC04596	S0	1.2	1.0	9439	131.7	25.35	T
UGC04599	S0	2.1	2.1	2072	31.8	18.26	T
UGC04631	S0	1.1	1.0	4159	60.6	24.25	N
UGC04639	S0?	1.4	1.3	8556	120.0	23.28	N
UGC04737	S0?	0.8	0.5	3813	56.0	53.33	N
UGC04869	S0?	2.0	0.7	6889	97.8	62.86	T,B
UGC04901	S0-A?	1.1	1.1	8424	118.7	28.92	N
UGC04910	S0	1.0	0.6	8353	117.8	28.92	N
UGC04916	S0	1.2	0.9	8785	123.6	36.21	N
UGC04989	S0	1.0	0.9	3646	54.1	60.89	N
UGC05075	S0-A	1.3	0.6	5435	79.0	26.61	N
UGC05094	S0	1.8	1.8	15154	210.3	58.69	N
UGC05182	S0	1.8	1.1	8692	123.2	34.61	N
UGC05403	SB0	1.8	0.9	2082	33.6	65.72	T
UGC05419	S0	3.3	1.9	6205	89.6	0.00	T
UGC05503	SB:0	2.3	1.3	1318	21.3	59.11	N
UGC05568	S0	1.7	0.8	2072	33.7	25.95	N

Table 2.2: Galaxy Characteristics

Galaxy	Type[1]	a[3](')	b[3](')	radial velocity[2](km s^{-1})	Distance[4](Mpc^{-3})	Inclination[5](°)	Type[6]
UGC05766	S0?	1.3	1.3	3075	47.7	60.66	B
UGC05952	S0	1.6	1.0	841	10.3	57.16	B
UGC08800	S0	1.4	0.7	816	10.3	62.86	B
UGC08886	S0?	1.0	0.7	5102	78.9	67.00	N
UGC08986	S0	1.5	0.7	1232	22.7	0.00	N
UGC08997	S0	1.1	0.6	7681	113.5	53.33	N
UGC09003	S0	1.6	0.9	4241	65.7	62.86	N
UGC09087	S0A	1.2	1.2	5131	78.8	52.43	B
UGC09156	S0	1.0	0.5	7705	114.2	67.00	N
UGC09212	S0	1.1	0.8	8543	124.9	54.09	N
UGC09280	S0	1.1	0.8	8017	118.2	54.42	N
UGC09321	S0	1.0	0.6	7671	113.5	0.00	N
UGC09387	S0	1.9	1.8	6274	94.1	62.86	N
UGC09400	S0	1.2	1.2	8634	126.7	36.21	N
UGC09434	S0-A	1.0	0.5	5412	82.5	44.85	T
UGC09514	SB0	1.4	0.9	8205	121.1	49.99	N
UGC09592	(S0)	1.1	0.9	5370	80.5	0.00	N
UGC09693	SB0	1.1	0.9	1225	21.8	0.00	B

Table 2.2: Galaxy Characteristics

Galaxy	Type[1]	a[3](')	b[3](')	radial velocity[2](km s^{-1})	Distance[4](Mpc^{-3})	Inclination[5](°)	Type[6]
UGC09705	S0	1.4	0.8	6690	99.4	62.86	N
UGC09713	S0	1.3	0.9	4934	75.8	60.37	B
UGC09939	S0?	1.1	1.1	3409	54.3	39.47	N
UGC09967	S0	1.0	0.8	8111	118.9	36.21	B
UGC09999	S0?	1.2	0.7	9546	137.8	57.49	N
UGC10029	S0-A	1.0	0.4	12440	177.6	49.99	T
UGC10048	S0	1.1	0.7	3937	62.1	0.00	N
UGC10084	S0	1.7	0.5	13880	196.7	56.58	N
UGC10112	S0	1.0	0.4	9883	142.5	74.27	N
UGC10158	S0-A	1.3	0.7	14315	202.8	44.85	N
UGC10163	S0	1.1	0.8	5505	83.9	73.18	T
UGC10272	-	-	-	5176	79.2	70.35	T
UGC10371	E?	1.2	0.9	10307	148.0	62.86	T
UGC10381	S0	3.5	1.7	8804	126.6	56.58	T
UGC10391	-	-	-	2438	40.9	47.86	N
VCC0545	-	-	-	1207	16.5	50.32	T,B
VCC1196	NA	1.0	0.7	909	16.5	61.95	N
VCC1412	-	-	-	1342	16.5	64.93	B

Table 2.2: Galaxy Characteristics

Galaxy	Type[1]	a[3](')	b[3](')	radial velocity[2](km s^{-1})	Distance[4](Mpc^{-3})	Inclination[5](°)	Type[6]
VCC1512	-	-	-	762	16.5	52.45	N
VCC1614	-	-	-	749	16.5	38.18	N
VCC1809	-	-	-	2798	16.5	53.89	N
VCC1833	-	-	-	1820	16.5	65.39	N
VCC1906	-	-	-	314	16.5	44.31	N

[1]Hubble type from UGC Catalog

[2]Heliocentric radial velocity (km s^{-1}) from NED

[3]Diameter is from UGC Catalog

[4]Distances are corrected for Virgo flow and the Great Attractor, from NED

[5]From UGC Catalog unless otherwise noted

[6]T (transition galaxy), B (barred, from Hyperleda), N (normal)

[7]Inclination is from Hyperleda

Our sample excludes galaxies with spiral structure, as gauged by visual inspection of SDSS images. Galaxies with tidal tails or faint spiral structure were retained, but put into a separate class. We call these galaxies "transition galaxies" due to the nascent emergence of spiral features in their morphology. The galaxies shown in Figure 2.1b, 2.1c and 2.1f are classified by us as transition galaxies. Although we are primarily interested in S0 galaxies with featureless disks, this transition class straddles the S0 classification in order to examine whether the putative transition in appearance from S0 to Sa galaxies correlates with a transition in stellar population properties. We note that some S0 galaxies left in our "featureless disk" sample are likely to still have spiral structure when examined with higher resolution telescopes, such as from HST (Drory & Fisher 2007), and our sample may also contain elliptical galaxies misclassified as S0.

Galaxies undergoing an obvious interaction or showing highly disturbed structure (from examination of 3-color images from SDSS) were excised from the sample, since clean bulge-disk decompositions and radial color profiles are ill-defined in these cases. Highly inclined galaxies with $i \geq 75$ deg, and galaxies that fell on the edge of the SDSS field of view, were also pruned from the sample in order to ensure well-defined surface brightness profiles. The inclination for each galaxy was determined from UGC axial ratios (Nilson 1973) and using a correction to inclination (see Haynes & Giovanelli 1984). When an inclination was not available in the UGC catalog, values were used from Hyperleda (Paturel et al. 2003). This estimate of inclination was used only for selection purposes.

Our final sample contains 59 galaxies; twelve of them are classified as transition galaxies. This sample is neither statistically complete nor randomly selected, but tailored to cover a wide range in global properties such as mass, concentration, and local environmental density (see § 2.5). Table 2.1 lists our sample galaxies along with relevant characteristics.

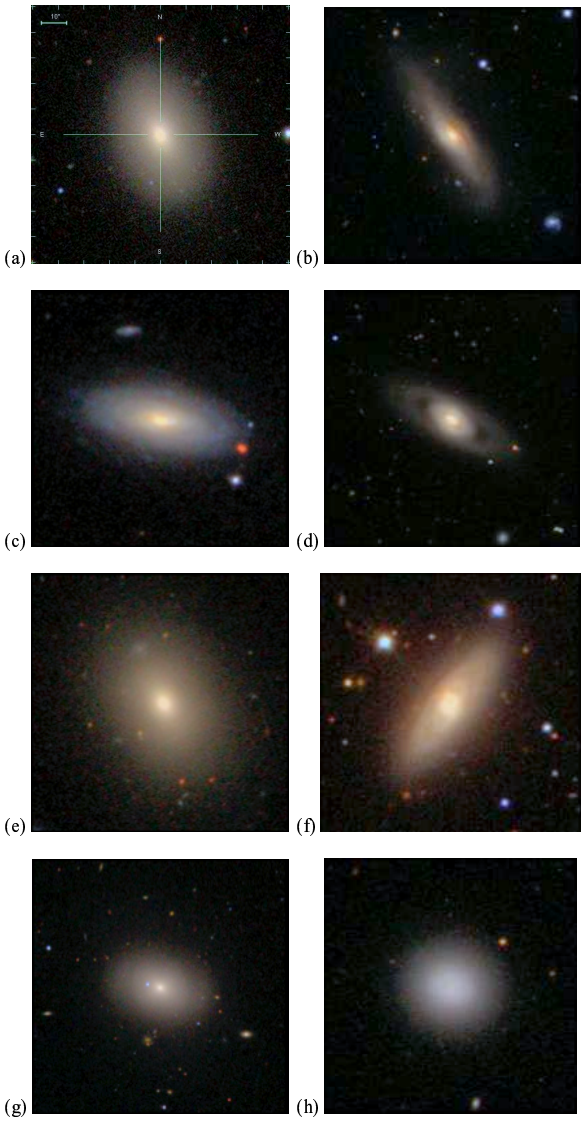

Figure 2.1 Color images of the following galaxies, a: UGC 10391, b: UGC 4869, c: UGC 5403, d: UGC 8886, e: UGC 9999, f: UGC 10163, g: VCC 1196, h: VCC 1614. The scale and orientation noted in panel (a) apply to all panels, except panels (b), (d), (g). In these cases the green bar is 20" long instead of 10".

2.3 Observations

Our stellar population analysis relies on optical and NIR photometry of 59 S0 galaxies. The NIR observations (J &/or H-band) are from the ULBCam at the University of Hawaii's 2.2-m telescope and the archival optical imaging (g & r) is taken from SDSS.

2.3.1 Optical Observations

Optical g & r images with a scale of 0.396 arcsec/pixel were extracted from the SDSS/DR5 archives. The u and z bands were avoided due to their low S/N. We did not use the i-band since stellar population models show that both the i and the r band, when combined with g and H or J bands, provide the same separation in age and metallicity.

2.3.2 Near-IR Observations

Near-IR images for the 59 S0 galaxies in our sample were obtained with the ULBCam at the University of Hawaii's 2.2-meter telescope on Mauna Kea in April 2005, 2006 and 2007 and March 2008. A total of 29 galaxies in our sample were observed only in the H band, 19 were observed only in the J band, and 11 galaxies were observed in both the J and H passbands. The K band filter was not available. The ULBCam image scale is 0.25 arcsecond per pixel. A maximum single exposure time of 40 seconds was used to maximize the sky flux whilst keeping within the detector's linear regime. A standard dithering script minimized the resampling of bad pixels. Only the cleanest of the four 2048x2048 arrays was used, resulting in an 8.5' by 8.5' field of view, large enough to properly determine the sky background levels for our sample galaxies. The near-IR flux calibration uses reference stars in the target galaxy field from the Two Micron All-Sky Survey (Skrutskie et al. 2006, hereafter 2MASS). Thus, no standard star observations for photometric calibration were necessary (see §2.4.1). A more detailed description of ULBCam data taking procedures is further

described in M09. A log of observations is presented in Table 2.2.

In the remainder of the paper, we refer to the galaxies observed in the J-band as the "J-band sample" and those observed in the H-band as the "H-band sample". The 11 overlapping galaxies are included in both samples.

2.4 Data Reduction

2.4.1 Basic Reductions

Optical images have been pre-processed by the SDSS for basic reduction such as flat-fielding, bias subtraction, and cosmic ray rejection. The photometric calibration of the light profiles (§ 2.4.6) uses the photometric zero-points provided in the SDSS/DR5 library.

Basic reductions of the UH near-IR data, which include flat-fielding, stacking, bad pixel rejection, geometric distortion corrections, and flux calibration were applied to the ULBCam data using the XVISTA software package[1]. The data reduction procedures, including geometric distortion correction, follow the prescription of M09. The near-IR flux calibration for light profiles uses infrared stellar photometry from 2MASS for stars in the ULBCam target galaxy fields. An error-weighted average offset between our brightnesses and the 2MASS H or J-band brightnesses was calculated and used for the zero-point calibration. This method of flux calibration enabled us to calibrate the photometry of our science images at each pixel, independent of airmass variations and transparency conditions. Additional information on flux calibration methods and stability can be found in M09. The photometric zero-point and its uncertainty (the standard deviation of the derived zero-point corrections from each star used in the field) are noted in Table 2.2. If fewer than 3 2MASS stars were found in the field (indicated by a zero in Table 2.2), the calibration from the previous and next exposures were averaged and used and the uncertainty quoted is the standard

[1]http://astronomy.nmsu.edu/holtz/xvista/index.html

deviation in all calibration values, +/- 0.17.

Surface brightnesses have been corrected for Galactic foreground extinction in each bandpass using the reddening values, A_Λ, of Schlegel et al. (1998) and assuming an $R_V = 3.1$ extinction curve.

2.4.2 PSF Matching

Wavelength-dependent image blurring by the atmosphere affects the calculations of colors for the inner galaxy radii. Thus, we measured the 2D seeing point spread function (PSF) to correct galaxy color profiles. The PSF full width at half maximum (FWHM) is measured from the final stacked image in each bandpass. The stars that are identified for PSF measurements in the g & r bands are individually sky-subtracted and fit with a 2-dimensional Gaussian function from which FWHMs are derived. On average, 50 stars are used for PSF measurements in each stacked SDSS image. The final PSF of the image is the median of all individual star PSFs. For NIR images, the final PSF of each image is the average of 5 individual PSFs. Images from each bandpass are degraded to the PSF of the worst seeing bandpass (typically the g image) by convolving with a 2D gaussian of appropriate FWHM. This effort suggests that differences in the PSFs will no longer affect the derivation of colors. However, as an added precaution against small differences in the PSF across each frame, we apply an inner radial cutoff of roughly 2 seeing disks (3 arcseconds) for the color profiles. The central region in all other analysis of colors is averaged within at-least the inner 2 seeing disks. PSF measurements have also enabled the identification of foreground stars that are then removed from the galaxy light following the prescription given in M09.

2.4.3 Sky Measurement

Careful sky subtraction is crucial for accurate analysis of deep surface brightness profiles. Sky subtraction follows slightly different approaches for SDSS and NIR im-

ages.

We have used the sky value provided with each SDSS image[2]. For the images where the sky value was not available ($\sim$ half our sample), we used the lowest of either the sky measurements measured by us from the entire SDSS image or from the four image corners. The latter method gives sky measurements within 0.5% of the SDSS values (M09).

For the NIR data, the sky is measured in four rectangular boxes along the perimeter of the field of view and then averaged together to give the mean sky value for that image. Each of the four sky boxes has a typical size of $\sim$ 500 x 75 arcseconds. For each box the sky level is measured with the XVISTA SKY routine. The typical deviation of sky levels amongst the four boxes for the near-IR data are .004% of the sky value.

2.4.4 Surface Brightness Profile Extraction and Error Estimates

Surface brightness profiles were extracted by fitting elliptical isophotes to the galaxy images in the r -band. The XVISTA command, PROFILE that performs this operation, uses a generalized non-linear least-squares fitting routine. For these fits, ellipticity and position angle are allowed to vary but the ellipse center is held fixed. The isophotal solutions based on the r-band images were then applied uniformly to the images in the g, J, and H band images. This ensures that color gradients are computed from the same matching isophotes. Further details about isophotal fitting and profile extraction, including details on profile depth and signal-to-noise ratios, are given in Courteau (1996) and M09.

The effect that the systematic sky error has on galaxy photometry naturally increases with radius in the galaxy. Therefore, to estimate the effect that the systematic sky error has on measured quantities, we have recalculated the surface brightness profiles and color profiles using sky values adjusted to $sky = sky_{orig} \pm 1\sigma_{sys}$, where σ_{sys} is

[2]http://www.sdss.org/dr5/algorithms/flatfield.html

the systematic sky uncertainty. This is calculated as the standard error in the mean of the sky values (as described in § 2.4.3) from four boxes along the perimeter of the image. We determine the sky effect at each radius along the SB profile as half the difference in the surface brightness calculated with the sky value set at $sky = sky_{orig} + \sigma_{sys}$ and $sky = sky_{orig}$ - σ_{sys}. When we refer to a "sky effect" in subsequent discussion for g-r and r-H colors, this measurement of sky systematic error has been added in quadrature for each respective band.

The final errors in surface photometry at each isophote consist of two contributions. The first is the is the standard deviation in the surface brightness around the best fit ellipse; it naturally includes statistical errors in the sky background. The other contribution comes from the systematic sky estimate error (discussed above as the "sky effect").

2.4.5 Outer Radial Cutoff

The low near-IR surface brightness galaxy counts, relative to the bright near-IR sky background, make accurate determination of the sky background essential for extracting reliable surface photometry in the J and H passbands. This is demonstrated in Fig. 2.2 for a sample galaxy (UGC 4737). The SB profile is shown with black dots and the sky error envelopes are depicted by green and red crosses. We define the outer radial cutoff as the point where the sky error envelopes deviate from each other by more than 0.4 mag arcsecond^{-2}. Our NIR profiles are intrinsically shallower than SDSS profiles and the common outer truncation radius was thus determined using J and H profiles. In the few cases where the surface brightness profile errors (for any of the optical or near-IR filters) continually exceed 0.2 mag arcsecond^{-2}, that point would be used as the outer cutoff instead. An example of the outer cutoff, based on an H-band profile, is shown in Fig. 2.2 as the dashed vertical line. The profiles for all the galaxies are shown in the electronic version of the paper. The outer radial cutoffs for each galaxy in the J and H-bands are given in Table 2.3. The radial cutoff used for the g and r bands matches whichever NIR band is being used for analysis.

Table 2.3: Derived Radial Quantities

		Inner				Outer			
Name	cutoff (")	age(Gyr)	σ	[Z/H]	σ	age(Gyr)	σ	[Z/H]	σ
H band derived									
UGC04596	38	6.93	0.62	0.23	0.02	1.81	0.11	0.12	0.05
UGC04737	62	2.99	0.06	0.43	0.01	5.38	1.58	0.00	0.12
UGC04869	100	3.31	–	0.50	–	1.69	–	0.44	–
UGC05094	60	3.18	–	0.50	–	3.45	–	0.34	–
UGC05182	50	3.65	0.23	0.38	0.01	12.57	–	-0.43	–
UGC05403	41	4.00	–	0.50	–	1.21	0.12	0.17	0.20
UGC05419	78	2.74	–	0.50	–	2.41	–	0.15	–
UGC05568	65	1.18	–	0.50	–	1.65	0.21	0.18	0.07
UGC05766	65	2.11	–	0.50	–	2.73	–	0.11	–
UGC08886	70	2.98	–	0.50	–	4.83	0.95	-0.23	0.06
UGC09280	60	2.52	–	0.50	–	6.51	0.68	-0.13	0.06
UGC09321	75	3.26	0.05	0.40	0.01	13.69	–	-0.47	–
UGC09400	60	3.95	0.17	0.42	0.01	2.13	–	0.25	–
UGC09434	48	2.91	–	0.48	–	6.94	1.53	0.00	0.09
UGC09514	55	3.89	0.24	0.35	0.01	6.52	2.47	-0.13	0.12
UGC09592	70	2.41	–	0.50	–	2.68	0.27	0.10	0.08
UGC09693	65	2.34	–	0.50	–	2.73	–	0.25	–
UGC09705	35	1.01	–	0.50	–	6.45	1.48	-0.29	0.08
UGC09713	50	2.40	–	0.50	–	12.61	–	-0.15	–
UGC09939	60	2.62	–	0.50	–	3.02	–	0.28	–
UGC09967	34	1.95	–	0.50	–	1.20	–	0.49	–
UGC09999	75	3.35	–	0.50	–	9.01	1.43	0.08	0.07
UGC10029	38	1.88	–	0.50	–	2.87	0.64	-0.17	0.08
UGC10048	40	2.50	0.24	0.42	0.02	2.56	–	0.15	–

Table 2.3: Derived Radial Quantities

		Inner				Outer			
Name	cutoff (")	age(Gyr)	σ	[Z/H]	σ	age(Gyr)	σ	[Z/H]	σ
UGC10084	62	3.17	–	0.50	–	4.40	1.41	0.21	0.08
UGC10112	40	3.03	–	0.50	–	11.72	–	-0.13	–
UGC10158	45	3.44	–	0.50	–	8.88	1.37	0.00	0.06
UGC10163	70	3.23	0.06	0.47	0.01	4.15	0.93	-0.01	0.06
UGC10272	70	3.40	–	0.50	–	2.86	–	0.13	–
UGC10371	55	1.87	–	0.50	–	1.80	–	0.38	–
UGC10381	20	2.76	–	0.50	–	2.68	–	0.32	–
UGC10391	40	2.39	–	0.47	–	8.66	1.01	-0.48	0.04
VCC00545	15	1.58	0.15	0.32	0.06	1.57	0.25	0.21	0.13
VCC01196	65	2.92	0.05	0.06	0.02	13.50	–	-0.96	–
VCC01412	100	5.04	0.27	0.25	0.01	3.24	–	0.18	–
VCC01512	24	1.89	–	0.50	–	0.79	–	0.50	–
VCC01614	27	1.04	–	0.50	–	3.62	0.94	-0.71	0.10
VCC01809	40	0.53	–	0.49	–	1.21	0.09	0.29	0.08
VCC01833	20	1.12	–	0.50	–	2.53	0.28	-0.27	0.08
VCC01906	17	1.13	–	0.50	–	1.08	–	0.50	–
J band derived									
UGC04330	43	2.04	–	0.50	–	1.91	–	0.44	–
UGC04599	58	1.60	–	0.43	–	0.77	0.04	0.29	0.03
UGC04631	36	2.64	0.28	0.45	0.02	13.69	–	-0.59	–
UGC04639	58	3.28	0.05	0.42	0.01	1.06	–	0.50	–
UGC04901	90	3.08	–	0.50	–	1.97	–	0.50	–
UGC04910	60	3.49	0.13	0.29	0.01	3.86	–	0.13	–
UGC04916	39	4.68	0.34	0.26	0.01	13.69	–	-1.09	–
UGC04989	67	2.51	0.25	0.43	0.02	1.94	0.37	0.20	0.13

Table 2.3: Derived Radial Quantities

		Inner				Outer			
Name	cutoff (")	age(Gyr)	σ	[Z/H]	σ	age(Gyr)	σ	[Z/H]	σ
UGC05075	32	1.81	–	0.50	–	0.99	–	0.41	–
UGC05503	75	0.75	–	0.50	–	3.37	–	-0.21	–
UGC05952	120	2.44	–	0.33	–	1.11	–	0.50	–
UGC08800	38	0.94	0.06	0.38	0.03	4.11	1.05	-0.91	0.18
UGC08986	33	1.57	–	0.37	–	11.92	–	-0.48	–
UGC08997	48	3.38	0.07	0.34	0.01	13.03	–	-0.25	–
UGC09003	28	0.72	–	0.50	–	0.83	0.06	0.20	0.06
UGC09087	68	2.32	0.09	0.38	0.01	2.47	–	0.40	–
UGC09156	80	4.06	0.24	0.40	0.01	13.69	–	-0.39	–
UGC09212	63	3.57	0.21	0.38	0.01	3.80	0.99	-0.10	0.08
UGC09280	65	3.16	0.24	0.33	0.03	13.35	–	-0.47	–
UGC09387	28	2.56	–	0.35	–	0.88	0.05	0.27	0.04
UGC09400	50	5.64	0.24	0.29	0.01	2.63	–	0.13	–
UGC09705	35	1.12	–	0.50	–	6.93	2.24	-0.38	0.12
UGC09713	45	2.99	0.02	0.43	0.01	11.09	1.10	-0.12	0.04
UGC09967	38	2.34	–	0.50	–	1.19	–	0.22	–
UGC10029	38	2.05	–	0.50	–	2.54	0.57	-0.16	0.09
UGC10084	70	3.52	0.14	0.47	0.01	6.51	1.67	0.04	0.09
UGC10112	40	2.89	–	0.50	–	13.66	–	-0.25	–
UGC10158	62	4.70	0.39	0.47	0.02	1.45	–	0.45	–
UGC10163	68	2.72	–	0.50	–	11.97	–	-0.56	–
UGC10391	32	2.31	0.20	0.44	0.02	12.71	–	-0.68	–

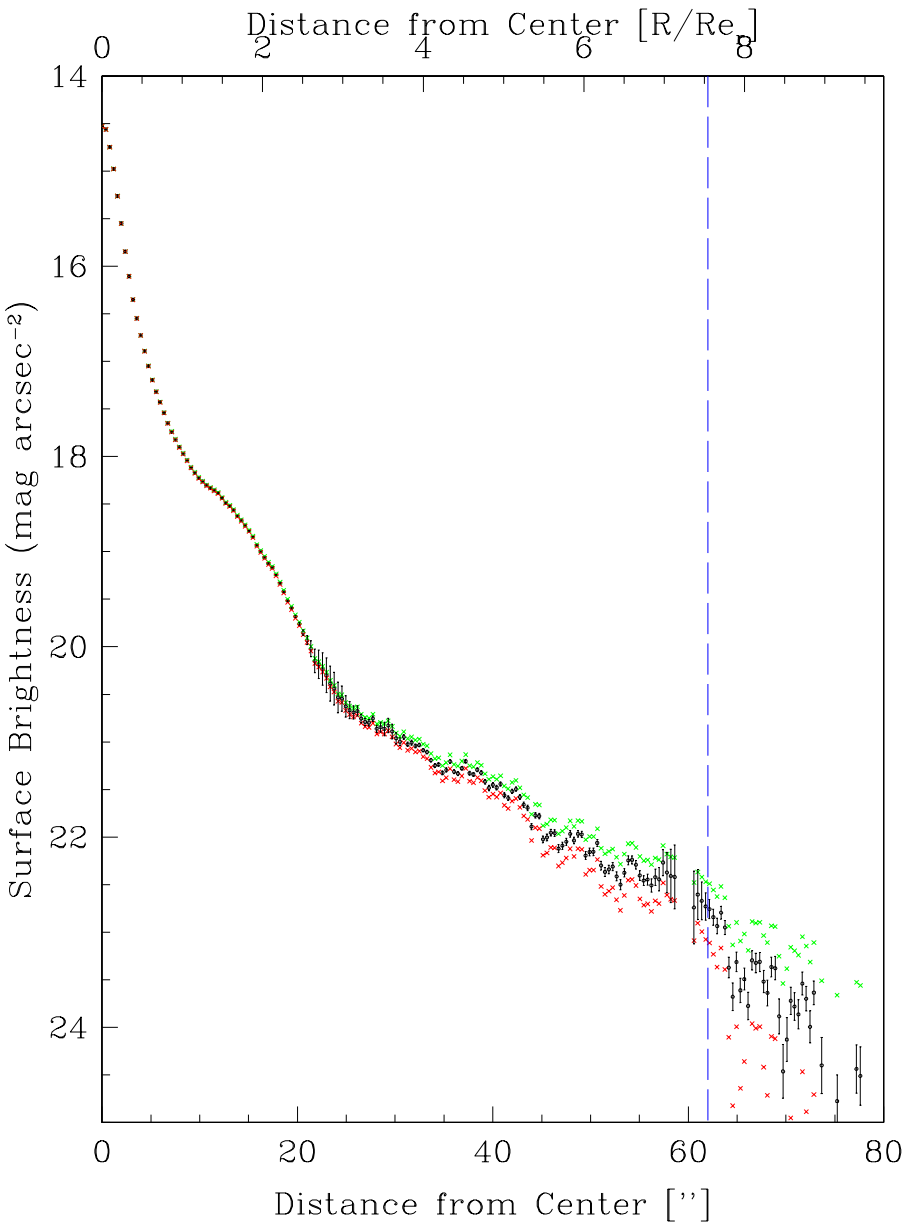

Figure 2.2 H-band radial surface brightness (SB) profile for UGC 4737. The SB profile is shown as black dots with $\pm\sigma$ sky error envelopes as green and red 'x's, respectively. The sky error envelopes are calculated using sky values adjusted to $sky = sky_{orig} \pm 1\sigma_{sys}$. The lower axis indicates the radial extent from the center in arcseconds while the upper axis is scaled by the r-band half-light radius. The outer cutoff is shown as a vertical blue dashed line. Error bars at each radial point represent the 1 σ surface brightness error. The profiles with sky error envelopes for other galaxies are provided in the electronic version of the paper.

2.4.6 Surface Brightness and Color Profiles

Optical (g & r) and NIR (J and/or H) surface brightness profiles are extracted for galaxies in our sample following the prescription outlined in § 2.4.4. Fig. 2.3 shows an example surface brightness profile for UGC 4869. A color image of this galaxy is shown in Fig. 2.1b. The entire collection of SB profiles is shown in Fig. 2.4. The g, r, J, and H bandpasses are represented by blue, magenta, red, and black data points. The J and H profiles are displayed for the 11 galaxies observed in both passbands. Color profiles for g-r and r-H versus radius for the H-band sample are shown in Fig. 2.5; color profiles for the J-band sample galaxies are given in the electronic version of the paper. All surface brightness and color profiles terminate at the outer radial cutoff as described above. In the figures where both J and H profiles are displayed, the cutoff for the g and r passbands is determined from whichever cutoff is largest between H-band and J-band. The error bars shown on the surface brightness and color profiles at each radius designate the $\pm$ 1σ errors in the surface brightness and in the color (surface brightness errors combined in quadrature), respectively; these errors tend to be small, generally smaller than the point size, except at the largest radii. Interior to the outer radial cutoff, surface brightnesses and colors are not plotted for radii where the surface brightness error exceeds 0.1 mag. Gaps in SB and color profiles, such as that seen for UGC 4737 around 25", are due to overlapping foreground stars or galaxies. Since these foreground objects have been masked during ellipse fitting, they do not affect the profile shape.

We also compute effective radii and total magnitudes in the g, r, J, and H bands. To determine the total magnitude, we have extrapolated the surface brightness profile outward by fitting the outer galaxy with an exponential function. Specifically, least squares fits were performed over the region from 50% to 90% of the radius at 26 r mag arcsec^{-2}, r_{26}, or to 90% of the maximum measured radius if the photometry does not extend that far. The effective radius, R_e, is the radius that contains 50% of the extrapolated total light. See Courteau (1996) for more information. If the SB profile contains a clear plateau, as in a Type II Freeman profile (Freeman 1970), then no

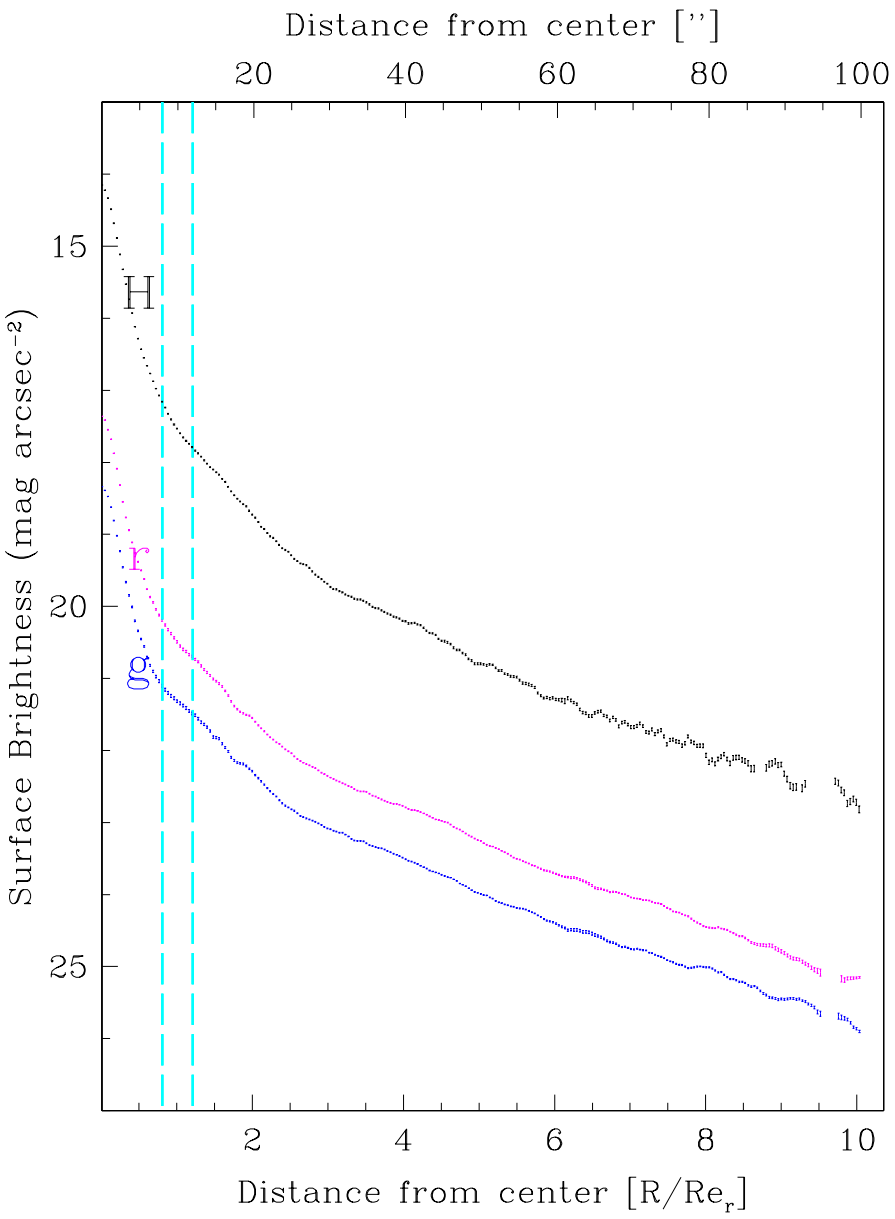

Figure 2.3 An example radial surface brightness profiles in H-band (black), g-band (blue), and r-band (magenta) is shown for UGC 4869. Vertical dashed cyan lines indicate the separation between the inner and outer radial regions. Surface brightness errors of 1 σ are shown on each radial point. The upper axis indicates the radial extent from the center in arcseconds while the lower axis is scaled by the r-band half-light radius. Profiles for the remaining galaxies are shown in Fig. 2.4

extrapolation was performed. Total magnitudes, mean colors and the effective radius for each galaxy in our sample are given in Table 2.4.

The lower axis of the surface brightness and color profiles in Figures 2.4 and 2.5 shows the radius in terms of the r-band effective radius (R_e) of the galaxy. Most profiles extend past 5 R_e. It is also apparent that our sample galaxies cover a range in profile shapes, suggesting a variety of contributions from galactic components. Dips and plateaus in the surface brightness profiles, such as those seen for UGC 4596, are due to structure in the galaxy, usually rings, bars, or spiral structure, and/or extinction by dust.

Table 2.4: Derived Total Quantities

Name	r_{tot}	g_{tot}	H_{tot}	J_{tot}	$Re_r(")$	g-r_{tot}	r-H_{tot}	r-J_{tot}
UGC04596	14.0	14.7	11.4	–	9.9	0.7	2.6	–
UGC04737	13.2	14.0	10.4	–	8.2	0.8	2.8	–
UGC04869	12.9	13.8	10.0	–	11.9	0.8	3.0	–
UGC05094	14.0	14.8	11.2	–	8.3	0.8	2.8	–
UGC05182	13.0	13.8	10.4	–	10.6	0.9	2.6	–
UGC05403	13.3	14.1	10.6	–	10.7	0.8	2.7	–
UGC05419	12.3	13.0	9.7	–	19.0	0.7	2.6	–
UGC05568	12.1	12.8	9.7	–	15.3	0.7	2.4	–
UGC05766	12.2	12.9	9.6	–	17.2	0.8	2.6	–
UGC08886	12.9	13.7	10.1	–	6.1	0.8	2.8	–
UGC09280	13.0	13.8	10.4	11.2	14.2	0.8	2.6	1.8
UGC09321	12.3	13.1	9.7	–	12.8	0.8	2.6	–
UGC09400	13.2	14.0	10.5	11.3	10.3	0.8	2.7	1.9
UGC09434	12.9	13.8	10.3	–	12.4	0.8	2.6	–
UGC09514	13.2	14.0	10.6	–	11.2	0.8	2.6	–
UGC09592	12.1	12.9	9.5	–	14.9	0.7	2.6	–
UGC09693	12.1	12.9	9.4	–	13.0	0.8	2.7	–

Table 2.4: Derived Total Quantities

Name	r_{tot}	g_{tot}	H_{tot}	J_{tot}	$Re_r(")$	g-r_{tot}	r-H_{tot}	r-J_{tot}
UGC09705	13.7	14.4	11.0	11.7	7.0	0.7	2.6	2.0
UGC09713	13.0	13.8	10.5	11.1	16.7	0.8	2.5	1.9
UGC09939	13.6	14.5	10.6	–	11.9	0.9	2.9	–
UGC09967	14.0	14.8	11.1	11.9	7.6	0.8	2.9	2.1
UGC09999	13.0	13.8	10.2	–	13.1	0.9	2.7	–
UGC10029	13.5	14.3	10.8	11.6	9.9	0.8	2.7	1.9
UGC10048	13.1	13.8	10.4	–	7.2	0.7	2.6	–
UGC10084	13.4	14.2	10.6	11.4	12.3	0.8	2.8	2.0
UGC10112	13.8	14.6	11.0	11.6	8.1	0.9	2.8	2.2
UGC10158	13.5	14.4	10.8	11.5	14.9	0.9	2.8	2.0
UGC10163	12.8	13.7	9.8	10.6	6.5	0.9	2.9	2.2
UGC10272	12.7	13.4	9.9	–	14.6	0.7	2.8	–
UGC10371	13.6	14.5	10.6	–	12.3	0.8	3.0	–
UGC10381	13.2	14.0	10.8	–	11.0	0.8	2.4	–
UGC10391	13.0	13.8	10.4	11.1	9.4	0.8	2.6	1.9
VCC00545	14.7	15.3	12.4	–	12.2	0.7	2.2	–
VCC01196	12.7	13.4	10.5	–	18.6	0.7	2.2	–
VCC01412	11.1	11.9	8.4	–	20.2	0.8	2.6	–
VCC01512	14.8	15.2	11.8	–	14.1	0.4	3.0	–
VCC01614	13.7	14.3	11.4	–	9.0	0.6	2.3	–
VCC01809	13.3	13.9	11.0	–	12.9	0.5	2.4	–
VCC01833	13.7	14.4	11.3	–	9.4	0.6	2.4	–
VCC01906	15.1	15.7	12.1	–	6.9	0.6	3.0	–
UGC04330	12.6	13.4	–	10.5	14.8	0.8	–	2.1
UGC04599	13.6	14.2	–	11.8	9.3	0.6	–	1.8
UGC04631	13.5	14.3	–	11.6	12.0	0.8	–	1.9

Table 2.4: Derived Total Quantities

Name	r_{tot}	g_{tot}	H_{tot}	J_{tot}	$Re_r(")$	g-r_{tot}	r-H_{tot}	r-J_{tot}
UGC04639	13.0	13.8	–	11.1	8.7	0.8	–	2.0
UGC04901	12.7	13.5	–	10.6	14.3	0.8	–	2.1
UGC04910	12.7	13.6	–	10.8	11.8	0.8	–	1.9
UGC04916	13.4	14.2	–	11.6	10.2	0.8	–	1.8
UGC04989	12.8	13.5	–	10.7	14.0	0.8	–	2.1
UGC05075	13.1	13.9	–	11.0	7.0	0.8	–	2.1
UGC05503	12.2	12.8	–	10.5	15.9	0.6	–	1.7
UGC05952	10.8	11.6	–	8.9	13.0	0.7	–	1.9
UGC08800	13.0	13.6	–	11.6	17.4	0.6	–	1.4
UGC08986	13.6	14.3	–	12.0	17.9	0.7	–	1.6
UGC08997	13.1	13.7	–	11.0	8.1	0.6	–	2.1
UGC09003	14.4	14.9	–	12.7	10.8	0.5	–	1.8
UGC09087	13.4	14.2	–	11.6	18.2	0.8	–	1.8
UGC09156	12.5	13.4	–	10.5	12.2	0.9	–	2.0
UGC09212	13.4	14.2	–	11.4	8.5	0.8	–	2.0
UGC09387	14.4	15.2	–	12.6	7.4	0.7	–	1.8

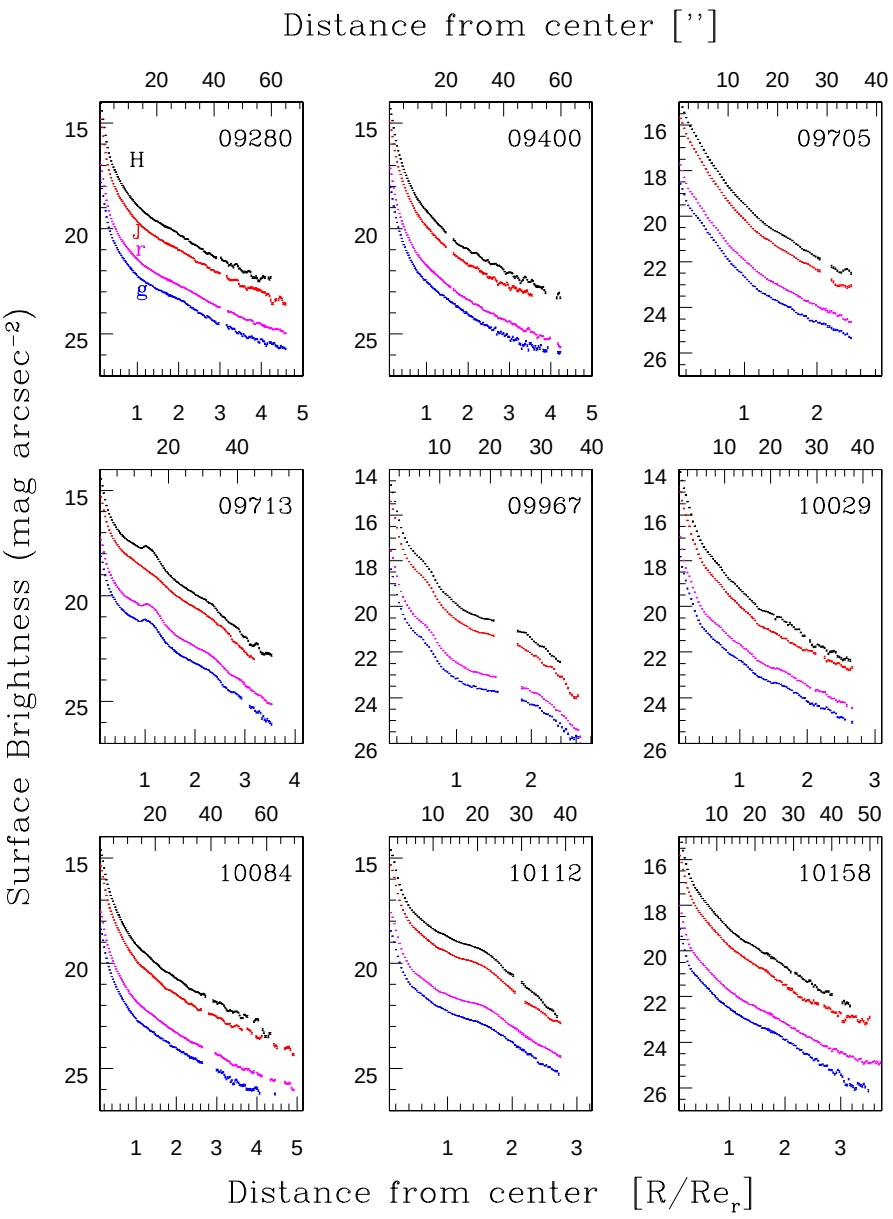

Figure 2.4 Radial surface brightness profiles in g-band (blue), r-band (magenta), J-band (red), and H-band (black) are shown for our entire sample of 59 S0 galaxies. At each radial point, the ± 1 σ error bars for surface brightness error are shown. The lower axis indicates the radial extent in arcseconds from the center while the upper axis is scaled by the r-band half-light radius. UGC or VCC numbers of the galaxies are given in the upper right corner of each panel.

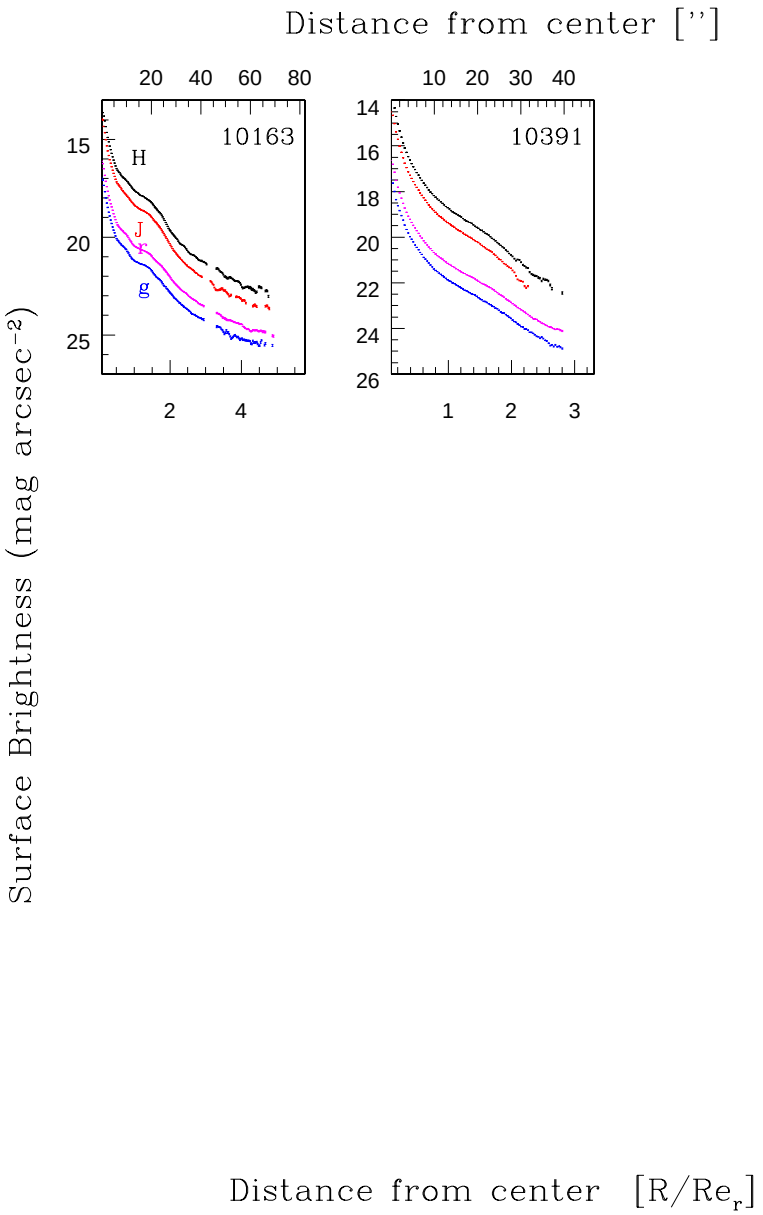
Distance from center ['']
20 40 60 80
10 20 30 40
10163
10391
H
J
K
g
15
20
25
14
16
18
20
22
24
26
2 4
1 2 3
Surface Brightness (mag arcsec^{-2})
Distance from center [R/Re$_r$]

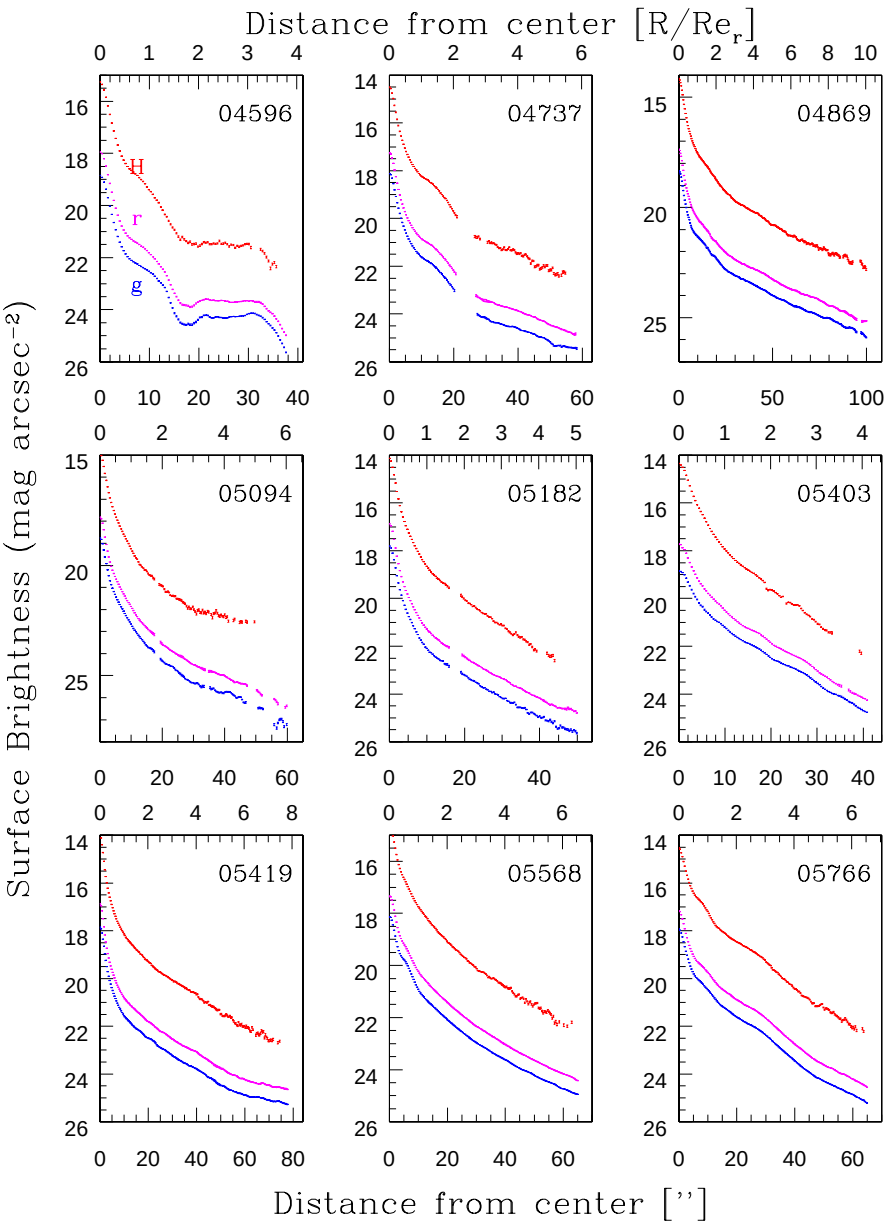
Distance from center [R/Re$_r$]
Surface Brightness (mag arcsec^{-2})
Distance from center ['']
04596
04737
04869
05094
05182
05403
05419
05568
05766
H
r
g

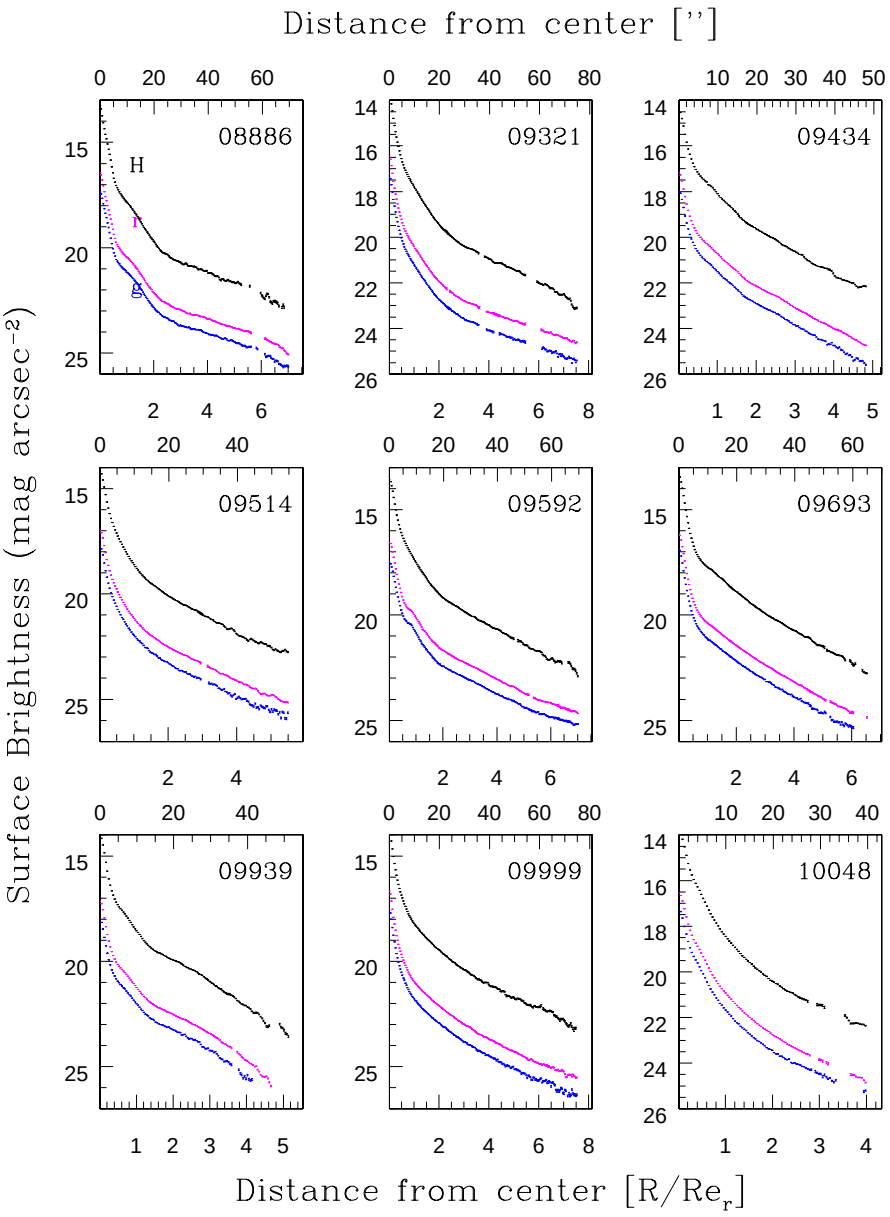
Distance from center ['']
Surface Brightness (mag arcsec^{-2})
08886
09321
09434
09514
09592
09693
09939
09999
10048
H
I
B
Distance from center [R/Re$_r$]

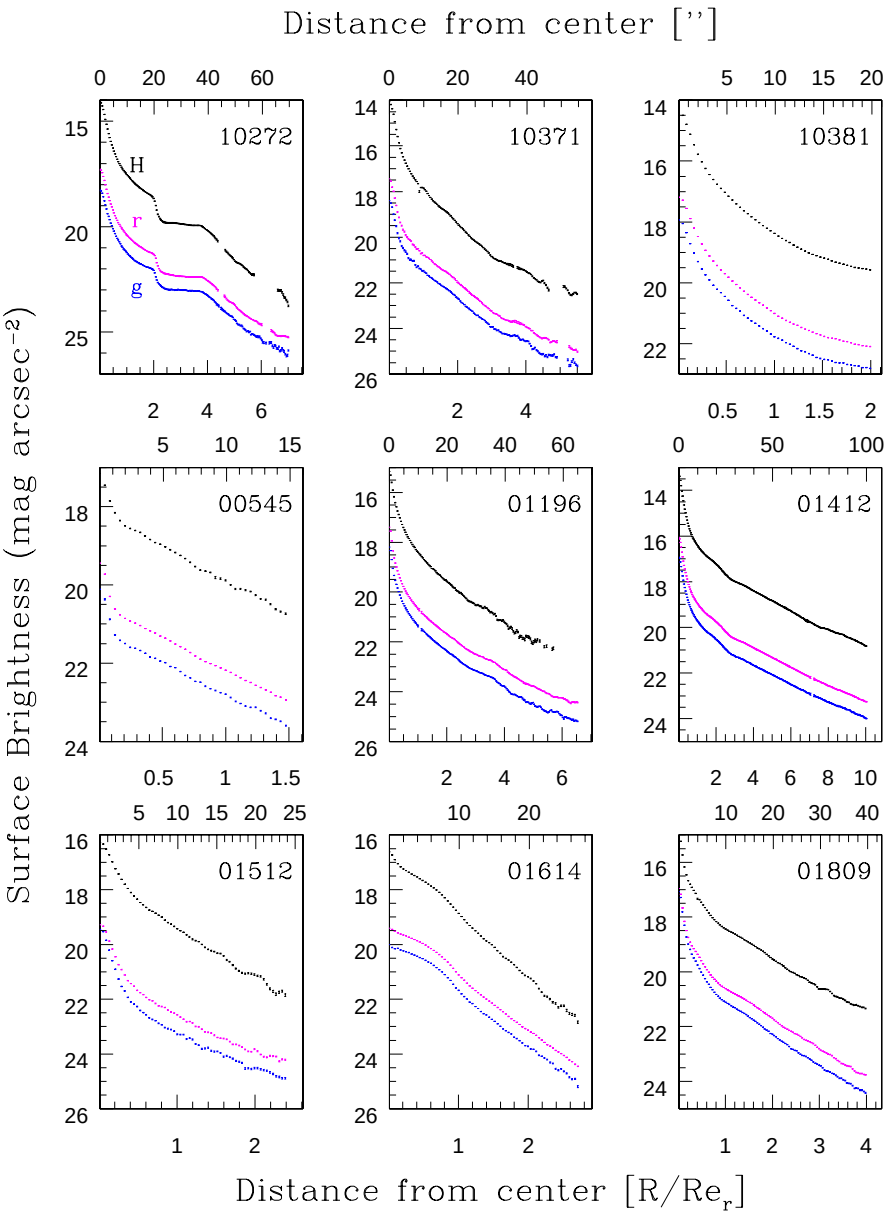
Distance from center ['']
Surface Brightness (mag arcsec^{-2})
10272
H
r
g
10371
10381
00545
01196
01412
01512
01614
01809
Distance from center [R/Re$_r$]

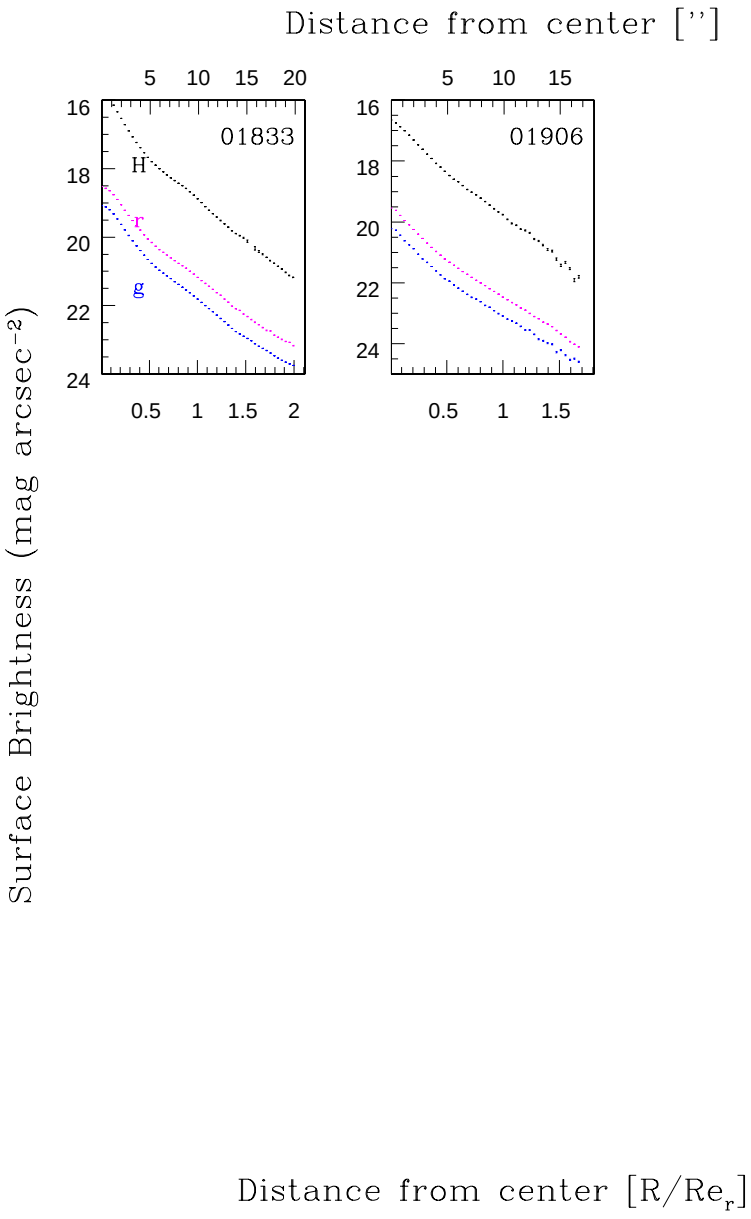
Distance from center ['']
5
10
15
20
16
18
20
22
24
01833
H
r
g
0.5
1
1.5
2
01906
Surface Brightness (mag arcsec^{-2})
Distance from center [R/Re$_r$]

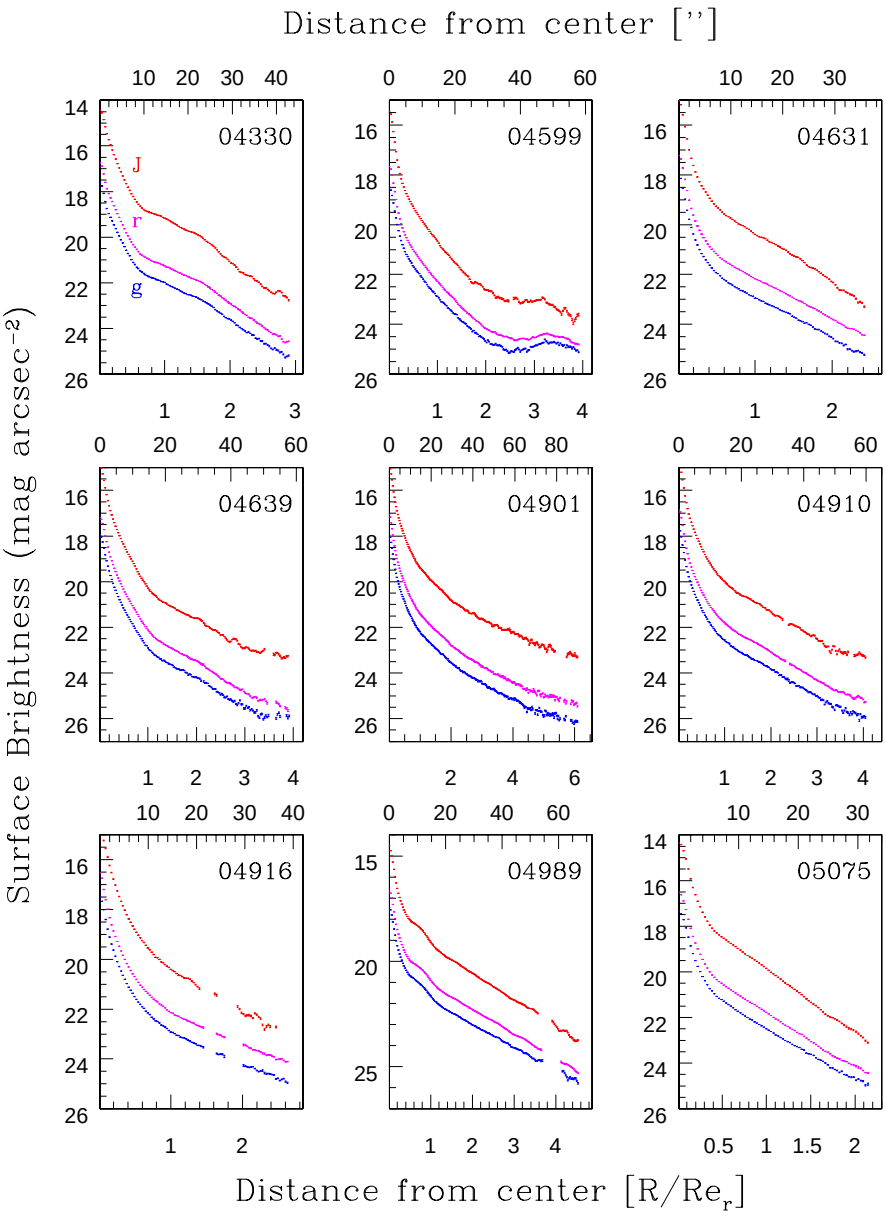
Distance from center ['']
Surface Brightness (mag arcsec^{-2})
Distance from center [R/Re$_r$]
04330
04599
04631
04639
04901
04910
04916
04989
05075
J
r
g

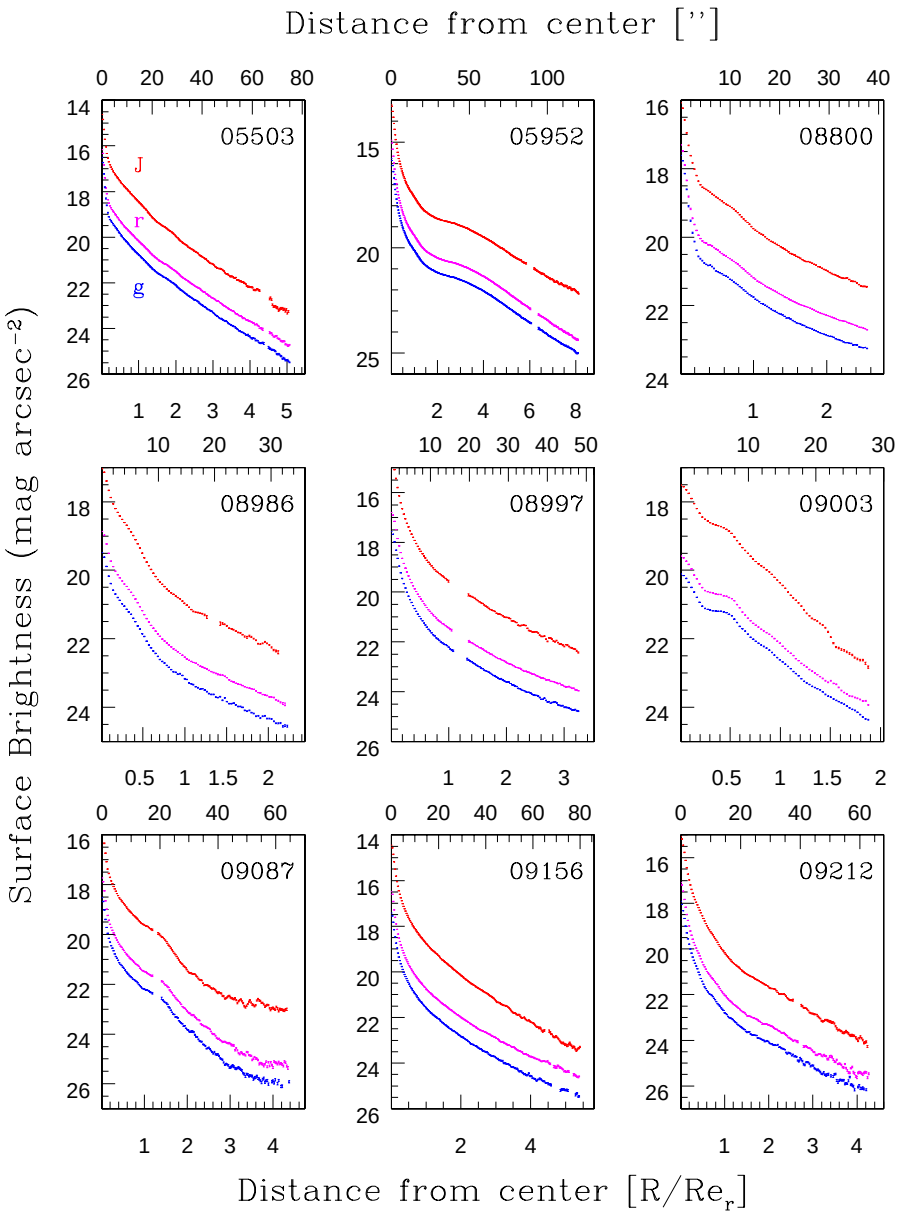
Distance from center ['']
Surface Brightness (mag arcsec^{-2})
Distance from center [R/Re$_r$]
05503
J
r
g
05952
08800
08986
08997
09003
09087
09156
09212

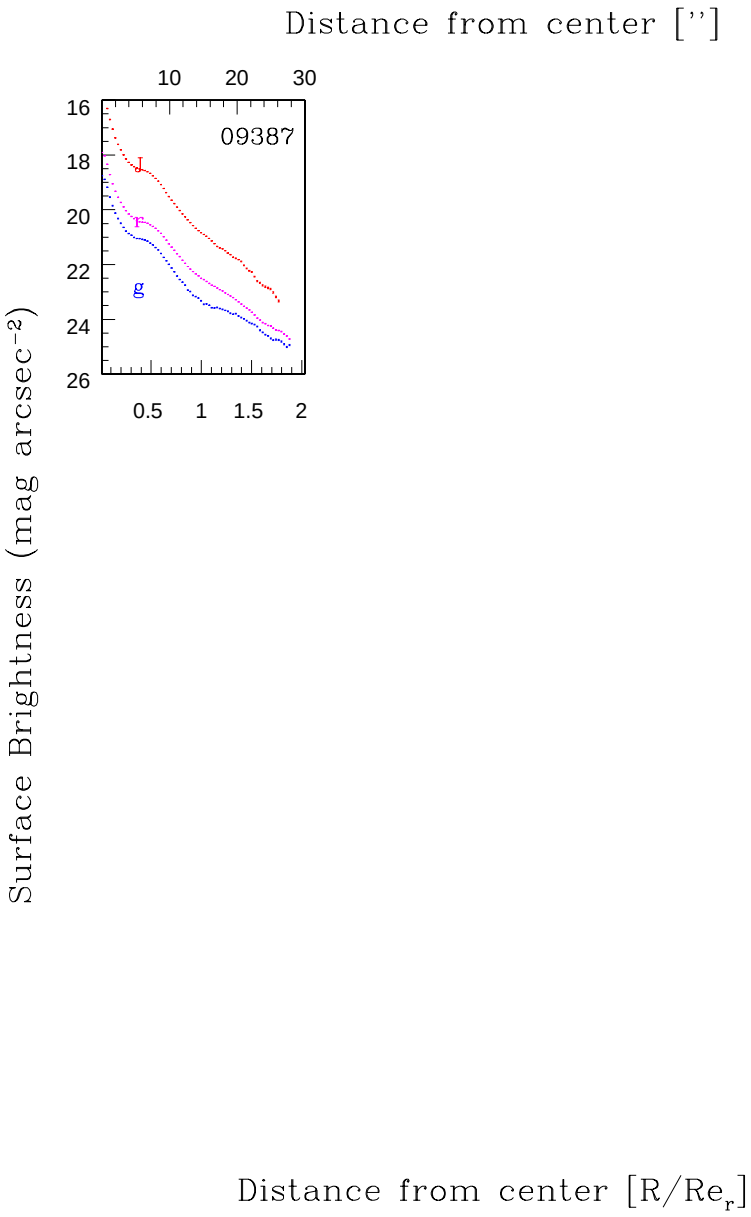
Distance from center ['']
10
20
30
16
18
20
22
24
26
09387
I
r
g
0.5
1
1.5
2
Surface Brightness (mag arcsec^{-2})
Distance from center [R/Re$_r$]

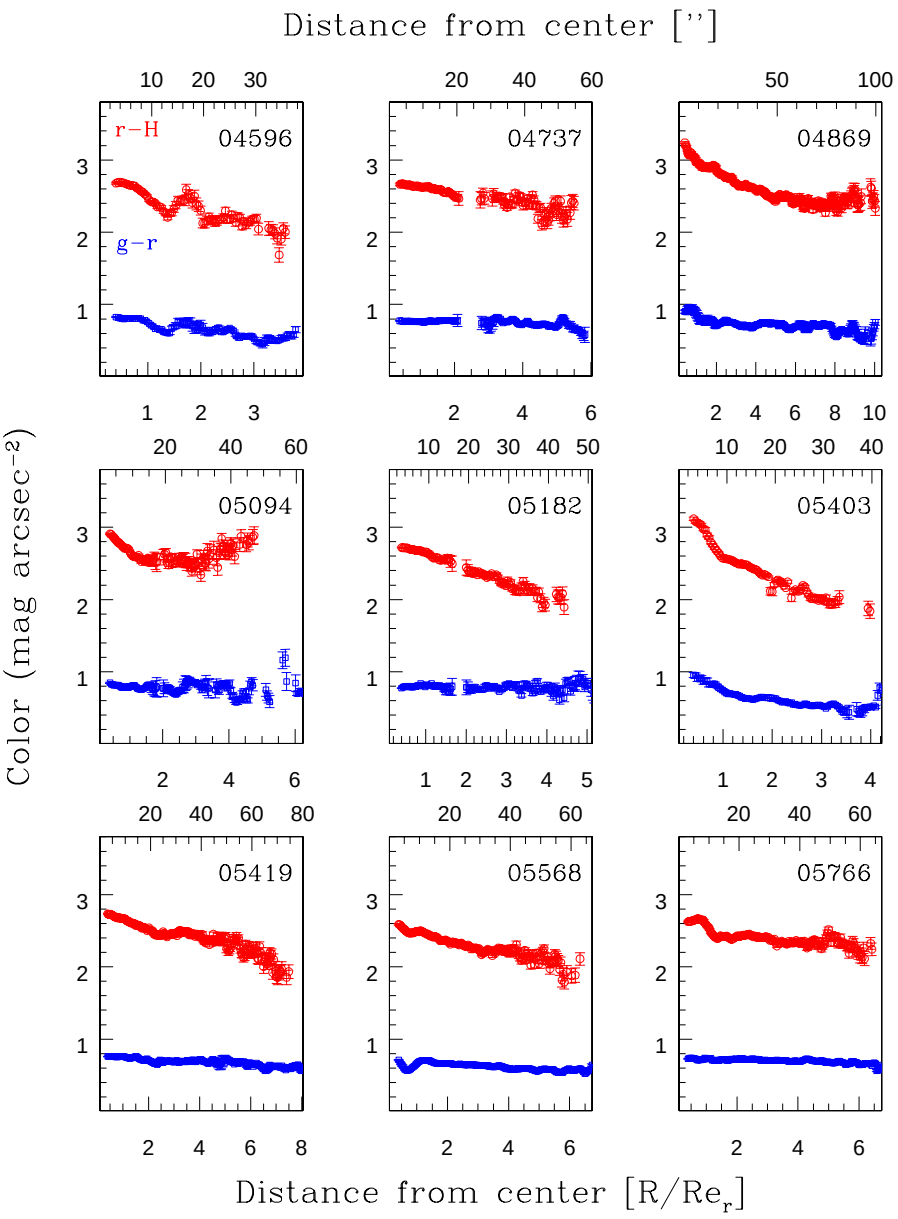

Figure 2.5 Radial color profiles in r-H (red) and g-r (blue) are shown for the H-band sample. The upper axis indicates the radial extent in arcseconds from the center while the lower axis is scaled by the r-band half-light radius. $\pm 1\ \sigma$ error bars represent the uncertainty in color based on the combined surface brightness error for each radial point. UGC or VCC numbers of the galaxy shown are given in the upper right corner of each panel.

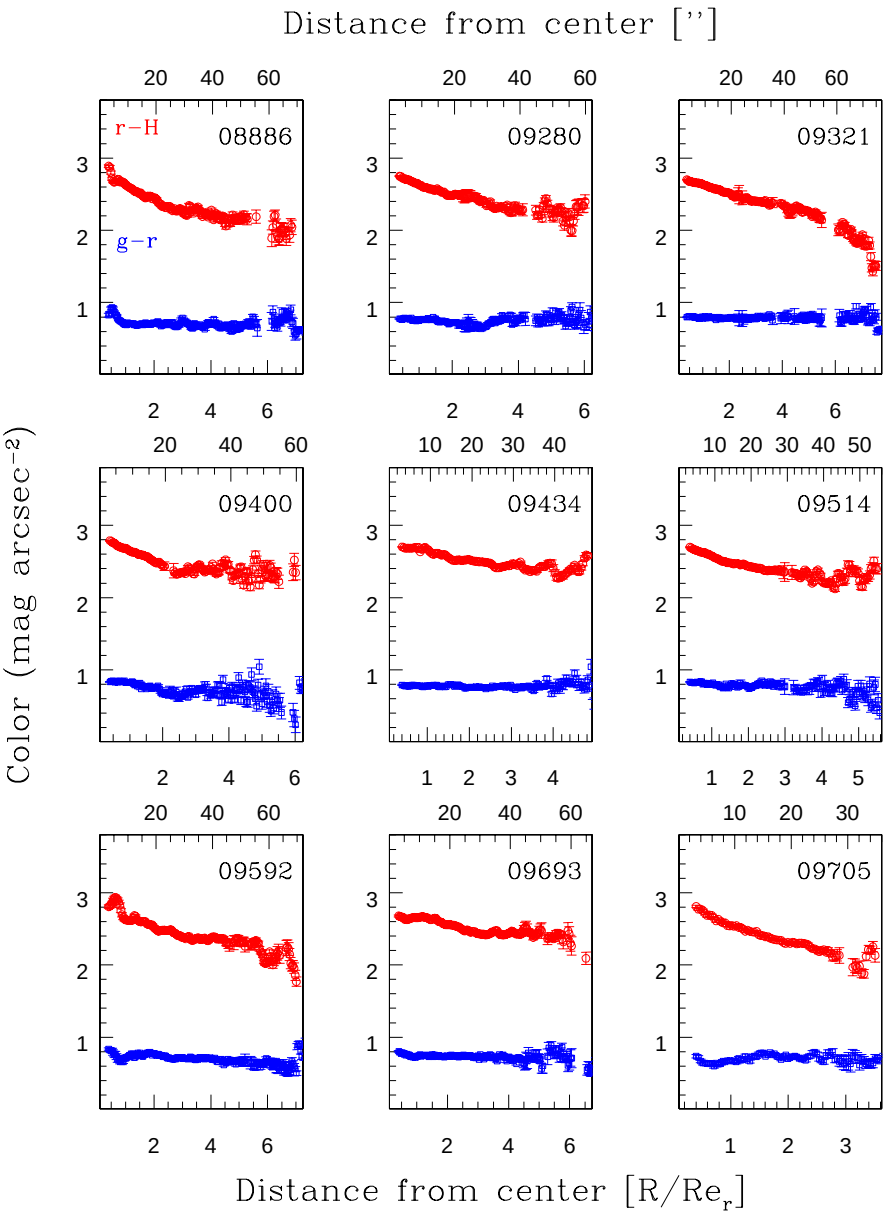
Distance from center ['']
Color (mag arcsec^{-2})
r−H
g−r
08886
09280
09321
09400
09434
09514
09592
09693
09705
Distance from center [R/Re$_r$]

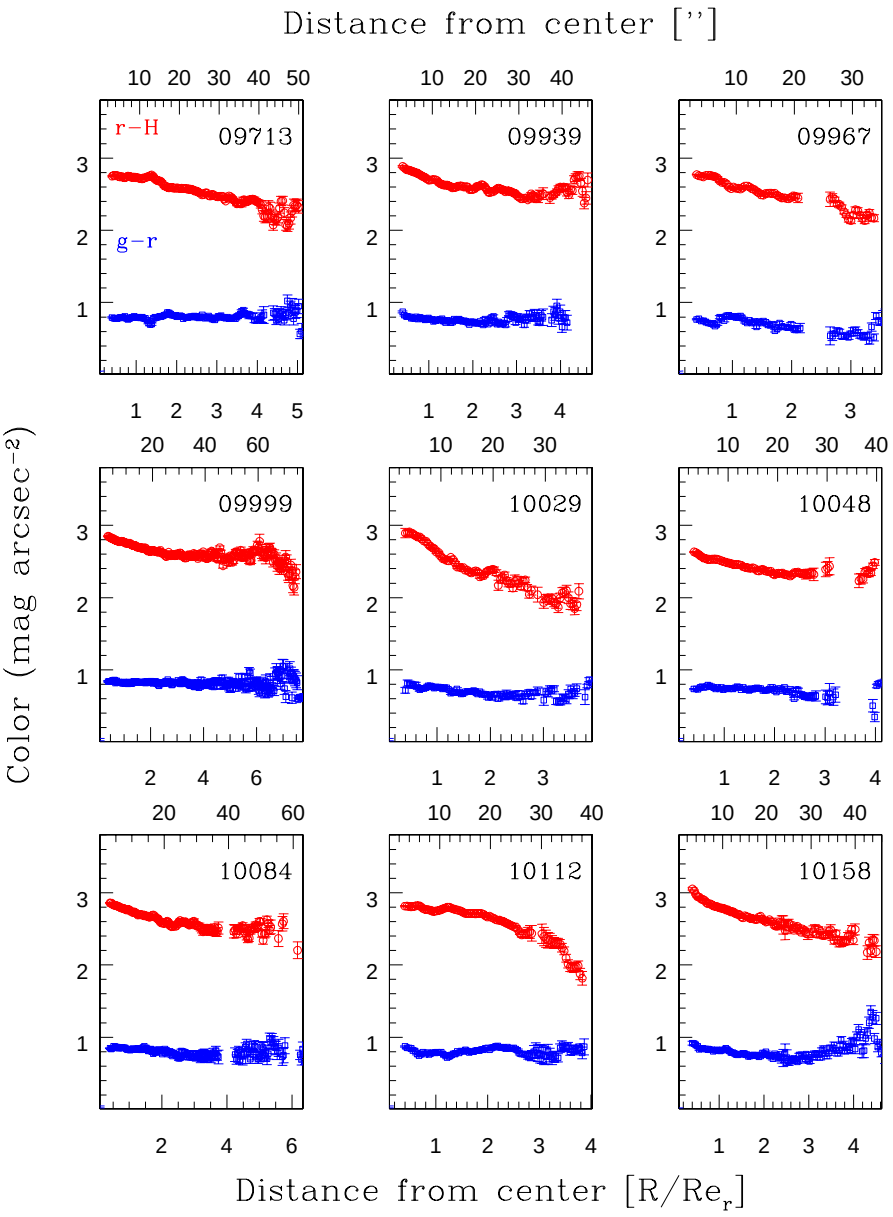
Distance from center ['']
Color (mag arcsec^{-2})
r−H
g−r
09713
09939
09967
09999
10029
10048
10084
10112
10158
Distance from center [R/Re$_r$]

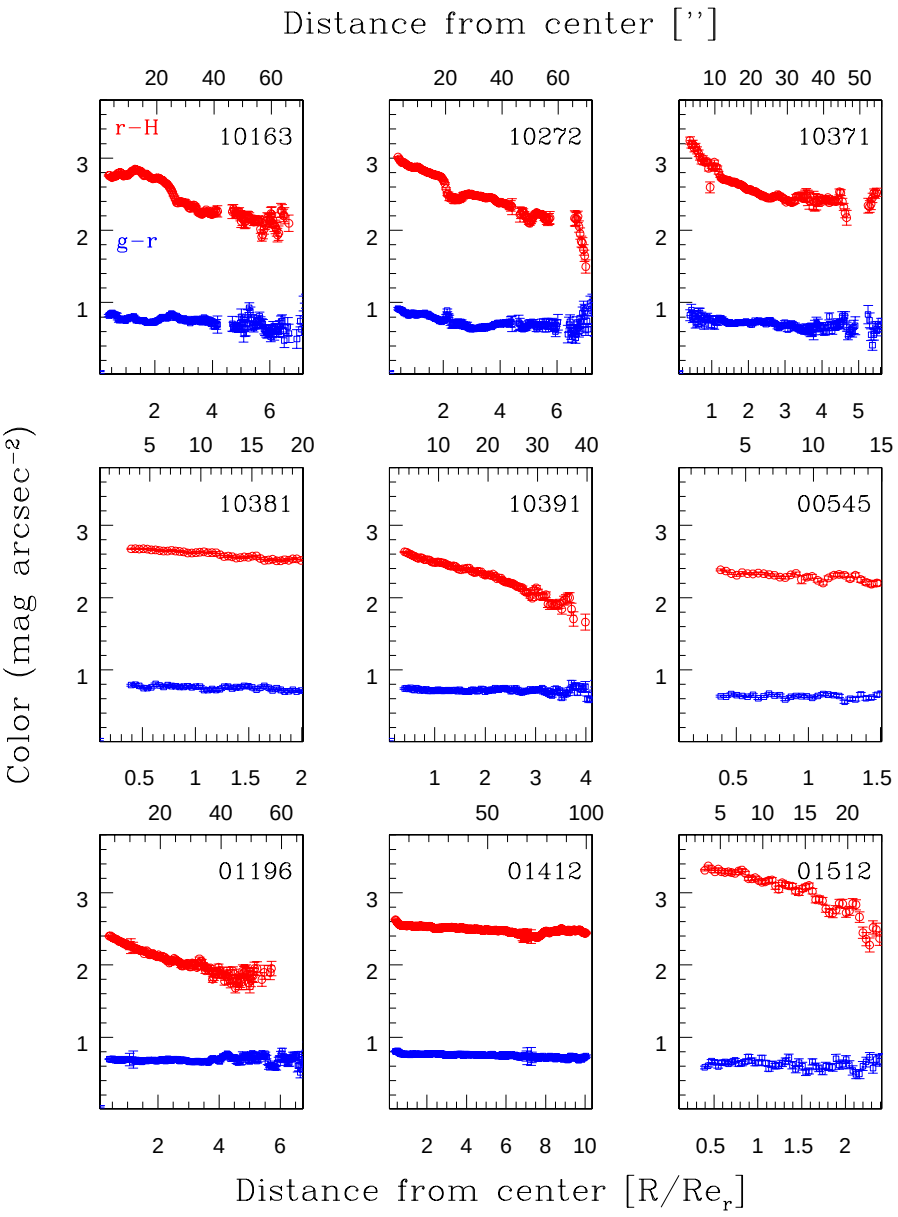
Distance from center ['']
Color (mag arcsec^{-2})
r−H
g−r
10163
10272
10371
10381
10391
00545
01196
01412
01512
Distance from center [R/Re$_r$]

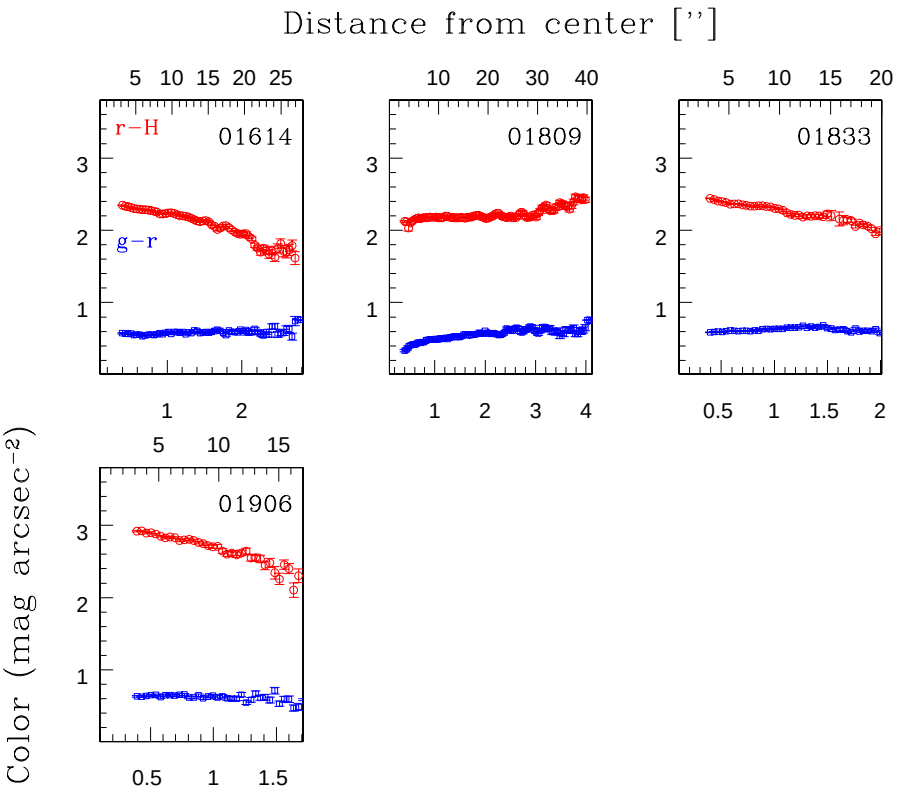
Distance from center ['']
Color (mag arcsec^{-2})
r−H
g−r
01614
01809
01833
01906
Distance from center [R/Re$_r$]

2.4.7 Radial Binning

To increase the signal per color bin, we average colors in six radial bins, scaled by the r-band half light radius. The binning scheme is noted in Table 2.5. If the surface brightness error at any radial point exceeds 0.1 mag, that radial point or region is excluded from the analysis. We also ensure that each binning region contains at least 5 radial points, otherwise that region is excluded from further analysis.

Table 2.5: Binning Scheme

Bin	Radial range
1	$0.0 < r/R_e < 0.5$
2	$0.5 < r/R_e < 1.5$
3	$1.5 < r/R_e < 2.5$
4	$2.5 < r/R_e < 3.5$
5	$3.5 < r/R_e < 4.5$
6	$4.5 < r/R_e < 5.5$

Each galaxy is also coarsely subdivided into an inner and outer radial region as follows. The separation radius between the two regions is chosen at the most prominent inflection point in the surface brightness profile. We find a well-defined change in the slope of the surface brightness profile for $\sim$50% of the sample, with the majority having a break between 0.8 or 1.2 R_e. We have thus chosen the inner radial regions to be within 0.8 Re and the outer radial region to be from 1.2 R_e to the outer radial cutoff. We have applied this characterization to all galaxies in our sample. Fig. 2.3 shows an example of the chosen inner and outer transitions, with a dashed line at 0.8 and at 1.2 R_e. While we wish to sample distinct physical regions with this separation into inner and outer regions, we do not distinguish regions based on model fitting of galactic components (i.e. disk and bulge). Analysis of stellar populations of discrete galactic components will be discussed in § 3. Here we focus on a model-independent analysis of the SB profiles. For clarity, when we wish to discuss our central-most colors, we

refer to a 'central' region which designates the central binning region above (r > 0.5 R_e) and when comparing inner and outer regions we refer to an 'inner' region (r > 0.8 R_e).

2.5 Determination and Range of Galaxy Properties

Our analysis of SP gradients relies on correlations of global galaxy properties, such as environmental density, stellar mass, and light concentration. Prescriptions for determining these properties are given below and the values for each galaxy in our sample are listed in Table 2.6.

Our definition of local environment uses a three-dimensional number density based on the mean distance of the six nearest neighbors. These calculations were kindly provided by Jesse Miner. To construct a density field, the Updated Zwicky Catalog (Falco et al. 1999, hereafter UZC) is used, which is 95% complete to a limiting magnitude of $m_{Z_w} = 15.5$ mag. A three-dimensional position in a Cartesian coordinate system of each galaxy in our sample is assigned, based on its sky position and recessional velocity (using a value for the Hubble constant of $H_o = 75$ km s^{-1}). The "local" region of the galaxy is considered a sphere with the mean distance of the six nearest neighbors used as its radius. The number of objects contained within the sphere is divided by the physical volume of the sphere to obtain a local number density around each of our S0 galaxies in units of Mpc^{-3}. At large heliocentric distances, the catalog only includes the bright end of the luminosity function, thus biasing our densities toward low values. To correct for this effect, our densities are multiplied by a luminosity function correction factor (the ratio of the observable luminosity function at 3,000 km s^{-1} to that of the observable luminosity function at the galaxy's redshift). However, for objects with cz > 9000 km s^{-1}, the luminosity function correction factors become large (greater than factors of 3) and are thus less reliable. Fortunately, for a study of nearby S0 galaxies, this is not a major concern - only 8 out of 59 galaxies

fall beyond this redshift range. Galaxies with cz < 3000 km s^{-1} (17 galaxies in our sample) have larger error in their environmental density measurement due to the large peculiar velocities that yield uncertain line-of-sight distances. In clusters, the high internal velocity dispersion will bias cluster number densities towards lower values. The distribution in environmental densities for our sample covers a range in environment, from -2.2 log Mpc^{-3} to 1.23 log Mpc^{-3}, and has a median value of -0.67 log Mpc^{-3}. The dotted vertical line in Fig. 2.6 denotes the typical density for a galaxy in a small group (Giuricin et al. 2000). We note, however, that these are number densities based on the 6 nearest neighbors and do not provide a perspective on the more global environmental membership (i.e. galaxies in the outskirts of clusters could have a lower number density than the dotted line). Our sample is slightly underrepresented in the cluster regime; the only S0 galaxies in rich clusters are the 8 Virgo cluster galaxies.

Model-dependent bulge-to-disk ratio estimates may carry large systematic errors due to the subjectivity of profile fitting functions (MacArthur et al. 2003). Alternatively, the galaxy light concentration parameter gives a non-parametric indication of the bulge-to-disk ratio (Kent 1985). It is computed as:

$$C_{28} \equiv 5 \log(r_{80}/r_{20})$$

where r_{80} and r_{20} are the radii within which 80% and 20% of the total light is contained (Courteau 1996). The total magnitudes and subsequent 80% and 20% radii have been calculated as described in § 2.4.6. Concentration values for our sample galaxies range from $C_{28} = 2.8$ to 5.5 with a median value of 4.7 as shown in Fig. 2.6. For reference, a pure exponential disk corresponds to $C_{28} \sim 2.8$.

Total stellar masses for our galaxies were calculated from total g and r magnitudes (described in § 2.4.6) and using the mass-to-light ratio prescriptions of Bell et al. (2003). Distances to calculate mass of the galaxies were corrected for Virgo flow and the Great Attractor as provided by the NED[3] for all galaxies other than Virgo cluster

[3]The NASA/IPAC Extragalactic Database (NED) is operated by the Jet Propulsion Laboratory, California Institute of Technology, under contract with the National Aeronautics and Space Administration

galaxies. A distance of 16.5 Mpc is used for all Virgo cluster galaxies (Mei et al. 2007). We have also calculated masses using Portinari et al. (2004) transformations. Although a disagreement between the two prescriptions is found in both the overall mass scale and the relative scales between different galaxy classes (Kannappan & Gawiser 2007), we find no difference in our results when using Bell et al. (2003) versus Portinari et al. (2004) transformations. Our results hinge at a separation of galaxies into high and low mass groups by their median values and we find no change in the mass groups from the two transformations. We also do not notice a difference in the mass distributions. For the 59 galaxies in the sample, the stellar mass of the galaxies ranges from 1.0×10^7 to 5.1×10^11 $M_\odot$, with a median value of 1.0 x 10^{11} $M_\odot$ as shown in Fig. 2.6.

We intentionally selected galaxies to cover a range in concentration, mass, and environmental density. Fig. 2.7 demonstrates the mass/concentration parameter space covered by our sample. Also shown in this figure are the environmental densities of the galaxies, designated by point type. Blue crosses and green dots refer to galaxies in the lowest and highest density environments respectively. Although there is a tendency for S0 galaxies in general to have large mass and high concentration, we strived to maximize this space so that the effects on the stellar populations due to the galaxies' mass and concentration can be separated. Our sample appears to have a trend towards higher density environment for low mass galaxies and, to a lesser extent, lower concentration galaxies. Biases in mass, concentration, and environment will be taken into account when studying stellar population trends.

Recent comprehensive surveys of galaxy luminosities and colors reveal that galaxies occupy two distinct regions in color-stellar mass space, which have been noted as the "red sequence" and the "blue sequence" (Strateva et al. 2001; Kauffmann et al. 2003; Bell et al. 2004; Kannappan et al. 2009a). Although S0 galaxies generally fall into the red sequence, studies have shown that this morphology-color correspondence fails for low mass S0s (Kannappan et al. 2009b). Fig. 2.8 shows u-r (Petrosian magnitudes from SDSS) color versus stellar mass calculated using Portinari et al. (2004). The

dotted line shows the boundary between red and blue sequences. This line is adopted from Kannappan et al. (2009b) but with a mass offset of a factor of 1.8 greater here to account for differences in mass scales. We use Portinari et al. (2004) mass transformations here in order to easily adapt the line from Kannappan et al. (2009b). All but one S0 galaxy (UGC 9003) in our sample fall in the red sequence.

Table 2.6: Derived Global Properties

Name	Concentration	Mass($M_\odot$)	Local Density (log Mpc^{-3})
UGC04330	4.4	1.22e+11	0.40
UGC04596	5.3	1.02e+11	-1.41
UGC04599	4.4	6.97e+09	0.29
UGC04631	4.9	3.88e+10	0.45
UGC04639	4.7	2.29e+11	-1.22
UGC04737	4.7	4.92e+10	-0.07
UGC04869	4.7	1.87e+11	-0.29
UGC04901	4.2	3.62e+11	0.43
UGC04910	4.9	3.24e+11	0.94
UGC04916	5.3	1.95e+11	-0.72
UGC04989	5.0	6.09e+10	-0.87
UGC05075	5.1	9.02e+10	-0.50
UGC05094	5.3	3.56e+11	-1.49
UGC05182	5.3	3.10e+11	-1.12
UGC05403	4.1	1.32e+10	-2.17
UGC05419	4.7	2.35e+11	-0.60
UGC05503	3.7	1.02e+10	0.31
UGC05568	4.1	3.10e+10	-0.95
UGC05766	4.2	7.33e+10	-0.29
UGC05952	4.5	1.15e+10	0.20
UGC08800	3.2	1.03e+09	-1.26

Table 2.6: Derived Global Properties

Name	Concentration	Mass($M_\odot$)	Local Density (log Mpc^{-3})
UGC08886	4.2	1.26e+11	-0.84
UGC08986	3.5	4.14e+09	-0.13
UGC08997	4.5	2.07e+11	-0.47
UGC09003	2.9	8.42e+09	2.00
UGC09087	4.0	7.29e+10	-0.32
UGC09156	4.7	4.43e+11	-0.25
UGC09212	4.9	1.99e+11	-1.93
UGC09280	5.2	2.57e+11	0.11
UGC09321	5.0	4.58e+11	-0.39
UGC09387	4.5	3.45e+10	-1.80
UGC09400	4.8	2.66e+11	-0.67
UGC09434	4.5	1.27e+11	-1.61
UGC09514	5.3	2.31e+11	-1.07
UGC09592	5.1	2.22e+11	-0.36
UGC09693	5.2	1.83e+10	-0.34
UGC09705	4.1	7.68e+10	-1.08
UGC09713	3.8	1.16e+11	-1.42
UGC09939	5.2	4.26e+10	-1.82
UGC09967	4.9	8.97e+10	-2.12
UGC09999	5.2	4.11e+11	-0.56
UGC10029	4.9	3.05e+11	0.20
UGC10048	5.0	5.57e+10	-1.08
UGC10084	4.8	5.10e+11	-0.98
UGC10112	5.4	2.05e+11	-1.08
UGC10158	3.7	4.98e+11	-1.54
UGC10163	4.7	2.08e+11	-1.45

Table 2.6: Derived Global Properties

Name	Concentration	Mass($M_\odot$)	Local Density (log Mpc^{-3})
UGC10272	5.3	1.11e+11	-1.24
UGC10371	4.2	2.26e+11	-1.31
UGC10381	5.1	2.19e+11	-0.23
UGC10391	4.8	2.89e+10	-1.05
UGC0545	3.3	5.14e+08	0.34
UGC1196	3.9	3.59e+09	0.95
UGC1412	4.2	2.03e+10	0.68
UGC1512	4.2	2.34e+08	0.74
UGC1614	2.8	1.16e+09	0.58
UGC1809	4.2	1.29e+10	-1.38
UGC1833	3.7	1.20e+09	-0.83
UGC1906	3.3	9.02e+06	1.23

2.6 Stellar Population Models

A comparison of the observed NIR and optical galaxy colors with colors inferred from stellar population synthesis models covering a range in age and chemical composition allows for the determination of light-weighted mean ages and metallicities. The combination of a primarily age sensitive color (such as g-r) with a primarily metallicity sensitive color (such as r-H) provides a separation in age and metallicity. We use a Bruzual & Charlot (2003, hereafter, BC03) simple stellar population (hereafter, SSP) model with a Salpeter initial mass function and Padova (1994) model isochrones for our analysis. Because an SSP model provides a single age while the observed light is likely composed of more than one coeval population, the derived ages are a light-weighted mean age of the populations contributing to the light. From here on, we

drop the "mean" and refer to these as light-weighted ages and metallicities to avoid confusion with mean ages of multiple radii or galaxies.

Ages and metallicities are easily represented in color-color diagrams, in which a near-IR color (r-H or r-J) is plotted versus an optical color (g-r). For example, we show in Fig. 2.9 the color-color diagram for UGC 10391. The color-color diagrams for all the galaxies in our sample are shown in the electronic version. The central binning region for the galaxy is designated by a green star, each subsequent radial bin is a small filled circle, and consecutive radial bins are connected by a solid blue line. Overplotted is a BC03 SSP model grid. Red dashed lines represent model lines of constant age increasing, left to right, from 0.8 Gyr to 13.8 Gyr. Blue dotted lines represent model lines of constant metallicity increasing, bottom to top, from [Z/H] = -2.2 to +0.5. The error bars for each radial bin represent the standard error in the mean based on the scatter in color of the radial points within the designated bin added in quadrature to the sky effect (error generated by changing the sky value by $\pm 1\sigma$ systematic sky error at each radial point, see § 2.4.3 for a description of the measurement of sky effects). This example shows a galaxy whose light-weighted metallicity and light-weighted age decrease and increase respectively from the center of the galaxy outward. The galaxy becomes clearly bluer in r-H at larger radii and stays roughly constant in g-r, thus crossing over lines of constant age with increasing radius and indicating older ages in the outer regions of the galaxy. For reference, we show a color image of this galaxy in Fig 2.1a.

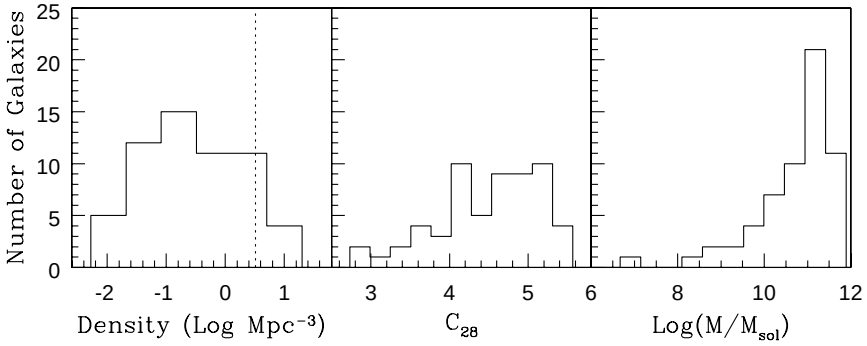

Figure 2.6 Left: Histogram of environmental number densities (in log Mpc^{-3}) for the sample of 61 galaxies. The vertical dotted line denotes the typical density for a galaxy in a small group. Middle: Histogram of the galaxy light concentration, C_{28}, for the sample of 61 galaxies. Right: Histogram of total stellar masses (in log solar mass) for the sample of 59 galaxies.

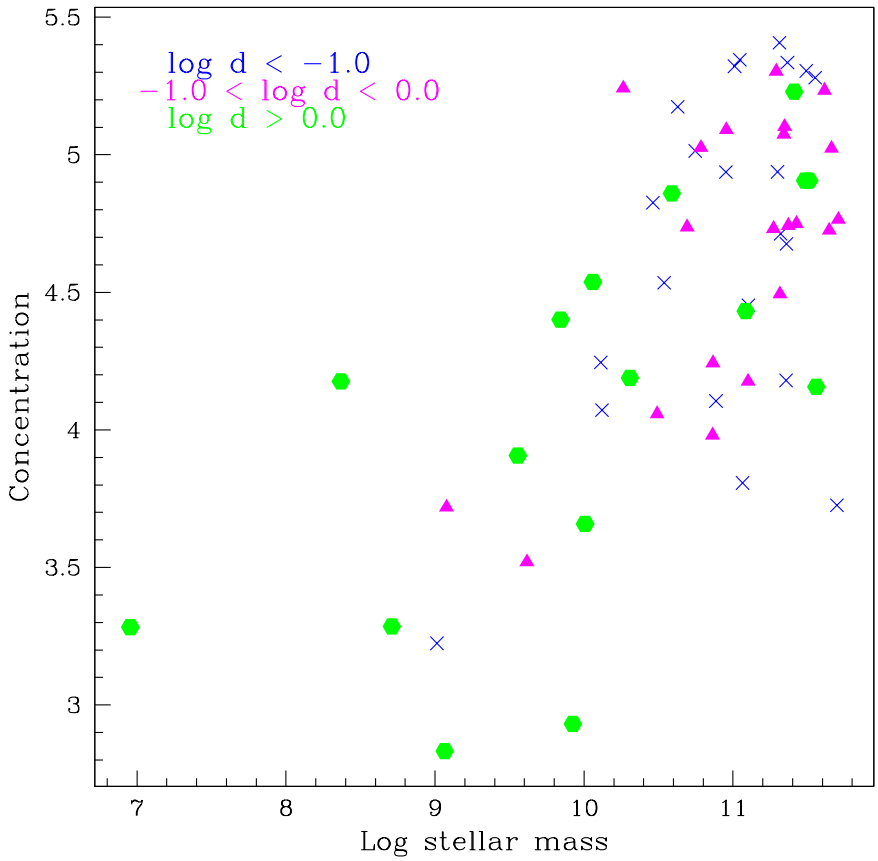

Figure 2.7 Total stellar mass (in log solar mass) is plot versus light concentration (C_{28}) for the entire sample of 59 galaxies. The point style designates local environmental density in Mpc^{-3}(green circles: d > 0.0, magenta triangles: -1.0 < d ≤ 0.0, and blue x's: d ≤ -1.0).

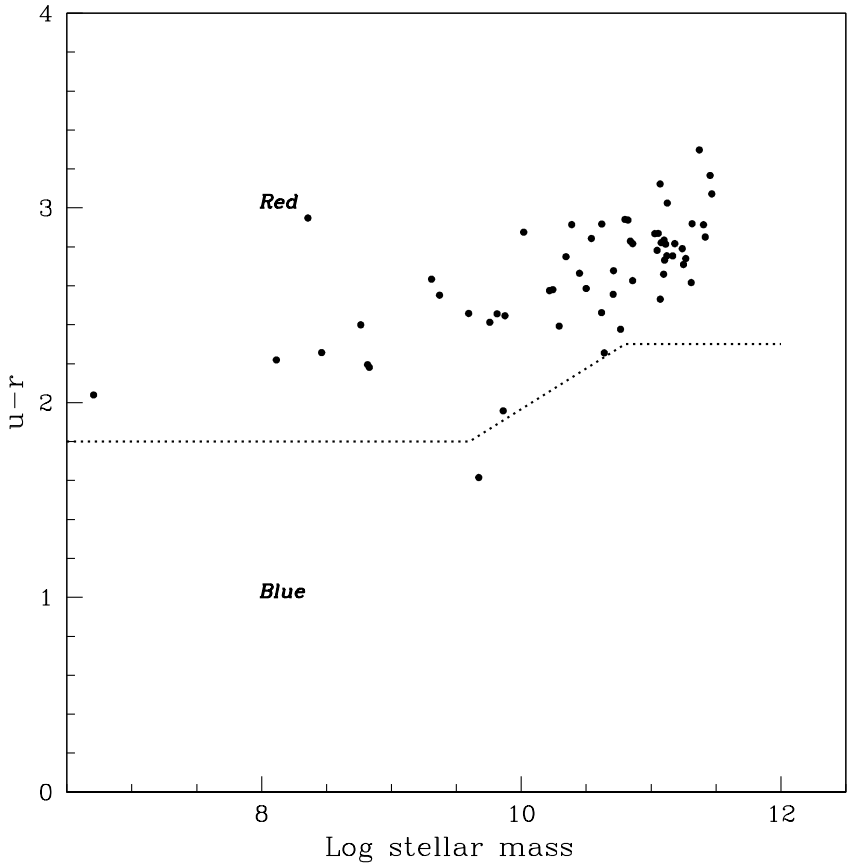

Figure 2.8 Total color (u - r) versus the stellar mass, in units of log solar mass. The dotted line, obtained from Kannappan et al. (2009a), was derived to separate the red and blue locus's of galaxies. All but 1 galaxy in our sample lie in the red sequence.

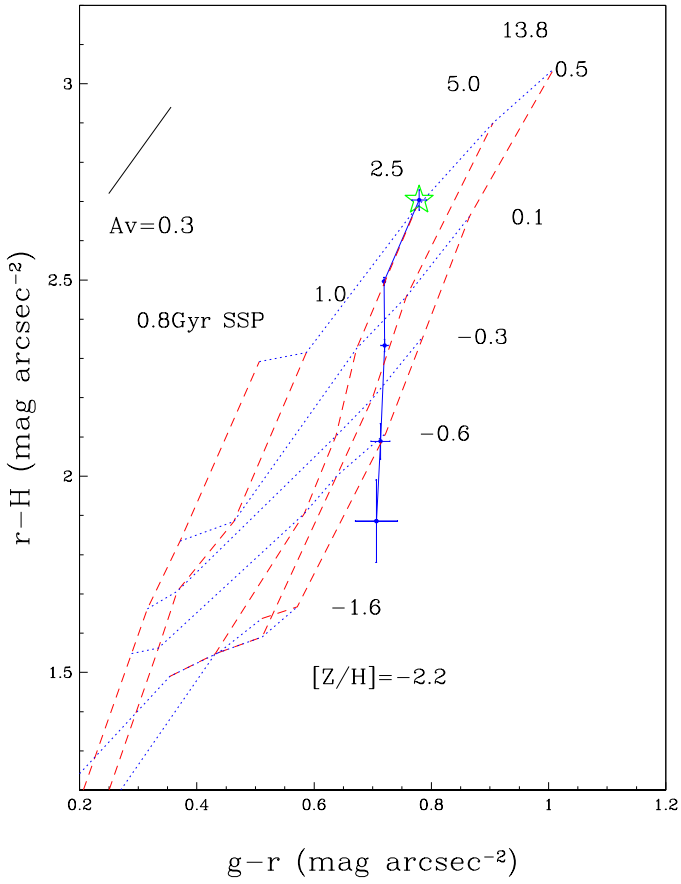

Figure 2.9 An example r-H vs. g-r color-color diagram is shown for UGC 10391. Galaxy colors are overlaid on a BC03 SSP model grid. Model lines of constant age (shown as dashed red lines) increase, left to right, from Age_{SSP} = 0.8, 1.0, 2.5, 5.0, and 13.8 Gyr. Model lines of constant metallicity (shown as dotted blue lines) increase from bottom to top from [Z/H] = -1.6, -0.6, -0.3, 0.1, and 0.5. Small filled circles are the average colors of the galaxy's radial bins (the binning scheme is noted in Table 2.5) and each bin is connected by the solid line. The central binning region is designated by a green star. The error bars on each radial bin represent ± 1 sigma, where sigma is the standard error in the mean based on the scatter in color for each radial point in the designated bin added in quadrature to the sky error as discussed in section §2.4.3. A foreground screen dust model color vector with Av = 0.3 is plotted in the upper left corner.

2.6.1 Star Formation Histories and Model Uncertainties

Since our analysis of stellar population trends in S0s hinges on the reliability of derived ages and metallicities, it is important to understand how differences between adopted stellar population models could affect our results. The SSP models that we use for our analysis predict the evolution in colors (and spectrum) of a coeval population of stars with the same chemical composition and specified initial mass function. While this is clearly an over-simplification of the actual star formation histories in S0 galaxies, it represents a straightforward way to obtain a *light-weighted* age and metallicity. However, we must test how our analysis might be affected by the use of more complex star formation histories. Since an SSP is one extreme star formation history (equivalent to a single burst), we also compute models for the other extreme, a constant star formation history with a quenching of star formation at various ages, and compute models for the intermediate case of exponentially declining star formation. We thus consider populations that are composed of a superposition of SSPs, born at different epochs. Using the *csp-galaxev* program provided by BC03, we take an SSP model with constant initial mass function and fixed metallicity and convolve it with the given star formation history (exponentially declining and constant). We compute the convolved models for a range of metallicities and time constants, τ, (for the exponentially declining models) or star formation truncation times (for the constant models). In both cases, the age of the galaxy (or time that star formation began) is fixed to 13 Gyr. We show a color-color diagram based on the two sets of models in Fig. 2.10. The constant star formation history is shown in blue, the exponentially declining star formation history is in red, and the SSP model is in black. The same SSP model grid is used throughout the paper. The meaning of the "age" of a stellar population for each set of models is different. For the exponentially declining models, we plot lines of constant τ. For the constant star formation models, the age is represented by truncation times, or how long the star formation has lasted since 13 Gyr. The model grid edges are similar between the three model sets. For example, the constant star formation model with a truncation time of 0.1 Gyr and the exponentially declining

model with a τ of 0.1 Gyr are similar to the SSP model with an age of 13.8 Gyr, all lying and nearly overlapping near the right edge of the grids. The general shape of the lines, especially those of constant age, do not vary with star formation history. Thus, an analysis based on relative age trends with radius will be robust concerning star formation histories. Lines of constant metallicity do vary in slope for the 3 different SFHs. However, the variations are small compared to the large metallicity gradient that is observed in our sample.

Uncertainties in stellar population synthesis modeling have been studied throughout the literature (Trager et al. 2000; Schiavon et al. 2002; Shapley et al. 2005; Conroy et al. 2009). Theoretical model uncertainties in the age and metallicity zeropoint can be caused by errors in the calibration of ages and metallicities from globular clusters. Another potential concern is the difference in elemental abundance ratios between the population being studied and the stars from which the models are based. Massive S0 galaxies are known to have a higher abundance of alpha elements, relative to iron, as compared to solar neighborhood stars (Serra et al. 2008; Thomas et al. 2005). Thus when using stellar population models that do not account for non-solar abundance ratios, derived ages and metallicities are affected by errors in the theoretical stellar evolutionary tracks. Uncertainties in the input model parameters, such as the effective temperature of the isochrones, giant stars or binary stars in the luminosity function, our understanding of late evolutionary phases, as well as the theory for convection and the effects of rotation and diffusion, may induce additional, unknown systematic errors.

Much of our analysis in this study is concerned with relative ages - comparisons of inner and outer regions of galaxies and comparisons among galaxies. If we compare two galaxies with similar metallicities, but different ages, their derived relative ages will not be greatly affected by model zero point errors. However, when two populations differ in metallicity as well as in age, then if the model zero point errors are metallicity dependent, differential ages between metal-poor and metal-rich populations are less secure. Indeed, there appears to be a strong metallicity gradient with radius for most

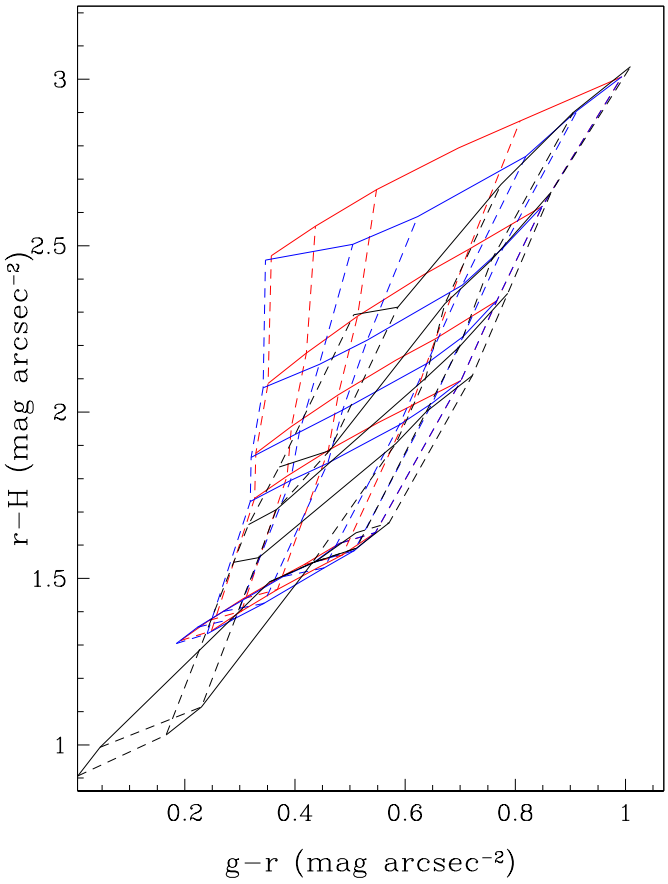

Figure 2.10 Plotted are r-H vs. g-r color-color diagrams of BC03 models using various star formation histories. Overlaid are models using a constant SFH history (blue), an exponentially declining SFH (red), and a simple stellar population (black). Both the constant and exponential models assume a maximum age of 13 Gyr. Lines of constant age are solid and lines of constant metallictiy are dotted. Metallicity increases from bottom to top for all 3 models as $[Z/H] = -1.6, -0.6, -0.3, 0.1, 0.5$. Age lines for the SSP model are as in Fig. 2.9. Age lines for the exponential model increase from left to right as time constant $\tau = 100, 13, 6.5, 4.0, 3.0$, and 0.1. Age lines for the constant star formation model are from right to left as time that star formation occurred (since 13 Gyr ago) = 0.1, 10, 12, 12.8, 12.9, and 13 Gyr.

of our sample. Therefore, our derived age trends with radius are subject to metallicity-dependent zero point issues and we take this into consideration when examining our results.

Differences in handling uncertain physics by model makers leads to large differences in the interpretation of galaxy colors from varying SSP models. Although it is difficult to estimate uncertainties in the derived stellar population parameters (like age and metallicity), comparing the BC03 models that we use here with other available models suggests how much our results are dependent on our choice of stellar population models. The treatment of advanced stages in evolution, such as the Thermal-Pulsating Asymptotic Giant Branch phase (TP-AGB), has received much attention in the past decade. TP-AGB stars are extremely bright and dominate the NIR light of a galaxy following a burst of star formation, but are difficult to model theoretically because of the combined effects of thermal pulses, changes from heavy element dredge-up, and mass loss (BC03). The stellar population synthesis models of Maraston (2005) use a different prescription for the TP-AGB phase than BC03 and the effect on the model colors has been demonstrated in the literature (Tonini et al. 2009). A revised version of the Bruzual and Charlot stellar population synthesis code has been developed (Charlot & Bruzual 2009, private communication) which includes a new prescription for TP-AGB evolution of low and intermediate mass stars following Marigo & Girardi (2007) and uses tracks from models with updated input physics from Bertelli et al. (2008). Eminian et al. (2008) has demonstrated a significant change with the new Bruzual and Charlot models in NIR model colors for intermediate populations.

We compare the BC03 SSP models to the SSP models of Maraston (2005) and Charlot & Bruzual (2009) in Fig. 2.11. Maraston (2005) and Charlot & Bruzual (2009) SSP model grids are shown in the left and right panels, respectively. The BC03 model grid is shown in each panel (in black) for reference. All 3 models cover similar ages and metallicities (see figure caption for details), but the lowest age that we plot here (0.8 Gyr) is not available for the lowest metallicity (-2.25 dex) in the Maraston (2005) model. The Charlot & Bruzual (2009) models appear to be a closer match to the

Maraston (2005) models than the earlier BC03 version. Both Maraston (2005) and Charlot & Bruzual (2009) models are redder in r-H, which has been found to provide a closer match to observations of star forming galaxies (Eminian et al. 2008). Despite large differences in color at low ages, we find in all models that the lines of constant age are tilted in a similar direction at all ages. We will return to this key point in § 2.7.2. For younger ages ($\lesssim$ 3 Gyr), the lines of constant metallicity in the Charlot & Bruzual (2009) and Maraston (2005) models changes slope (metallicity decreases with increasing age at lower metallicity and younger age) and lines of constant age vary slightly in their dependence on r-H colors. For studies of radial stellar population trends in galaxies, the difference in using the two models will primarily affect the strength of the age gradients, but will not change the direction of the age trends. For older ages, the effect on the strength will be minimal. The PEGASE models of Fioc & Rocca-Volmerange (1997) have also been examined in this color space and the lines of constant age and metallicity were found to be similar, but covering a smaller range in color than BC03. We refer the reader to MacArthur et al. (2004); Lee et al. (2007); Eminian et al. (2008); Tonini et al. (2009) for further discussion on stellar population model comparisons.

We chose to base our analysis for this work on BC03 models because the Charlot & Bruzual (2009) models are still preliminary and not yet publicly available (we were provided the models to test the sensitivity of our results). As well, the BC03 models have been used in the literature for quite some time and have thus become standard. As stated earlier in this section, we chose to use SSP models for comparison with galaxy colors because it represents a straightforward way to obtain a *light-weighted* age and metallicity. We will come back to differences in colors between the models as we discuss our results.

2.6.2 Extraction of Ages, Metallicities, and Gradients

We derive light-weighted ages and metallicities for each radial bin and for the inner and outer radial regions (as defined in § 2.4.7) by fitting BC03 SSP stellar population

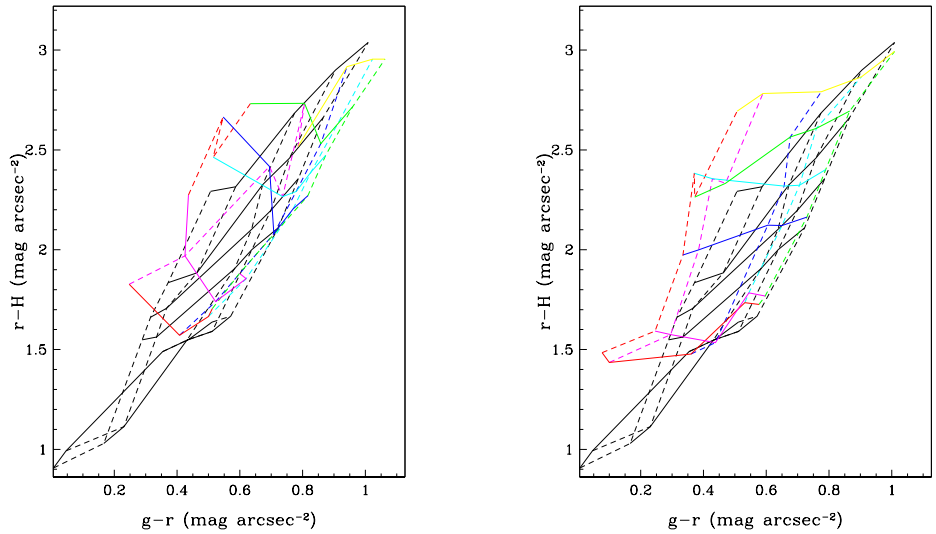

Figure 2.11 Color-color diagrams using the BC03 model (in black) overlaid on other population synthesis models (in color). Lines of constant age and metallicity are represented by dashed and solid lines, respectively, and vary in color according to their values for all but the BC03 model. Maraston (2005) and Charlot & Bruzual (2009) SSP model grids are shown in the left and right panels, respectively. Maraston (2005) ages increase from left to right as 0.8, 2.0, 5.0, 10.0, and 14.0 Gyr SSP. Maraston (2005) metallicity increases from bottom to top as [Z/H] = -2.25, -1.35, -0.33, 0.35, and 0.67 dex. The BC03 and Charlot & Bruzual (2009) SSP model grid have ages and metallicities as in Fig. 2.9.

models to the galaxy colors. We compute a finely spaced BC03 SSP model grid by interpolating linearly between the SSP metallicities and also between the finely spaced ages provided by BC03. From the g-r and r-H (or r-J) color, we determine the ages and metallicities from the model that minimizes the difference between model and observed colors, calculated in quadrature. Due to the uncertainties in extrapolating model colors to larger metallicities and ages and the convergence in colors at large ages, the age and metallicity of a galaxy is set to a maximum of 13.8 Gyr and +0.5 dex, respectively. While the BC03 models actually extend to 20 Gyr, we chose a maximum age of 13.8 Gyr to be more consistent with the current age of the universe

(Hinshaw et al. 2009) (the 20 Gyr and 13.8 Gyr model are similar enough in color to not hinder our analysis).

The uncertainties in the derived ages and metallicities are determined from a Monte Carlo method, similar to that used by MacArthur et al. (2004). Two-hundred realizations of the model fits were performed for each radial bin and inner and outer regions with the colors for each realization drawn from a Gaussian distribution of the errors in each color. The standard error in the mean is based on the scatter in color of the radial points within the designated bin or region added in quadrature to the sky effect. Ages and metallicities for each bin are quoted as the mean of the ages and metallicities computed from each realization. The quoted errors in the derived ages and metallicities for each bin are taken as half the interval containing 68% of the 200 Monte Carlo realizations. If more than 5% of the realizations produced either an age greater than 13.8 Gyr or a metallicity greater than +0.5 dex, we set the error for the entire age measurement to zero, indicating the lack of a measurable error. We note that model fitting errors do not reflect uncertainties in the model itself that were discussed in § 2.6.1. Ages, metallicities, and their uncertainties are listed in Table 2.3 for the inner and outer regions of all galaxies in our sample.

There are 11 galaxies for which both J and H-band images were acquired, enabling a partial consistency check on our extracted ages and metallicities. In Fig. 2.12, we show the derived J-band ages versus the derived H-band ages for both the inner and outer regions. A Kolmogorov-Shmirnov two sample test (hereafter, K-S) on inner and outer region ages of the J-band sample and H-band sample for the 11 galaxies in common reveals a probability of 99% and 81%, respectively, that they are drawn from the same population.

Age and metallicity gradients are determined from a linear least squares fit to the age and metallicity data in the 2nd, 3rd, and 4th radial bins. We avoid the central radial bin due to the greater likelihood of dust contamination and seeing blur; the 5th and 6th bins are avoided due to their greater errors from systematic sky uncertainties. The age and metallicity gradients for each galaxy are listed in the electronic version.

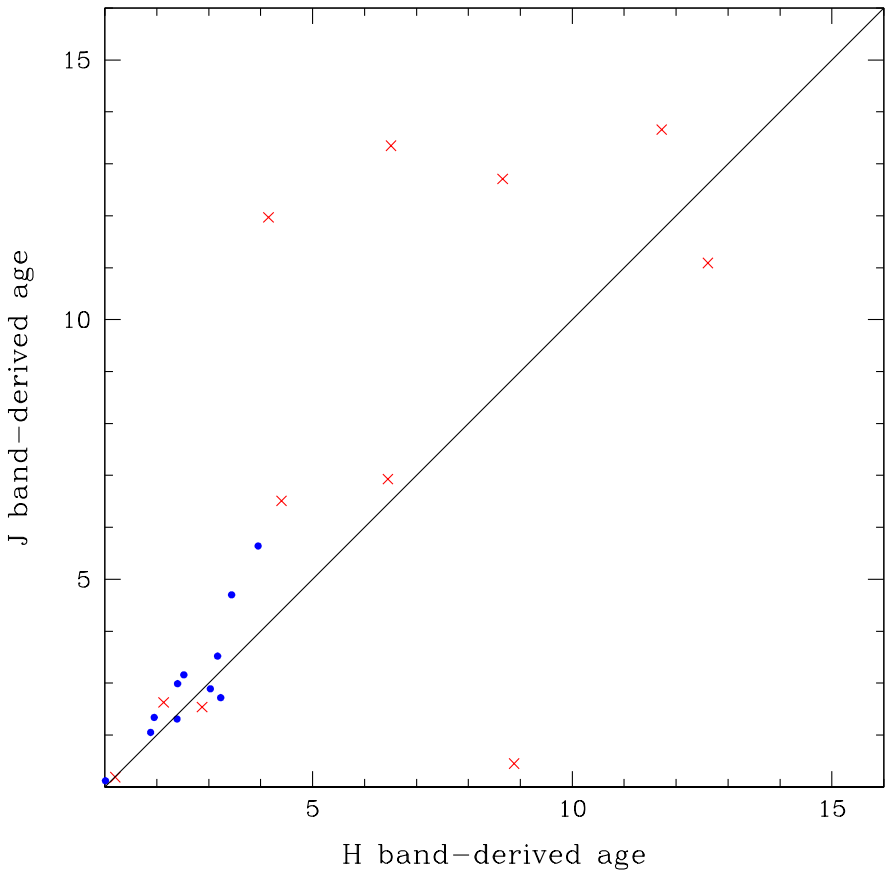

Figure 2.12 Ages derived from the J-band versus ages derived from the H-band for the inner radial region (blue circles) and the outer region (red x's) for the 11 galaxies observed in both H and J-bands.

Because the extracted ages and metallicities were set to a maximum of 13.8 Gyr and +0.5 dex respectively, when an age or metallicity from a bin used to calculate the gradients was set to one these values, the gradient is considered a lower limit.

2.7 Results

The primary goal of our study is to constrain the star formation and chemical enrichment histories of S0 galaxies by mapping light-weighted ages and metallicities from the center out to large radii. We begin with an analysis of the central ages and

metallicities. While sky background removal is clearly the limiting obstacle to accurate photometric colors at large radii, it is a minimal problem in the central region, where the highest signal-to-noise ratio is achieved. In addition, there exists a considerable amount of prior age determinations for the centers of early-type galaxies in the literature, thereby allowing us a useful check on our modeling procedures. On the other hand, it is now clear that the central regions of early-type galaxies can be "contaminated" by relatively recent star formation episodes that may be non-representative of the mean age of the rest of the galaxy (e.g., de Jong & Davies 1997; Sánchez-Blázquez et al. 2007), and hence the mean age derived for the central region may be highly dependent on the aperture size for the age determination. Moreover, PSF differences between different passbands makes the interpretation of surface photometry within the central regions of galaxies problematic. Despite the latter complications, we consider it instructive to begin with an examination of the central ages and metallicities of our sample, and to compare them with corresponding values from the literature, before continuing on with an analysis of the outer regions of our galaxies. We note that our central regions all correspond to a radius of at least 3 arcsec, which should be large enough to alleviate the PSF matching issue.

2.7.1 Central Ages and Metallicities

Galaxy g-r colors are plotted versus r-H for all galaxies in the H-band sample in Fig. 2.13 relative to a SP model grid, where the central bins ($r < 0.5\ R_e$) are designated by a green star. It can be seen that most of our galaxies have central colors that are concentrated in regions of intermediate age and high metallicity relative to the model grid. In the upper and lower panels of Fig. 2.14, histograms are plotted of the extracted central ($r < 0.5\ R_e$) ages and metallicities for the H-band and J-band sample, respectively. The J and H band data for 11 galaxies produce similar age and metallicity histograms. We wish to combine the results of the H and J band data. However, we note non-uniformities in the J-band backgrounds that may increase the possibility for systematic errors compared to the H-band images. Thus, when combining all the

galaxies in our sample, the quoted ages and metallicities for galaxies that have H-band imaging will be based on that band alone.

The distribution of central ages for the combined H and J band data is fairly symmetrical around a mean light-weighted age of 2.7 Gyr, with an rms scatter of $\pm$1.3 Gyr; the median central age is 2.6 Gyr. Thus star formation episodes have occurred in the central regions of a majority of S0 galaxies within the past few Gyr. We can compare this result with data on the central regions of other samples of S0 galaxies from two sources: (1) optical and near-IR photometry (Peletier et al. 1999), and (2) integral field unit (IFU) optical spectroscopy (Sil'chenko 2006), as well as comparing the ages and metallciities of specific galaxies in our sample with spectroscopically derived values. Since the ages of early-type galaxies are typically older for more massive galaxies (Caldwell et al. 2003; Nelan et al. 2005; Sánchez-Blázquez et al. 2007), the comparison of central ages between two S0 galaxy samples requires that we compare galaxies of similar mass (absolute luminosity). The typical luminosities of our sample galaxies, as measured by the absolute B magnitude, are similar to those of Peletier's and Silchenko's samples, with the median M_B for our sample being $\sim$0.4 mag brighter than for Peletier and Silchenko. Thus, the stellar masses cannot be responsible for the any age differences between the samples.

From broadband optical and near-IR photometry, Peletier et al. (1999) found a spread of about 1-2 Gyr and a mean light-weighted age of 9 Gyr for bulges (at 1 bulge K-band effective radius) in a sample of twenty S0 and early spiral galaxies (to Sbc). The "bulges" of Peletier et al. (1999) are closest in observed radius to our 2nd binning region. Consequently, we compare the mean age of 2.8 $\pm$1.3 Gyr for the 2nd binning region of our sample with the 9 Gyr mean age found in Peletier et al. (1999). The Peletier et al. (1999) ages are substantially older than ours. However, the mean age provided by Peletier et al. (1999) does not include the seven bluest, hence youngest, bulges in his sample, three of which are S0 galaxies. More importantly, Peletier et al. (1999) studied highly inclined galaxies and masked out the disk from their extracted ages and metallicities, hence their results truly apply to bulge light at 1 R_e, while our

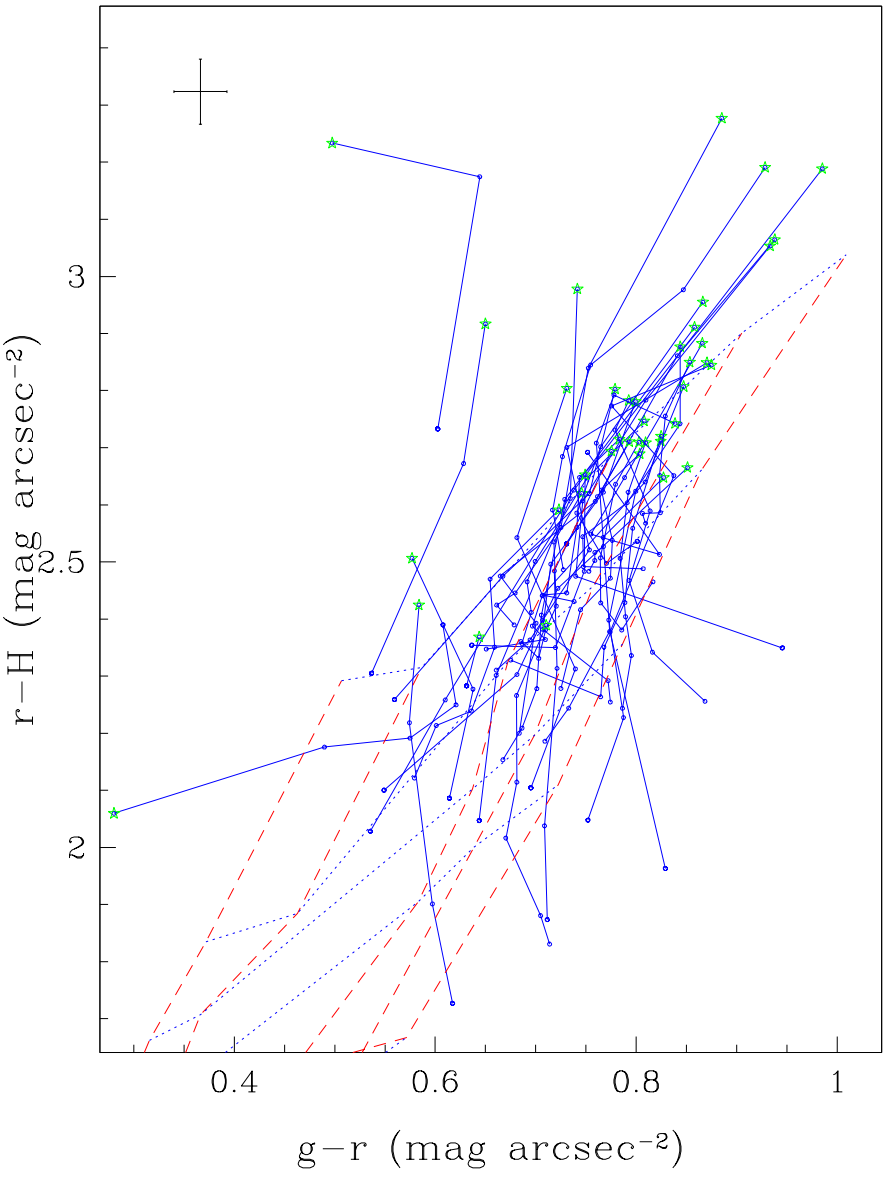

Figure 2.13 Color-color diagram for the entire sample of 41 S0 galaxies in the H-band sample. The model grid is the same as in Fig. 2.9. The top error bar in the upper left corner represents the average of the error at each radial bin (see Fig. 2.9) and for each galaxy.

results apply to bulge and disk light mixed together within 0.5 to 1.5 R_e. Thus, the difference in ages may be partly due to the fact that Peletier et al. (1999) isolate the bulge light, while we have disk light mixed in. Moreover, the difference in mean ages may be partly attributed to the difference in stellar population models. Peletier et al. (1999) have used Vazdekis et al. (1996) SSP models to compute the ages and note that the use of Worthey (1994) models gives a significantly smaller mean age of 2 Gyr for their sample.

The IFU spectroscopic sample of 58 lenticular galaxies studied by Sil'chenko (2006) yielded ages derived from Lick indices that are in closer agreement with ours. Specifically, she reports median ages within the unresolved nuclei of 3.7 and 6 Gyr respectively for galaxies in sparse and dense environments, while the median ages for 'bulges' (extracted from an annulus of 4 to 7 arcsec) are 4.8 and 8.3 Gyr for sparse and dense environments. With the exception of the few Virgo galaxies, our sample mostly corresponds to the sparse environment in Sil'chenko (2006), and our central ages are extracted from a region that is somewhat between the unresolved nucleus and the 4-7 arcsec bulge in light-weighted average. In any case our age distribution is a closer match with that of Sil'chenko (2006), who uses the Thomas et al (2003) models for age determinations.

We can also compare our mean central metallicities with those of Peletier et al. (1999) and Sil'chenko (2006). The mean and median central metallicities of our sample galaxies are [Z/H]= 0.4 dex and 0.5 dex, respectively. The median value is preferable here, because it is more robust to the upper limit we place on metallicities at +0.5 dex; the mean will be shifted toward lower values because the high end of metallicities is artificially set to a lower value, i.e. +0.5 dex. These results are again in good agreement with Sil'chenko (2006), who finds a median metallicity for her nuclei and bulges of +0.4 and +0.2, respectively. Visual inspection of Fig. 3a in Peletier et al. (1999) reveals a mean metallicity around solar. In contrast, we obtain a substantially higher value with [Z/H]=+0.3 for our second radial bin. Accounting for the effect of the upper limit on metallicities would only make our value higher.

Although our sample contains no overlapping galaxies with Peletier et al. (1999) or Sil'chenko (2006), independent ages and metallicities from spectroscopic studies offer direct comparisons for a few galaxies in our sample. Kuntschner et al. (2006) provide Lick index line strength measurements for UGC 5503. Comparison of their Hβ and Fe5015 index measurements to a Vazdekis (1999) stellar population model (by eye) yields a light-weighted age of 1.6 Gyr for the inner 25". Our average extracted age for this region (comparable to our first two radial bins) is similar at 0.9 Gyr. The age estimates for UGC 10048 by Caldwell et al. (2003) range from 4.9 to 7.9, depending on the indices used. The metallicity ranges from -0.1 to 0.1. Our extracted age ranges from 2.5 Gyr in the inner region to 2.6 Gyr in the outer region and our metallicity from 0.4 in the inner region to 0.2 in the outer region. Our results are clearly offset to younger age relative to Caldwell et al. (2003). However, their spectra were extracted from a 3″wide long slit spectrum, using variance weighting, thus it is difficult to compare specific regions in the galaxy. Caldwell et al. (2003) also find an age of ∼1.8 Gyr and a metallicity range of ∼-0.4 for VCC 1614. Our extracted age ranges from 1.0 Gyr in the inner region to 3.6 Gyr in the outer region and our metallicity from 0.5 in the inner region to -0.7 in the outer region for this galaxy. In general, there is good agreement between our extracted ages and metallicities and other spectroscopic studies.

Fig. 2.13 shows the center of many galaxies lying off the model grid toward larger r-H values. The colors of these points may be explained by both modeling and dust effects. As described in § 2.6.1, when stellar population models use improved treatments of TP-AGB evolution, they predict redder colors. Therefore, if the Charlot & Bruzual (2009) code were used instead in Fig. 2.13, the central points of only a few galaxies would lie off the model grid. Using Charlot & Bruzual (2009) models, we would derive lower metallicities and slightly older ages (the mean age would be shifted closer to 5 Gyr) for the central regions. The colors of the remaining off-grid points may be understood by reddening from dust. Dust is a possible source of bias in photometric studies. For many S0 galaxies, dust effects mainly the central regions

(Peletier et al. 1999; Wiklind & Henkel 2001; Fritze v. Alvensleben 2004), although dust lanes are observed in 3-color optical images in the outer regions of a few galaxies in our sample. While we have corrected our galaxy colors for Galactic foreground extinction, they have not been corrected for internal extinction. To estimate the effect of internal extinction, a reddening vector for a foreground screen dust model with $A_v = 0.3$ is shown in the upper left corner of the color-color diagrams. Dust would thus lead to higher extracted ages and metallicities than is the case when the colors are properly dereddened. The effect that internal dust reddening has on photometrically derived ages and metallicity is clearly demonstrated and discussed in Peletier et al. (1999). Their Figure 3a shows a large shift, parallel to the reddening vectors, in colors from the center of the galaxy to one R_e. Ages appear to shift from $\sim$ 11 Gyr to $\sim$ 9 Gyr and metallicity shifts from [Fe/H] > 0.5 to $\sim$0.0. Peletier et al. (1999) has found a signature of dust in HST images in almost all S0 galaxies in their sample. On the other hand, spectroscopically derived ages and metallicities, derived from line index measurements, are largely impervious to dust (MacArthur 2005), perhaps making our comparison to Sil'chenko (2006) less satisfactory.

2.7.2 Radial Age Trends

While the inner regions of S0 galaxies have typical light-weighted ages of $\sim$3 Gyr, the outer regions are remarkably heterogeneous. For the outer regions we find a mean light-weighted age of 4.8 Gyr, with an rms scatter of $\pm$4.2 Gyr, which far exceeds observational errors. In comparison, the mean age of the inner regions is 2.6 Gyr, with an rms scatter of only $\pm$1.1 Gyr (the young ages are not affected by the upper age limit). This larger spread in outer region ages is notable in the distribution of inner and outer region ages shown in the top and bottom panels of Fig. 2.15, respectively, for all galaxies in our sample (as mentioned before, we use the H-band data for the 11 overlapping galaxies). The increased heterogeneity in outer region ages compared to the inner regions naturally creates heterogeneous radial age trends, as illustrated in Fig. 2.13. Some galaxies curl toward the left with increasing radius, crossing over

lines of constant age toward decreasing ages. Others curl to the right, thus increasing in age with radius. Age differences range from a 5 Gyr decrease to an 11 Gyr increase in age from the inner to outer regions. We find an increase in age with radius from the inner to outer radial regions for 24 galaxies, a decrease for 10 galaxies, and a change of less than 1 Gyr for 25 galaxies, i.e, 41%, 17%, and 42% of our sample of 59 galaxies respectively.

The peak ages of the inner and outer regions shown in Fig. 2.15 appear similar. However, there is a clear tail in the outer region ages toward the high age regime. (The large number of galaxies with an outer age of 13.8 Gyr is due to the limit we placed on ages). As expected, this tail is also apparent in the distribution of age *differences* from the inner to the outer region. This is demonstrated in the top panel of Fig. 2.16. Excluding this tail, many galaxies cluster around zero age difference between the inner and outer regions.

These results suggest that the outer regions of a subsample of S0 galaxies are significantly older than the remainder of our sample. For 12 out of 59 galaxies (20%) in our sample, we find a substantial increase in light-weighted age from the center of the galaxy outward, resulting in very old outer regions ($>$ 10 Gyr, SSP). We define a galaxy with a light-weighted age in the outer radial region greater than 10 Gyr as an "old outer population S0" galaxy (hereafter, OOPS). Examination of optical color images of OOPS galaxies shows no prominent features (like bars, nascent spiral structure or rings) in the outer regions of these galaxies, except for 2 galaxies: UGC 9713 (bar) and UGC 10112 (faint ring). Examples of OOPS galaxies are shown in Figs. 2.1a and 2.1g.

Our method of separating inner and outer radial regions does not set a fixed outer limit to the outer regions based on a physical quantity, such as the half-light radius, but rather uses the outer radial cutoff, which is based on surface brightness and sky error. To test for the sensitivity of our results to the outer cutoff, we have also calculated colors by defining the outer region between 1.2 and 3.5 R_e. When adjusting the outer cutoff using this definition, our result of heterogeneous outer region ages, including

the tail in distribution toward older ages in the outer region, remains unchanged and the same galaxies are defined as OOPS galaxies.

We compare our age trend results with data in other samples of S0 galaxies. Early studies on age gradients in S0 galaxies found mostly a decrease in age with radius and rarely an increase (Caldwell 1983; Bothun & Gregg 1990). However those works only analyzed the bulge and inner disk while we extend out to an average of 5 R_e, and/or they used color combinations that do not give the best separation of age and metallicity. Peletier & Balcells (1996) find a difference in age of less than 3 Gyrs between the bulge and inner disk, similar to our peak at zero age difference. While they do not observe a substantial tail toward old ages in their outer regions, their study includes early-type galaxies up to Sb, with only 8 pure S0 galaxies. Only the pure S0 galaxies (i.e. not transition) in our sample demonstrate old outer regions. Peletier & Balcells (1996) do observe two galaxies that have older ages in the outer regions; both of these are S0 galaxies. Detailed studies of individual galaxies have found both negative and positive age gradients in S0 galaxies (Norris et al. 2006; Tikhonov et al. 2003). Sil'chenko (2006) found that S0 galaxies in all types of environments contain a nuclear region that is younger than the bulge region. In this paper, we show that this trend continues outward in the galaxy for some galaxies in our sample, resulting in a large age gradient for these galaxies.

For a more quantitative comparison, we compare age gradients, Δage/Δlog(r) , in our sample with the sample of Fisher et al. (1996). For all galaxies in our sample, we derive age gradients that have a mean of Δage/Δlog(r) = 3.2 Gyr. It is likely that our mean is dominated by the OOPS galaxies comprising $\sim$ 20% of our sample. Fisher et al. (1996) found an average age gradient of Δage/Δlog(r) = 5.0 to 7.0 Gyr (depending on assumptions) for the bulge and Δage/Δlog(r) $<$ 1 Gyr for the inner disk for a sample of 9 edge-on S0 galaxies. Since we are sampling light from both components due to the face-on nature of our sample, a direct comparison is not possible. However, we do find that our age gradients are consistent with Fisher et al. (1996).

One of our most surprising results is the significantly old ages in the outer regions of 12 galaxies. Here we discuss these galaxies in more detail along with potential caveats for our deduction of old outer regions. To assist our discussion, in Fig. 2.17 we show color-color diagrams in H and J for each OOPS galaxy in our sample. Caveats for our result take two forms: observational and model dependent.

One way to test for observational effects is to examine galaxies with both J and H data available, as we have in § 2.6.2 and 2.7.1, but now with a focus on the derivation of old outer regions. When designating galaxies as OOPS galaxies, we examine outer region ages derived from both the H and J bands for galaxies. In two cases, UGC 10391 and UGC 9280, the age derived from the H band falls just outside the criteria to classify the galaxy as an OOPS and examination of color-color diagrams convinces us that these galaxies portray appropriate age trends, such as ages > 10 Gyr in at least 2 outer radial bins. Thus, the two bands agree rather well in these galaxies and they are kept in the OOPS subsample. (For consistency, we have checked color-color diagrams of our entire sample for other galaxies that may have missed the cut and found no other galaxies that we consider to exhibit the characteristic old outer region ages). One galaxy in our sample, UGC 10112, meets the criteria to be classified as an OOPS galaxy using ages extracted from both the J and H bands. The remaining nine galaxies in our sample with both J and H bands do not meet the criteria in either passband. The color-color diagrams of both the H and J bands are shown in Fig. 2.17 for the three OOPSs galaxies which have both J and H band data available (UGC 9280, UGC 10112, and UGC 10391).

Not only do OOPS galaxies have old outer regions, but they also have a significant increase in age from the center out. It is clear from Fig. 2.17 that the colors of each galaxy cross lines of constant age toward old ages from the center outward and decrease in metallicity. The observed decrease in metallicity is crutial to our understanding of these galaxies. Although the g-r color is more sensitive to age then the r-H color, the ages are highly dependent on the r-H color, due to the tilt in model colors. As well, because most of our sample has a large decrease in metallicity with radius, a

constant g-r color with radius would produce a derived increase in age with radius. Our results of both old outer regions and large increases in age for the sub-sample of galaxies hinge at the observed large decrease in r-H color. This demonstrates the importance of near-IR colors in extracting ages from photometry and our observational and model-dependent considerations must take this wavelength regime into account.

Observationally, a large concern for photometric studies of the faint outer regions of galaxies is sky subtraction. As discussed in § 2.4.4, we believe the NIR colors to be affected by sky systematics more than the optical colors. Possible causes of systematic sky error are a variation of sky value in the field, a field of view too small for the galaxy size, and a systematic error in the methodology of determining the sky background. To examine sky subtraction sensitivity to variations in the field, we estimate whether old ages would still be derived for OOPS galaxies if a sky value offset by the amount of variation was used instead. In § 2.4.4 we discussed our estimate for sky systematic uncertainties based on the standard error in the mean of the sky values from four boxes along the perimeter of the image. This error provides a large contribution to the error bars in Fig. 2.17. It is clear that the error bars in either r-H or g-r for the last few bins of all galaxies except UGC 9713 and UGC 8986 do not reach young ages. Thus, provided our measurement of systematic sky error is correct, altering the sky background by the systematic error in most OOPS galaxies would still not provide an age less than 10 Gy and the result of old outer regions would hold. A systematic error in sky from galaxies being too large for the field of view is not likely to artificially create old outer regions in OOPS galaxies because we do not find larger diameters or effective radii in these galaxies compared to the rest of our sample. Finally, an error in our methodology should have a similar effect in all galaxies in our sample, and not specifically for OOPS galaxies. Thus, we do not believe that systematic errors in the sky background alone can explain the old outer regions in OOPS galaxies.

It is also unlikely that the presence of dust has affected our results of old outer regions. While S0 galaxies likely suffer from dust effects, Peletier et al. (1999) find, based on HST images, that the light should be free from dust for most S0 galaxies at

r > 1 R_e. Examination of optical color images of OOPS galaxies shows no visible dust lanes and no nascent spiral structure in the outer regions of these galaxies. Finally, the reddening line shown in the top left of Fig. 2.17 shows the direction for dust reddening, which will tend to make both g-r and r-H redder; it does not appear that the ages in the outer region will easily shift to younger ages when reddening is corrected.

A final observational consideration is an offset in photometric zeropoint. If H-band photometric zeropoints were erroneously too large, the galaxy colors would be shifted down, creating artificially older ages (and lower metallicities) in the outer regions. This would also create lower metallicities in the central regions. OOPS galaxies do appear to have slightly lower r-H values in the central regions than other galaxies in our sample. However, we believe a lack of central dust in OOPS galaxies contributes to this effect, both from the observation that the central point is not skewed up and to the right of the second binning regions, as is observed in many galaxies with large r-H central colors, and the plausibility that these galaxies may lack a dusty center. Furthermore, many OOPS galaxies would require a significant shift either increasing in r-H or decreasing in g-r to obtain young ages, placing the central region far off the grid and far exceeding photometric errors (for reference, the mean J and H band photometric zeropoint error for OOPS galaxies is 0.11 mag).

The dependence of derived ages on r-H color also makes our result subject to modeling uncertainties, which are worse in the NIR because these fluxes are dominated by late evolutionary phases that are difficult to model (Eminian et al. 2008; Bruzual & Charlot 2003). If there are zeropoint errors in the models at subsolar metallicity, our derived ages in the outer regions will be affected. As well, the observed increase in age can be affected by metallicity-dependent model zeropoint errors. Based on the stellar population models that are currently available, our results of both old outer regions and an increase in age from the center out are not affected by our choice of model. The primary difference in the models is the treatment of the TP-AGB phase which has a strong influence at low ages/high metallicities causing large color differences in this regime, but does not affect old ages. However, colors of the outer regions of OOPS

galaxies fall off of all model grids, suggesting an inconsistency in observations and the models. While it is likely that some of the offset is due to sky subtraction error, it is unlikely, based on arguments presented above, that sky subtraction would explain the offset entirely. Thus it is possible that zero point errors in the model are at play and may affect our results. Models that predict too-large ages of galaxies has been a long-standing concern for stellar population models. Age dating of old stellar populations is influenced by uncertainties coming from the T_{eff} and [Fe/H] scale of giant branch stars (a significant fraction of the continuum light of old stellar populations, even in the blue, is provided by giant stars) as well as the luminosity function of the upper red giant branch (Schiavon et al. 2002). For example, Schiavon et al. (2002) found that the unrealistically large age derived for the globular cluster 47 Tucanae from comparison of its observed integrated spectrum to population synthesis models may be partially explained by the discrepancy between the observed luminosity function of the upper red giant branch of the cluster and the factor of two smaller number in the isochrones used in the synthesis models. Particularly related to our work is that the model prediction in Schiavon et al. (2002) for (B-V) is too blue compared to the observations, so that an older age is needed to reconcile with the observed color. Despite these concerns for the model-dependent derivation of old ages, it is unlikely that the result of old outer regions in a sub-sample of S0 galaxies will be negated with improved models.

We do not believe that our restriction to SSP models in extracting ages will have an effect on our result of old outer region ages. Because young stars dominate the light, an SSP age greater than 10 Gyr indicates the lack of any significant star formation to have occurred for quite some time. Therefore, no star formation *history* is necessary.

Given all of the above considerations, we feel that the result of old outer regions in a subsample of galaxies is robust.

2.7.3 Age Trends With Galaxy Properties

In the previous section, we established that S0 galaxies exhibit a variety of radial trends in age, with a substantial population having large increases in age. It is natural to inquire whether these age trends are correlated with global properties such as total mass, light concentration, and galaxy environment. To assess this, we first divide our sample of 59 S0s at the midpoint in stellar mass, $1x10^{11}$ $M_{\odot}$, thus forming low mass and high mass subsamples. While this midpoint is not physically motivated, it does provide adequate numbers of galaxies in both subsamples. The colors at each radial bin are averaged for all galaxies in each group, and these averaged colors are plotted in the g-r vs r-H diagram (left panel) and g-r vs r-J diagram (right panel) in Fig. 2.18. The solid, colored, error bars are the standard error in the mean for each radial bin (determined from the galaxy-to-galaxy scatter). The black dotted error bars on the first radial bin denote the standard deviation in color corresponding to the amount of scatter in color among the galaxies. The smaller error bars in the left panel, as compared to the right panel, are due to the larger number of galaxies observed in the H band than in the J band. In both the H and J-band samples there is a clear separation in ages of the two mass groups; the stellar populations of less massive galaxies are younger on average than those of more massive galaxies at all radial bins. To assess whether there is a statistically significant difference in age distribution between the high and low mass samples, we combine the ages of each radial bin for each galaxy in the designated mass sample into a single distribution. The Kolmogorov-Smirnov (K-S) two-sample test was then applied to the high and low mass combined age distributions. The hypothesis that the two samples are drawn from the same population in mean age can be rejected at the 2.7×10^{-8} level. The results of this and other K-S tests are summarized in Table 2.7. Hence the K-S test confirms what is apparent in Fig. 2.18, i.e., that the light-weighted ages of the high-mass galaxies, M>$1\times10^{11}M_{\odot}$, are significantly higher than those of the low-mass galaxies. This result is consistent with Sil'chenko (2006), who found that more massive S0 bulges are older than less massive bulges, although our result now applies to the

whole galaxy. Although the sample is not statistically complete (i.e. it's biased with respect to mass, concentration and environment to obtain a useful range in all three parameters), accounting for possible environment-age trends (as observed in Sil'chenko 2006) would only strengthen our mass-age relation.

We have also sorted galaxies into high and low concentration groups, using a separation at the median value of the concentration index, $C_{28} = 4.7$. As with the mass subsamples above, the ages at each radial bin were combined for each galaxy in the two concentration subsamples. Fig. 2.19 shows a color-color diagram for the H-band sample with the average colors of each concentration group averaged. A separation in light-weighted age at all radii is evident, such that the stellar populations of centrally concentrated galaxies ($C_{28} > 4.7$) are older than those of less centrally concentrated galaxies. The hypothesis of a similar parent distribution in age between the two subsamples can be rejected at the $2.8\text{x}10^{-6}$ level.

Because low concentration galaxies tend to be less massive than higher concentration galaxies, as seen in Fig. 2.7, the age trends found with both mass and concentration could be intertwined, with only one of the variables being the driving factor. To test which of mass or concentration is more fundamental, we further subdivide our high mass sample into low and high concentration subsamples, and do the same for the low mass sample. In Fig. 2.20, color-color diagrams are plotted with galaxies separated by mass as in Fig. 2.18, however this time only high concentration galaxies are plotted in the left panel and only low concentration galaxies are plotted in the right panel. Although Fig. 2.20 suggests that there is a larger separation in mean age for the low concentration galaxies than high concentration galaxies such that low mass galaxies of low concentration are younger on average than higher mass galaxies of low concentration, as is summarized in Table 2.7, we find a statistically significant separation in age of the two mass groups at both high and low concentration. Comparing the mean extracted ages, we find a shift in the mean age of the inner region of the two mass groups of ~ 1 Gyr for both high and low concentration galaxies. The outer region, on the other hand, shows a larger difference in mean age for the low

concentration galaxies (2.6 Gyr difference) than high concentration galaxies (1.6 Gyr difference). Fig. 2.21 reverses the analysis and shows that low mass galaxies with low concentration have younger mean ages than low mass galaxies with high concentration. High mass galaxies, however, do not form statistically separate populations in age, suggesting a weaker connection between concentration and age than mass and age. In summary, we find that galaxies with both low mass and low concentration are significantly younger in mean age than the rest of our sample. Both parameters therefore appear to drive the correlation, with mass being the dominant parameter.

To determine the correlation of age with galaxy mass and concentration at different radii and how radial trends are correlated with these parameters, in Fig. 2.22, we plot the distribution of ages for the inner regions (left panels) and outer regions (right panels) of galaxies with both low mass and low concentration (bottom panels) as well as the remaining galaxies in our sample (top panels). We find that low mass, low concentration galaxies are younger in both the inner and outer regions, as expected from Figs. 2.20 - 2.21. There is also a difference in the spread in outer region ages of the 2 groups of galaxies: low mass, low concentration galaxies do not appear to have the populated tail in the outer age distribution that is seen in the rest of the sample, but rather have an age distribution in the outer regions more similar to the inner regions. Only two galaxies, VCC 1196 and UGC 8986, with low mass and low concentration, has an outer region old enough to be considered an OOPS galaxy. A color image of VCC 1196 is shown in Fig. 2.1g. Examples of other low mass, low concentration galaxies are given in Fig. 2.1c and Fig. 2.1h.

To relax the restricted separation of mass groups by the median value, in Fig. 2.23 we show the age of the inner radial region (filled circles) and the outer region (triangles) plotted against galaxy stellar mass for all galaxies. The right panel shows the inner and outer regions for a single galaxy connected by a line, with the color designating either an increase (magenta), decrease (blue), or mostly constant (black) age with radius. The left panel shows the expected error in the age and metallicity measurements. When an error was not measurable (see § 2.6.2), the error bar is set to zero. Fig. 2.24

shows similar diagrams for concentration. OOPS galaxies are noticeable by their large outer region ages. We find that, even though OOPS galaxies are mostly absent from the low mass, low concentration regime, they cover a wide range in mass and concentration.

Fig. 2.23 & 2.24 allow an examination of whether there exists a distinct class of low-mass low-concentration S0 galaxies, or if there is rather a continuous trend with mass and/or concentration. An examination of how the age of the inner and outer region varies with galaxy stellar mass and concentration in Fig. 2.23, shows that the inner ages appear to have a trend in both mass and concentration, while the outer ages suggest two distinct groups (one being the OOPS galaxies). While this analysis is suggestive, a larger galaxy sample needs to be studied to reach any firm conclusions about the existence, or not, of a distinct class of low-mass low-concentration S0 galaxies from our data. However, as we discuss in Section 8, other investigators have also suggested that low mass S0s form a distinct class from higher mass S0s.

Our sample of S0 galaxies shows a morphological mix, with some galaxies containing more spiral features than others. We consider whether there is a difference in our results between various morphologies by examining both radial age trends and correlations with mass and concentration. The distributions of age differences for non-transition galaxies (featureless disk) and for transition galaxies are plotted in Fig. 2.16 in the middle and bottom panels respectively. There is a clear stronger positive age gradient (age increases with radius) for featureless disk S0s than for transition galaxies. Except for one galaxy, UGC 10163, transition galaxies do not appear to have the same tail into large age differences as other galaxies. Even for this galaxy, the light-weighted age of the outer region is still fairly young and not old enough to be classified as an OOPS galaxy. A color image of UGC 10163 is shown in Fig. 2.1f. The transition galaxies also have a slightly younger mean age than featureless disks. This is expected if transition galaxies have a growing spiral structure where young stellar populations are located. A K-S test to the age differences of the two groups reveals a statistically separate populations greater than the 2 σ confidence level. We

see that both transition galaxies and low mass, low concentration galaxies lack the tail of galaxies with old outer regions. However, the transition galaxies have a range of mass and concentration so they are not the same group of galaxies as the low mass, low concentration galaxies, nor are they mutually exclusive from them.

The environment of a galaxy clearly can play an important role in its evolution, given the greater fraction of local S0s in high density environments. If we divide our sample into high and low density subsamples at the median local log density value of -0.67, there is however little evidence for any age difference between high and low density S0s. If we increase the dividing line to a local log density value of -0.3, we see a slightly larger correlation. In this case, we find 12 galaxies in the high density group and 28 in the low density group (for the 40 H-band sample galaxies). Fig. 2.25 shows that galaxies in high environmental densities (blue, d > -0.3) generally have younger ages than those in low density environments (red, d < -0.3). However, only when ages from all radial bins are combined is there a statistical separation at the $\sim 2\sigma$ confidence level in age between the high and low density environments, suggesting a weaker correlation with age than was found for mass and concentration. On the other hand, if we separate high and low density groups by an even larger density than -0.3, e.g., +0.2, a more statistically significant separation in ages for all radial bins combined is evident (see Table 2.7). A relation of increasing age for higher density environments, the opposite of the trend found here, for early type galaxies is outlined in the literature (Kuntschner et al. 2002; Thomas et al. 2005; Sil'chenko 2006) and predicted in the current hierarchical assembly paradigm (De Lucia et al. 2006). Some studies, though, have showed minimal influence from the environment on ages of S0 galaxies (Peletier et al. 1999; Kochanek et al. 2000). In addition to our sample containing insufficient S0s in the high density environment (we have no S0s in rich clusters other than the small sample of Virgo galaxies), our sample also contains a bias in mass and environment. Thus, we may be observing a relation in mass, creating the appearance that higher density environments contain more galaxies with younger light-weighted ages. The combination of a statistically incomplete sample (e.g., all of the observed lowest mass

galaxies are in the Virgo cluster high density environment) and a scarcity of high density environment makes it difficult to draw conclusions regarding environment and age. Regarding OOPS galaxies, we find that they appear at a range of environmental densities, based on our possibly limited range in environment.

Table 2.7: Results from Statistical Analysis[1]

Groups	Result
inner region ages from J-band and H-band for galaxies in common	0.99
outer region ages from J-band and H-band for galaxies in common	0.81
inner ages of high and low concentration galaxies[2]	2.0E-3
outer ages of high and low concentration galaxies[2]	0.10
inner ages of high and low mass galaxies [3]	4.9E-6
outer ages of high and low mass galaxies [3]	0.03
inner ages of high and low density galaxies [4]	0.22
outer ages of high and low density galaxies [4]	0.87
inner ages of high and low density galaxies [5]	0.06
outer ages of high and low density galaxies [5]	0.20
ages for all bins of high and low concentration galaxies [2]	2.82E-6
ages for all bins of high and low mass galaxies[3]	2.67E-08
ages for all bins of high and low density galaxies [4]	0.09
ages for all bins of high and low density galaxies [5]	1.7E-3
outer metallicity of high and low concentration galaxies[2]	0.48
outer metallicity of high and low mass galaxies [3]	0.09
outer metallicity of high and low density galaxies [4]	0.52
ages for all bins of high and low mass galaxies with low concentration [23]	1.1E-3
ages for all bins of high and low mass galaxies with high concentration [23]	1.4E-3
ages for all bins of high and low concentration galaxies with low mass [23]	6.0E-3
ages for all bins of high and low concentration galaxies with high mass [23]	0.07
age differences of transition and featureless disk galaxies	0.02

Table 2.7: Results from Statistical Analysis[1]

Groups	Result
metallicity gradient ($\Delta[M/H]/\Delta log(r)$) of high and low mass galaxies [3]	0.72
metallicity gradient ($\Delta[M/H]/\Delta log(r)$) of high and low concentration galaxies [2]	0.41
metallicity gradient ($\Delta[M/H]/\Delta log(r)$) of high and low density galaxies [4]	0.22

2.7.4 Metallicity Trends

Radial trends in mean metallicity, as well as in metal abundance ratios, provide information on galaxy evolution complementary to that extracted from trends in age. Negative metallicity gradients have been previously found for S0 galaxies (Fisher et al. 1996; Tamura & Ohta 2003; Rickes et al. 2009). From their spectroscopic sample Fisher et al. (1996) found a mean of Δ[Fe/H]/Δlog(r) = -0.9 to -0.7 (depending on assumptions) for their bulges and Δ[Fe/H]/$\Delta(r_{kpc})$ = -0.04 to -0.06 kpc^{-1} (depending on assumptions) for the disks. We carry these observations to larger radii and examine the correlations with global properties. Since from color data alone it is not possible to extract information about non-solar element abundance ratios, in what follows we examine the trends in mean metallicity in S0 galaxies, based on the scaled solar modeling described in §6.

It is evident from Fig. 2.13 that virtually all S0s have significant negative metallicity

[1]Probability from Kolmogorov-Smirnov test that the two groups are drawn from the same population.

[2]separation of concentration is $C_{28} = 4.7$.

[3]separation of mass is 1E11.

[4]separation of density is -0.3.

[5]separation of density is +0.2.

gradients. We find a mean and median metallicity gradient, $\Delta[Z/H]/\Delta log(r)$, of -0.5 and -0.3, respectively. In terms of physical radius, the gradients have a mean and median $\Delta[Z/H]/\Delta(r_{kpc})$ of -0.09 and -0.04, respectively. Although a direct comparison with Fisher et al. (1996) is not possible because of the different populations studied, we do find comparable metallicity gradients. A possible source of bias in the metallicity gradients that we observe is dust in the central regions of the galaxy, causing the metallicities in the central regions to be biased high, hence biasing the gradients towards larger negative values. On the other hand, the fact that we place an upper limit on mean metallicity of $[Z/H] = +0.5$ tends to suppress the highest metallicities in the central regions, and thus lower the absolute size of the negative gradients. We have avoided the central most binning region in calculation of gradients to lessen these effects.

The correlation of metallicity with mass, concentration, and environment can be assessed in the same way as for age, i.e., by dividing the sample into high and low mass, concentration, and environment subsamples. However, due to the fact that the inner regions of many galaxies lie off the model grid and are thus set to the maximum metallicity of 0.5 dex, we are not able to assess a correlation of metallicity with mass, concentration, and environment in a quantitative way for the inner regions of the galaxies. We can, however, examine the metallicity of the outer regions. Results of our K-S two-sample tests to the various subsamples, summarized in Table 2.7, suggest that when mean metalliciities for the outer radial regions are considered, neither mass, concentration, nor environment indicate a statistically different population at the 2 σ level. The metallicity gradients, as well, are not significantly correlated with global parameters; within errors, we find not difference in mean or median metallicity gradients for high and low mass, concentration, and density groups. Studies detailing mass-metallicity relations in S0 galaxies are abundant (Garnett 2002; Tremonti et al. 2004; Kauffmann et al. 2003), but most of these studies are of a central metallicity or a global metallcity (such as studies at high z where the aperture contains the entire galaxy) so that a mass-metallicity relation in the outer parts of S0 galaxies is not

clear. While our results suggest no outer metallicity-mass relation, a bias in our sample with mass and environment (e.g., all of the observed lowest mass galaxies are in the Virgo cluster high density environment) may be at play. Along with mass-metallicity relations in the literature, trends of lower metallicity for lower environmental density have also been observed (Cooper et al. 2008). The mass/environment bias in our sample, which is the reverse of what has been observed in nature (Hogg et al. 2003; Kannappan et al. 2009b), is in the direction to hide a mass-metallicity and an environment-metallicity relation in our sample.

2.8 Discussion

We have examined in the present paper the connection between the globally averaged light-weighted ages of S0 galaxies and other global properties, such as stellar mass, concentration, and environment. We have also investigated the radial age and metallicity trends in S0s. We find that at all radii, galaxies with lower mass and lower concentration have younger ages on average than other galaxies. We have also found that virtually all S0 galaxies have negative metallicity gradients, with an average value of Δ[Z/H]/Δlog(r) = -0.5. On the other hand, the radial behavior of age in S0s is heterogeneous; both positive and negative age gradients are found. We observe an increase in age with radius for 41% of our sample, a decrease for 17%, and little change for 42%. For 20% of our sample, there are populations with substantially old light-weighted ages ($>$ 10 Gyr) in the outer region of the galaxy. We now consider the implications of these results.

2.8.1 Low Mass, Low Concentration Galaxies

A principal result of our study is that low mass, low concentration S0 galaxies have younger ages at all radii than S0s with high mass and/or concentration. It is not surprising that the concentration and mass parameters are connected to the formation history of S0 galaxies in this manner, since recent studies (Koo et al. 2005) have found

that massive bulges in spirals formed their stars earlier, at high gas density. Both higher concentration and higher stellar mass point towards higher bulge mass at early epochs.

Low mass, low concentration spiral galaxies (i.e. later types) have been found to be on average younger than earlier type spirals (MacArthur et al. 2004). Hence it seems likely that we would see this same trend in S0 galaxies, especially if S0s have been transformed from a spiral galaxy. Age trends with mass in the central regions of galaxies are predicted in bulge formation scenarios of both a merger origin and a secular evolution origin. Although the observed trends with bulge age and mass of S0 and spiral galaxies first appeared to be at odds with hierarchical galaxy formation models, recent semi-analytic modeling, containing enhanced feedback processes such as AGN, produce more extended SFHs in less massive galaxies, leading to positive correlations of mass with average age. (Cole et al. 1994; Bower et al. 2006; De Lucia et al. 2006; Croton et al. 2006). In particular, Cole et al. (1994) found that massive spheroids tend to form from fragments that formed their stars early and their star formation is quenched when they lose their hot gas reservoir by preferentially falling into deeper potential wells. It has also been shown that positive correlations of mass with average age can be a natural consequence of hierarchical merging (Neistein et al. 2006). Alternatively, recent studies of late type spiral galaxies suggest the importance of secular evolution in bulge formation (Ellis et al. 2001; Combes 2000; Kormendy & Kennicutt 2004; MacArthur et al. 2009). For example, surface photometry of late type spirals (Kormendy 1993; Courteau et al. 1996; Carollo 1999) reveals that their 'bulges' are best fit by a disk-like exponential light profile. The observed structural similarity between the disk and the inner 'bulge' is predicted by secular evolution models (Pfenniger & Norman 1990). A small bulge, whether in a late-type spiral galaxy or a low mass, low concentration S0 galaxy, is more likely to contain associated star formation from secular evolution, even if some of the mass has been built up previously (Ellis et al. 2001). Indeed, MacArthur et al. (2009) found by spectroscopic analysis of stellar populations that $\sim$20% of the mass of the mass of late type spiral

bulges consists of stars less than 1Gyr (in fact, 70% of the bulge *light* comes from these young stars.) Detailed spectroscopic studies of S0 galaxies will determine if this is also true of low mass, low concentration S0s. Although a secular origin for the bulge for low mass, low concentration S0 galaxies is an attractive possibility and could explain the difference in central ages between these galaxies and others in our sample, we observe younger ages in low mass, low concentration galaxies at all radii. If the outer regions are dominated by a disk component, then this suggests that the disks of these galaxies are also younger than other galaxies in our sample. If true, galaxy formation models will need to take this additional constraint into account.

Other investigations have found a trend of mean S0 galaxy age with *dynamical* mass similar to what we have found with stellar mass and concentration (Mehlert et al. 2003; Sil'chenko 2006; Bedregal et al. 2008). For example, Bedregal et al. (2008) has studied the central regions of S0 galaxies using both velocity dispersion and rotational velocity for dynamical mass estimates. Through analysis of [α/Fe], their results indicate that for central regions at least, different star formation histories are responsible for the difference in mean ages. They suggest that their results are consistent with a scenario where faint S0s are descendants of spiral galaxies which lost or exhausted their gas, while bright systems have star formation histories that resemble those of normal ellipticals. Can this scenario be extended to our results to include the concentration of a galaxy? Physically speaking, S0 galaxies with low mass and low concentration are certainly more similar to the more disk-dominated spiral galaxies, while high mass and high concentration S0s would have a more dominant elliptical like component. However, a high mass, low concentration galaxy, which is shown in our results to separate in age from low mass, low concentration galaxies, is difficult to reconcile with an elliptical like origin. Future results on whether there exists a distinct class of low-mass low-concentration S0 galaxies, rather than a continuous trend with mass and/or concentration will help disentangle possible formation scenarios. Due to the complexity of S0 formation/transformation mechanisms, studies of a larger sample of S0 galaxies, especially low mass, low concentration galaxies, are needed to

fully understand the formation of these galaxies.

2.8.2 OOPS Galaxies

Another significant result that we have found is a subsample of galaxies with significantly old ages in their outer regions and large increases in age from the center outward. These OOPS galaxies appear to form a separate class, in terms of their star formation histories, from the rest of the sample. To understand the implications of OOPS galaxies on galaxy evolution, we need to establish whether the outer region of these galaxies is dominated by a disk or bulge component. The importance of this is striking; if we are observing old stars in the outer region of the disk, then either these galaxies have not undergone a major, disk-destroying merger for a very long time or the old stars are somehow redistributed into the outer parts of the disk. Interestingly, Koo et al. (2005) find a few very red luminous disks at high redshift, implying that at z=1 not all massive disks are young and some old, massive S0s have already existed in the field. Also, some models of disk formation have predicted an increase in age with radius (Roškar et al. 2008) and several theories of Spiral-to-S0 transformation through external gas removal processes predict a resultant trend of increasing age with radius (Quilis et al. 2000; Kawata & Mulchaey 2008; Kronberger et al. 2008). In any case, determining the structural component (i.e. disk versus spheroidal) that makes up the outer region is a necessary step to understand the formation history of these galaxies. In a § 3 we will present our results and analysis from galactic component decompositions of our sample.

2.9 Conclusion

We present optical (SDSS g and r) and near-IR (H and/or J) surface photometry for a sample of 59 S0 galaxies covering a range in stellar mass, light concentration, and environmental density. Radial age and metallicity gradients out to at least 5 effective radii are derived from comparison of the observed g-r and r-H (and/or r-J) colors to

stellar population models.

We find an average central light-weighted age ∼3 Gyr and central metallicity of [Z/H]∼0.5 dex. For most of the galaxies in our sample we find large negative metallicity gradients with an average of Δ[Z/H]/Δlog(r) = -0.5. Radial age trends are more heterogeneous. An increase in age with radius is found for 41% of our sample, a decrease for 17%, and little change for 42%. In virtually all of the galaxy sample a negative metallicity gradient is found with radius.

The outer regions of 20% of our sample have very old light-weighted ages (> 10 Gyr) and also exhibit large increases in light-weighted age from the center outward. These OOPS galaxies are found in a range of environments, masses, and concentrations, but are rarely found in galaxies with both low mass and low concentration. None of these galaxies is found to contain nascent spiral structure. Determining the structural component (i.e. disk versus spheroidal) that makes up the outer region is a necessary step to further probe the formation history of these galaxies. Bulge and disk decompositions for the OOPS galaxies are discussed in § 3.

We find that mean age correlates with both mass and concentration; for all radii, galaxies with both lower mass and lower concentration have, on average, younger ages than other galaxies in our sample. Studies of a larger sample of S0 galaxies, particularly those with low mass and low concentration, will enable a decisive test of whether low mass low concentration S0s constitute a fundamentally separate class of S0 formation, or whether they are simply extreme examples of a basic correlation between mass/concentration and star formation history in a more unified evolutionary picture for S0 galaxies.

We wish to thank S. Charlot and G. Bruzual for providing their new models, J. Miner for providing density calculations, and J. Roediger and S. Kannappan for stimulating discussions. This study was partially funded by NSF grant AST 04-06443 to the University of North Carolina. L.C. acknowledges the support of the Linda Dykstra Science Dissertation Fellowship and S.C. acknowledges the support of NSERC through Discovery grant. This research has made use of the NASA/IPAC

Extragalactic Database (NED) which is operated by the Jet Propulsion Laboratory, California Institute of Technology, under contract with the National Aeronautics and Space Administration.

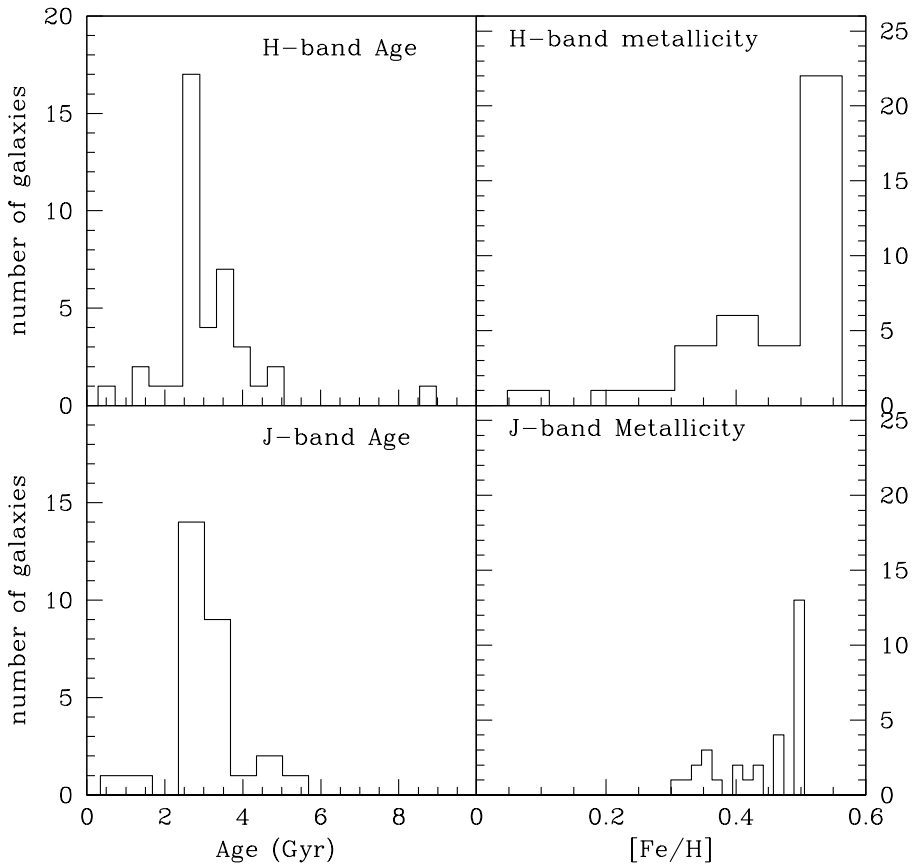

Figure 2.14 Distribution of average age (in Gyr) of the central 0.5 R_e for galaxies in the H-band sample, top, and J-band sample, bottom. Right: Distribution of average metallicity (in [Z/H]) of the central 0.5 R_e for galaxies in the H-band sample, top, and J-band sample, bottom.

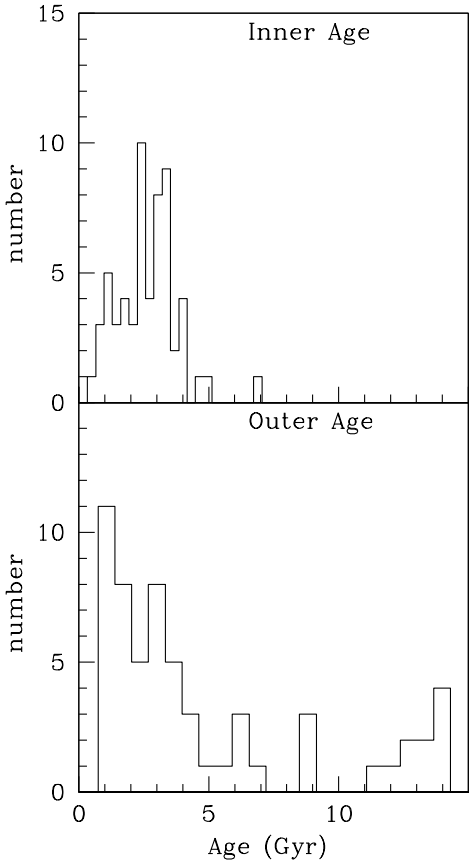

Figure 2.15 Top and bottom panels show the distribution of average ages (in Gyr) of the inner ($r < 0.8\ R_e$) and outer ($r > 1.2\ R_e$) regions, respectively, for all galaxies in our sample.

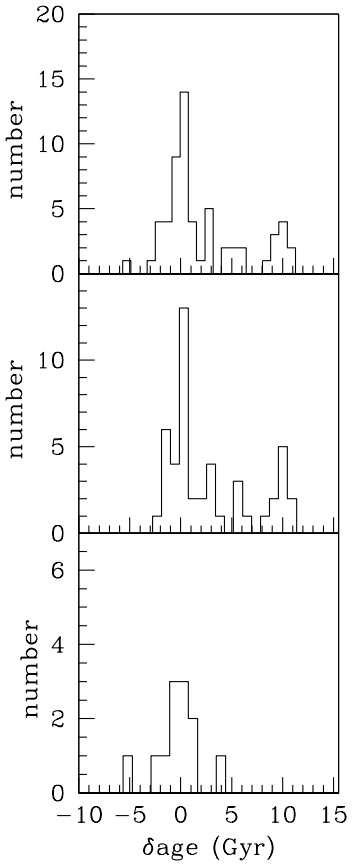

Figure 2.16 Top: Distribution of light-weighted age differences (in Gyr) from the inner to outer regions (outer age - inner age) for all galaxies in our sample. Middle: Distribution of age differences for featureless disk galaxies. Bottom: Distribution of age differences for transition galaxies.

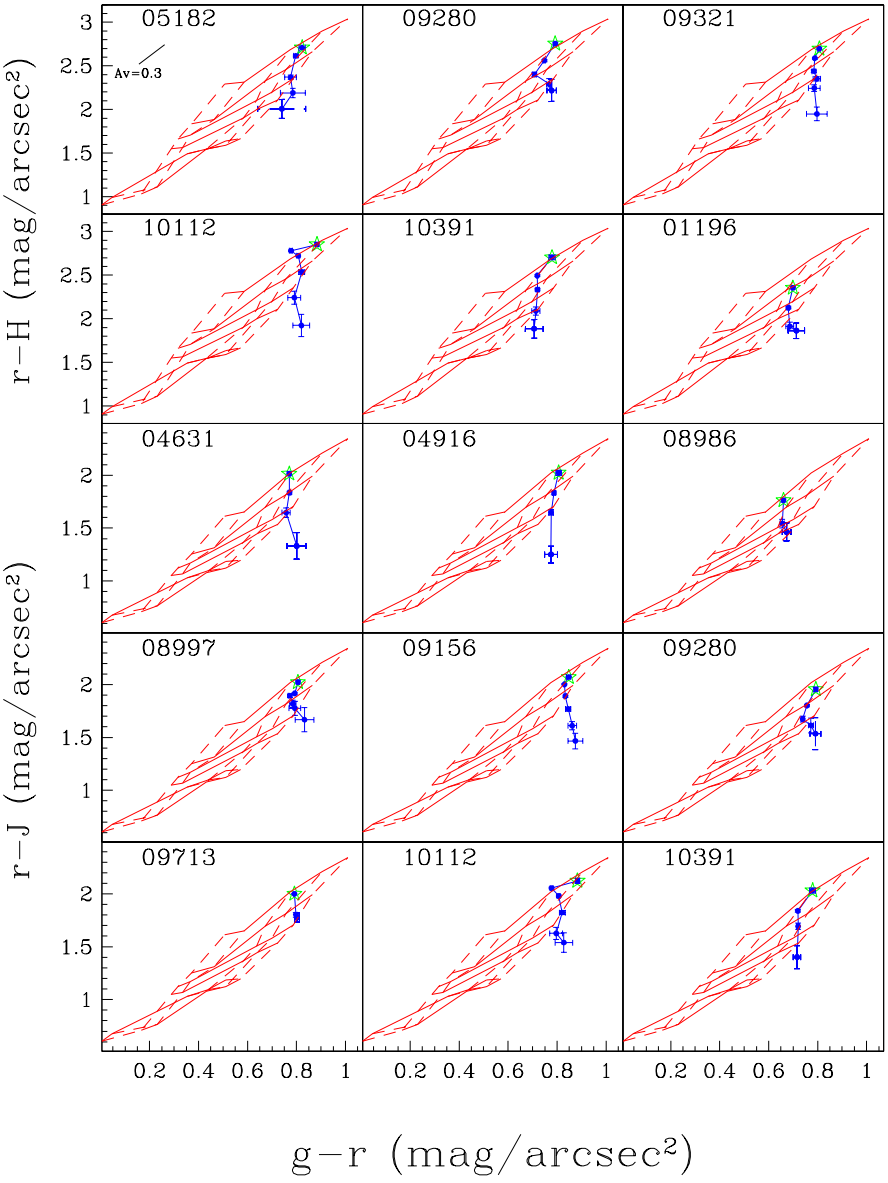

Figure 2.17 Color-color diagrams for the sample of OOPS galaxies in the H-band (top two rows) and J-band (bottom 3 rows) plot individually in a panel. The model grid and errors are the same as in Fig. 2.9.

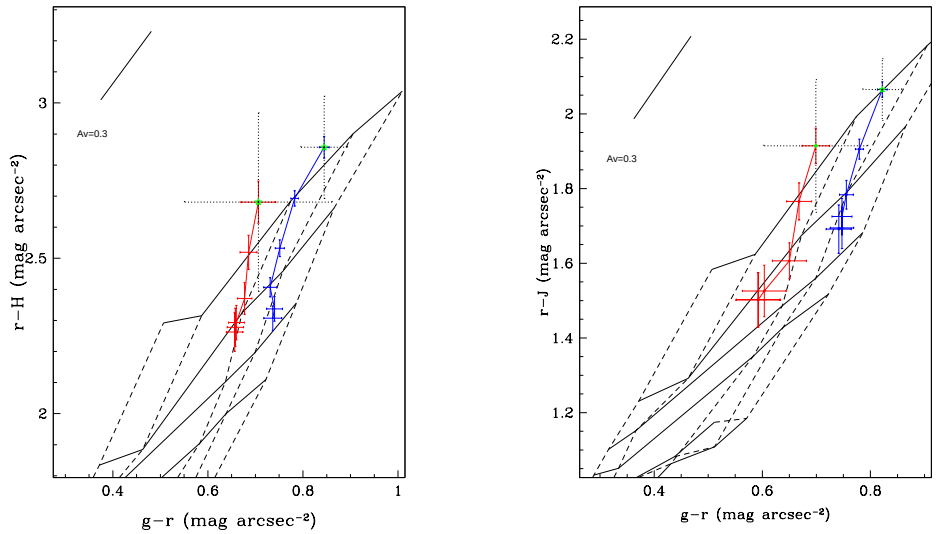

Figure 2.18 Plot is a g-r vs r-H color-color diagram (left) and g-r vs r-J (right) for the high and low stellar mass groups. In the right panel, the same model grid is used as in Fig. 2.9, but using r-J. The red and blue solid lines represent the average colors for galaxies with mass $< 1x10^{11}$ $M_{\odot}$ and mass $> 1x10^{11}$ $M_{\odot}$, respectively. The solid colored error bars on each radial bin represent $\pm$ 1 sigma, where sigma is the standard error in the mean based on the scatter in color for each radial bin in the designated mass range. The black dotted error bar on the first radial bin represents the standard deviation. The reddening line, ages and metallicities, and symbols are the same as in Fig. 2.9.

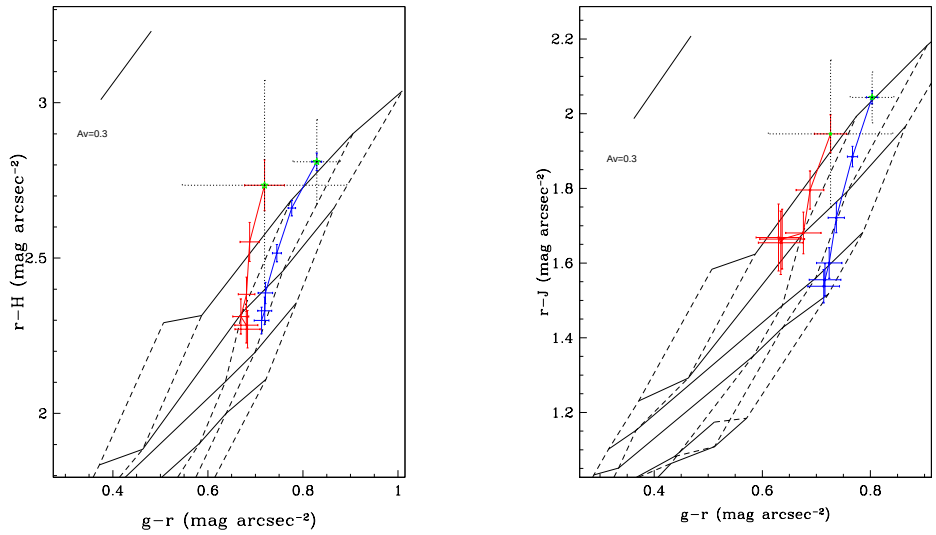

Figure 2.19 Color-color diagram for galaxies separated by high and low light concentration. The solid red and blue lines represent the average colors for galaxies with $C_{28} < 4.7$ and $C_{28} > 4.7$, respectively. The model grid is the same as in Fig. 2.9. The solid colored error bars on each radial bin represent $\pm$ 1 sigma, where sigma is the standard error in the mean based on the scatter in color for each radial bin in the designated concentration range. The black dotted error bar on the first radial bin represents the standard deviation. The left panel shows r-H vs g-r for the H-band sample and the right panel shows r-J vs g-r for the J-band sample.

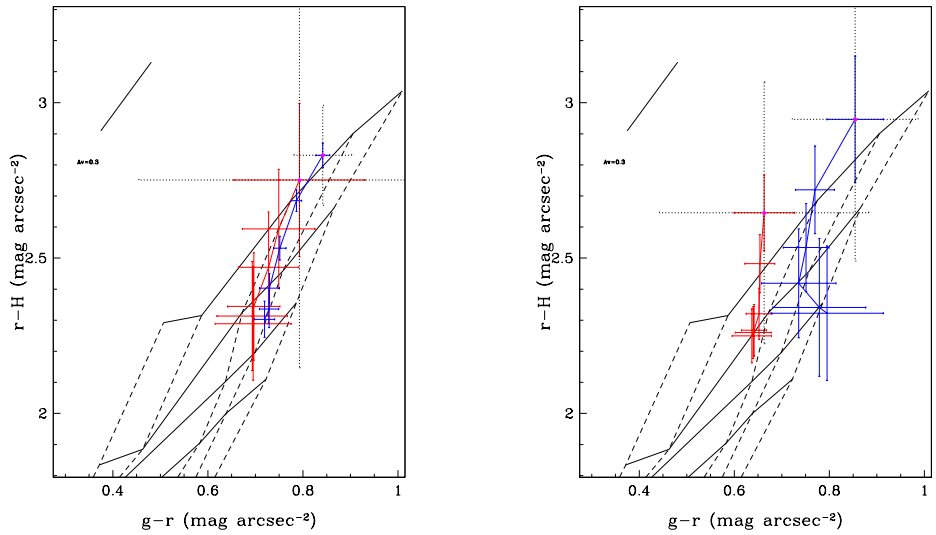

Figure 2.20 Color-color plots for high (left) and low(right) light concentration galaxies, separated by $C_{28} = 4.7$ are shown for the H-band sample. The solid red and blue line represents the average colors for galaxies with mass $< 1 \times 10^{11}$ $M_{\odot}$ and mass $> 1 \times 10^{11}$ $M_{\odot}$, respectively. The solid colored error bars on each radial bin represent $\pm$ 1 sigma, where sigma is the standard error in the mean based on the scatter in color for each radial bin in the designated mass range. The black dotted error bar on the first radial bin represents the standard deviation. The model grid, reddening line, and symbols are the same as in Fig. 2.9.

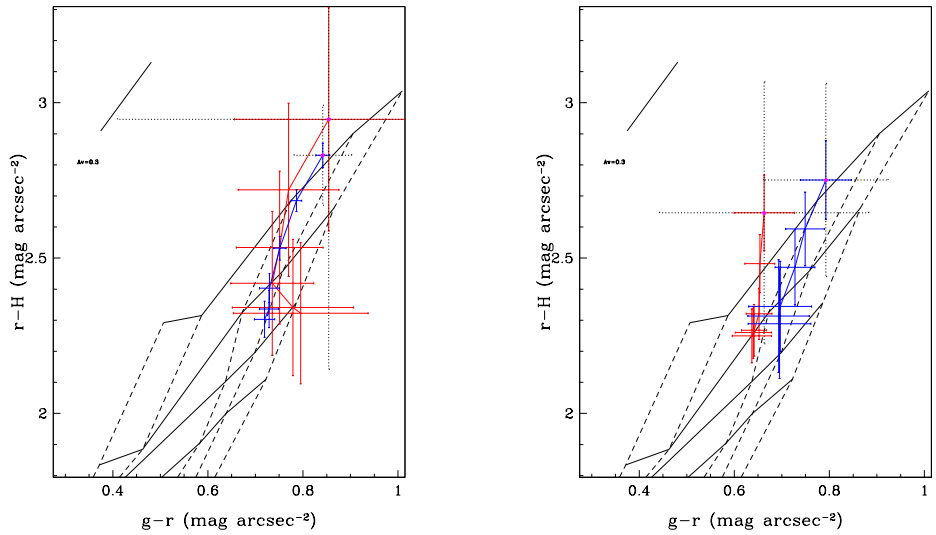

Figure 2.21 Color-color plots for high (left) and low(right) mass galaxies, separated by a mass of 1×10^{11} $M_{\odot}$, are shown for the H-band sample. The solid red and blue line represents the average colors for galaxies with mass $C_{28} < 4.7$ and $C_{28} > 4.7$, respectively. The solid colored error bars on each radial bin represent $\pm$ 1 sigma, where sigma is the standard error in the mean based on the scatter in color for each radial bin in the designated concentration range. The black dotted error bar on the first radial bin represents the standard deviation. The model grid, reddening line, and symbols are the same as in Fig. 2.9.

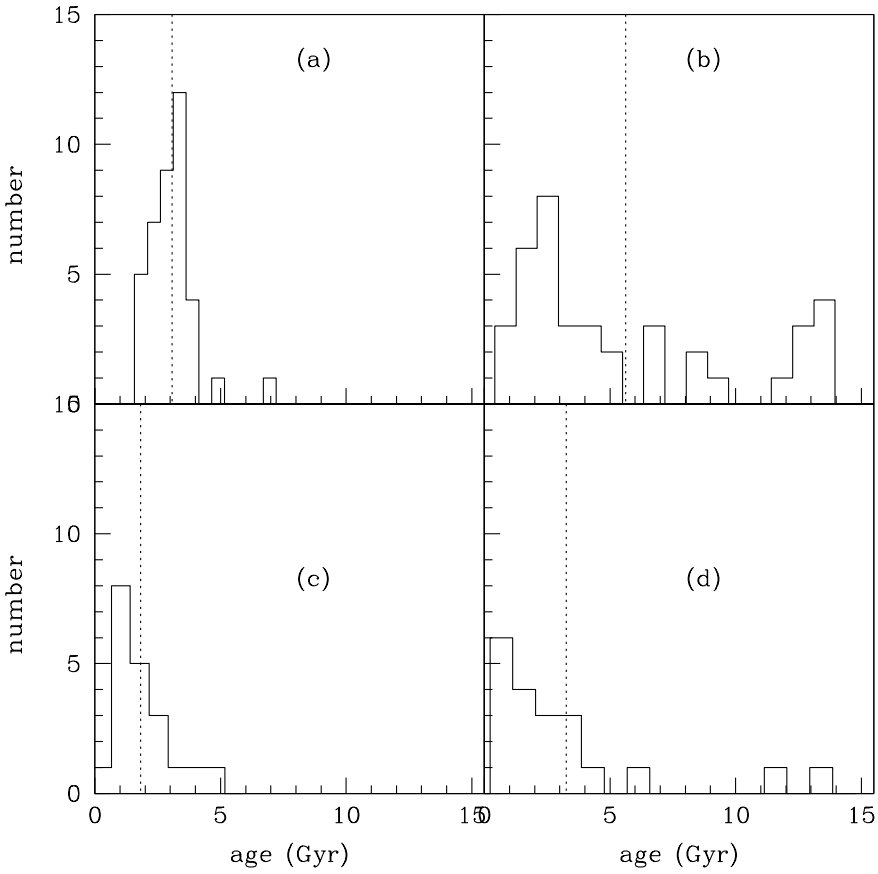

Figure 2.22 The distribution of inner ages (R $< 0.8\ R_e$) for high mass or high concentration galaxies (mass $> 1 \times 10^{11}\ M_\odot$ or $C_{28} > 4.7$) is shown in panel (a), and galaxies with both low mass and low concentration (mass $< 1 \times 10^{11}\ M_\odot$ and $C_{28} < 4.7$) in panel (c). The distribution of outer ages (r $> 1.2\ R_e$) for high mass or high concentration galaxies is shown in panel (b) and for galaxies with both low mass and low concentration panel (d). In all panels, the mean age is indicated by a dotted vertical line.

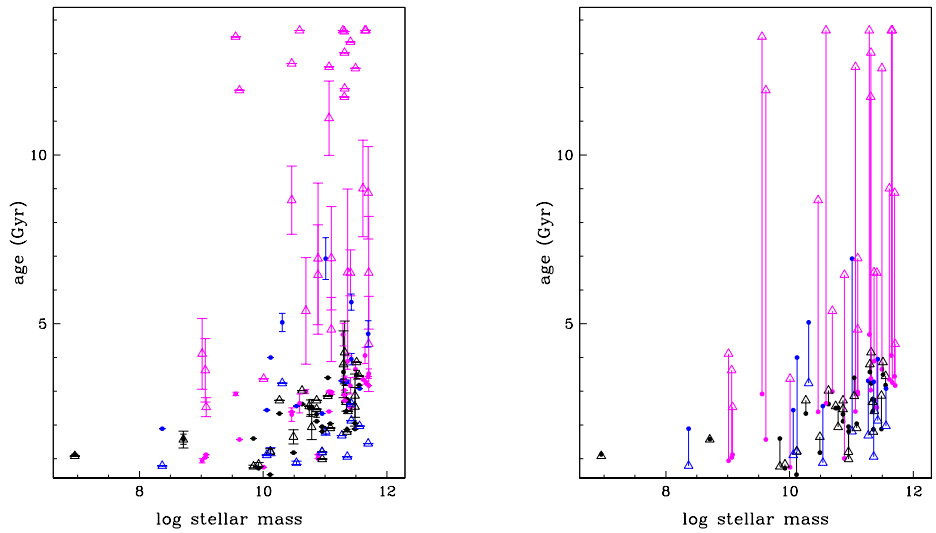

Figure 2.23 Light-weighted mean age (Gyr) versus galaxy stellar mass (log solar mass) for inner (filled circle) and outer (triangle) radial regions. The left panel shows error in age measurements while the right panel leaves them out for visual ease. Lines connect the inner and outer radial regions for a single galaxy. The colors represent the trend in age with radius outward. Magenta denotes an age increase, δage $>$ 2.0 Gyr, blue denotes a decrease, δage <- 2.0 Gyr, and black represents galaxies with a small or no change in age, -2.0 Gyr $<$ δage $<$ 2.0 Gyr

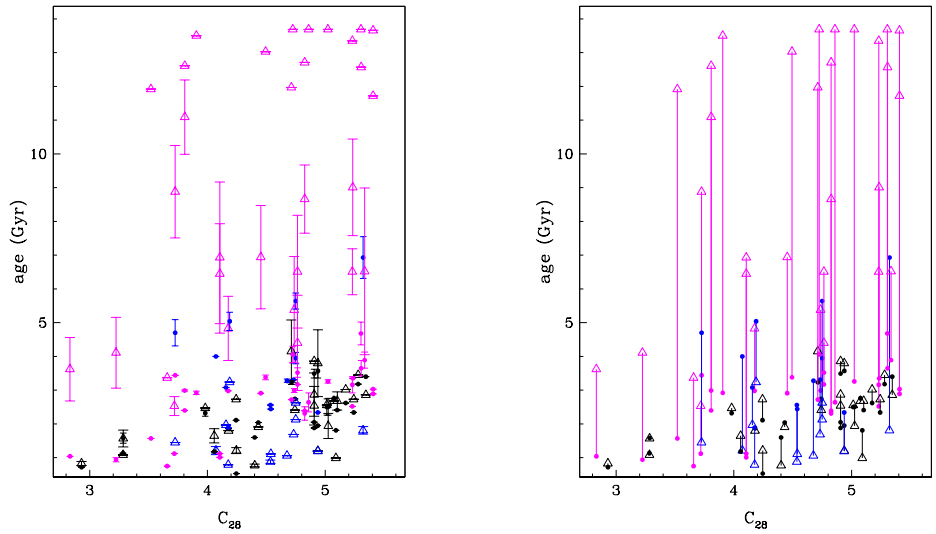

Figure 2.24 Light-weighted mean age versus light concentration is plot for the entire sample. Inner radial regions are shown as filled circles and outer radial regions are triangles. The left panel shows error in age measurements while the right panel leaves them out. Lines connect the inner and outer radial regions for a single galaxy. The colors are as in Fig. 2.23

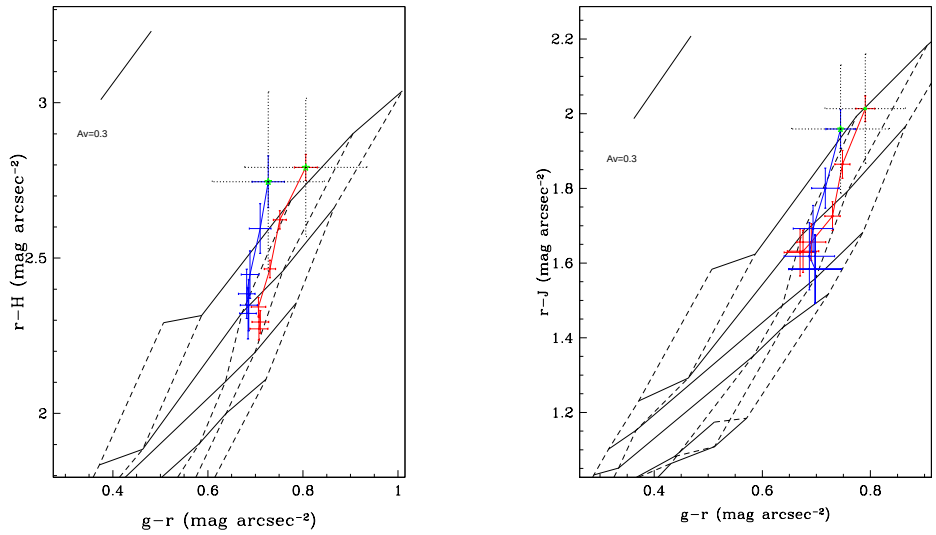

Figure 2.25 Color-color diagram for the high and low environmental density bins. The solid red and blue lines represents the average colors for galaxies with d < -0.3 Log $Mpc^{-3}$and d > -0.3 Log Mpc^{-3}, respectively. The model grid is the same as in Fig. 2.9. The solid colored error bars on each radial bin represent ± 1 sigma, where sigma is the standard error in the mean based on the scatter in color for each radial bin in the designated density range. The black dotted error bar on the first radial bin represents the standard deviation. The left panel shows r-H vs g-r for the H-band sample and the right panel shows r-J vs g-r for the J-band sample.

Chapter 3

Bulge/Disk Decompositions of S0 Galaxies with Old Outer Regions

L. C. Prochaska Chamberlain

Department of Physics and Astronomy, CB 3255, University of North Carolina, Chapel Hill, NC 27599

chaska@physics.unc.edu

Stéphane Courteau

Department of Physics, Engineering Physics and Astronomy, Queens University, Kingston, ON, Canada

courteau@astro.queensu.ca

Mike McDonald

University of Maryland, College Park, MD

mcdonald@astro.umd.edu

James A. Rose

Department of Physics and Astronomy, CB 3255, University of North Carolina, Chapel Hill, NC 27599

jim@physics.unc.edu

ABSTRACT

We have performed galactic component decompositions for a sample of 22 S0 galaxies using a generalized Sersic component for the bulge and an exponential profile for the disk. Our main goal is to understand the nature of S0 galaxies that have a substantially old outer regions (> 10 Gyr). Our database consists of deep H and/or J images of nearby S0 galaxies that demonstrate this radial trend and we have included additional S0 galaxies for comparison. We find that nearly all galaxies in our sample contain outer regions that are disk dominated. Most importantly, our results indicate that the disk component is responsible for the old ages in galaxies having large radial increases in age. The ages of the disks of these galaxies place a constraint on models of hierarchical merging, requiring no major merger to have occurred for these galaxies in a very long time (since z $\sim$ 2, using an age of 10 Gyr). For all galaxies in our sample, we derive a mean n of 2.0 $\pm$ 0.6, a mean ratio of bulge and disk scale lengths, r_e/h, of 0.41 $\pm$ 0.40, and a mean $(B/D)_{tot}$ of 1.8 $\pm$ 3.1. We find a correlation between n and $(B/D)_{tot}$ such that galaxies with larger n are more bulge dominated.

3.1 Introduction

S0 galaxies offer a unique opportunity to study disk formation from both an observational and an evolutionary perspective. The average light from their disk is significantly less overwhelmed by the knots of young star formation and dust compared to spiral galaxies. Additionally, the relatively smooth light distributions of a large fraction of S0 galaxies enable robust surface brightness decompositions of their photometric components. From the perspective of galaxy evolution, S0 galaxies lie in a special morphological position between gas rich spirals and gas poor ellipticals. Whether S0 galaxies are thought to have a formation more tied to an elliptical or a spiral galaxy directly affects our view of the origin of the Hubble sequence. As well, their minority existence in low density environments presents a puzzle to formation models of this class of galaxies. Thus, analysis of the stellar populations and structural

parameters of featureless S0 galaxies provide a crucial component to disk formation studies.

Both primary galaxy formation mechanisms (i.e. hierarchical merging or monolithic collapse) and secondary formation mechanisms (i.e. secular bulge formation or gas removal from the disk) produce imprints on the galaxies' star formation history. Therefore, observations of radial stellar population (SP) gradients help to distinguish between possible scenarios for S0 galaxy formation. Radial stellar population trends out to at least 5 effective radii were studied for a sample of 59 S0 galaxies in detail in § 2. There, we found that virtually all S0 galaxies have negative metallicity gradients while both positive and negative age gradients were found. Of particular interest are galaxies that were found to have substantially old outer regions (>10 Gyr). These old outer population S0 galaxies (OOPS) appear to form a separate class, in terms of their star formation histories, from the rest of the sample. They are found in a range of environments, masses, and light concentrations, but are appear to be rarer in galaxies with both low mass and low concentration. None of these galaxies is found to contain nascent spiral structure and many are entirely featureless in ground based images.

The nature of the old SP's of OOPS galaxies can set constraints on galaxy formation theories. For example, if the old SPs are reflecting the age of the disk component, then either these galaxies have not undergone a major, disk-destroying merger for a very long time or the old stars are somehow redistributed into the outer parts of the disk. Whether the increase in light-weighted age with radius is due to an age gradient in the disk component will also offer clues to the specific formation of S0 galaxies by testing predictions of primary and secondary formation scenarios, such as the inside-out formation of the disk predicted in hierarchical models (Fall & Efstathiou 1980).

To understand the implications of OOPS galaxies on galaxy evolution, however, we first need to establish which physical component is dominating the light at different radii along the galaxy. The light distribution in S0 and other disk galaxies is often separated into a bulge and disk component, which are assumed to be physically and

dynamically distinct. Although disk galaxies are thought to be dominated by the disk in the outer regions, some S0 galaxies are found to have disks embedded in a large spherical halo (Erwin et al. 2005). Separating both components using only the surface photometry of a galaxy is not trivial and many different decomposition techniques can be found in the literature. For most methods, one postulates mathematical functions describing the shape of the different components and fits these components to the observed light distribution. Decomposition techniques differ in both the assumed mathematical functions as well as in the applied fitting algorithms. Most frequently the disk is fit with an exponential function (Freeman 1970) and the bulge with either a general Sersic law (Sersic 1968), or a more special case of $r^{1/4}$ law (de Vaucouleurs 1948). A number of studies suggest a range of bulge shapes from early to late type spirals (de Jong 1996a; Courteau et al. 1996; Carollo 1999; Graham 2001), indicating that a general Sersic law is a good match for the bulge component.

In this paper, we present our results and analysis from galactic component decompositions of a sample of 22 S0 galaxies. This study focuses on the development of a reliable set of surface brightness profile decompositions based on a sub-sample of galaxies from § 2. An important goal is to understand whether the old outer regions of OOPS galaxies are disk or bulge dominated. Our sample for this paper was thus chosen to focus on OOPS galaxies. We include additional galaxies from § 2 for comparison. The surface-brightness profiles are modeled to determine the galaxy's bulge and disk structural parameters using a two-component fit consisting of a Sersic bulge and an exponential disk.

3.2 Data

3.2.1 Sample Selection

The main goal of this paper is to address the nature of the OOPS galaxies described in § 2. In order to determine the galactic component decomposition for these galaxies,

a sample of S0 galaxies were selected from § 2 to include OOPS galaxies. The sample from § 2 includes galaxies from the UGC catalog (Nilson 1973) with S0, S0a and S0B morphological classes and blue Galactic extinction ≤ 0.5, and was chosen to cover a representative range of mass and light concentrations.

In galactic component decompositions, complications arise when the smooth exponential disk assumption is invalidated by the presence of inner and outer disk truncations, bars, spiral arms, or other structure. Fortunately, 9 out of 12 OOPS galaxies from § 2 are featureless galaxies in that they are not found to contain visible structure from examination of ground based images (of the three that are not, one is found to contain a dominant bar, another contains a faint ring, and the third demonstrates sharp plateaus in it's surface brightness profile). These 9 galaxies make up the focus of the study.

For comparison, we supplement our sample with additional galaxies from § 2 that follow similar featureless characteristics, but are not classified as OOPS galaxies. To reach a supplementary sample, we first excluded galaxies from the sample of § 2 that were designated to contain a bar or were classified as a transition galaxy. Through examination of color images, we then further excised from our sample galaxies in § 2 that contain visible structure, such as rings. Finally, the surface brightness profiles were examined for prominent bumps, plateaus, and disk truncations and galaxies containing them were excluded.

Our final sample contains 22 S0 galaxies; 9 of these are OOPS galaxies. Table 3.1 lists our sample galaxies along with relevant characteristics. We refer the reader to § 2.2 for further discussion of these characteristics and to § 2.5 for information on their global properties.

Table 3.1: Galaxy Characteristics

Galaxy	Type[1]	a[3](')	b[3](')	radial velocity[2](km s^{-1})	Distance[4](Mpc^{-3})	Inclination[5](°)	Type[6]
UGC04631	S0	1.1	1.0	4159	60.6	24.25	OOPS
UGC04901	S0-A?	1.1	1.1	8424	118.7	28.92	N
UGC04910	S0	1.0	0.6	8353	117.8	28.92	N
UGC04916	S0	1.2	0.9	8785	123.6	36.21	OOPS
UGC05075	S0-A	1.3	0.6	5435	79.0	26.61	N
UGC05182	S0	1.8	1.1	8692	123.2	34.61	OOPS
UGC05503	SB:0	2.3	1.3	1318	21.3	59.11	N
UGC05568	S0	1.7	0.8	2072	33.7	25.95	N
UGC08997	S0	1.1	0.6	7681	113.5	53.33	OOPS
UGC09156	S0	1.0	0.5	7705	114.2	67.00	OOPS
UGC09212	S0	1.1	0.8	8543	124.9	54.09	N
UGC09280	S0	1.1	0.8	8017	118.2	54.42	OOPS
UGC09321	S0	1.0	0.6	7671	113.5	0.00	OOPS
UGC09400	S0	1.2	1.2	8634	126.7	36.21	N
UGC09514	SB0	1.4	0.9	8205	121.1	49.99	N
UGC09999	S0?	1.2	0.7	9546	137.8	57.49	N
UGC10048	S0	1.1	0.7	3937	62.1	0.00	N
UGC10084	S0	1.7	0.5	13880	196.7	56.58	N

Table 3.1: Galaxy Characteristics

Galaxy	Type[1]	a[3](')	b[3](')	radial velocity[2](km s^{-1})	Distance[4](Mpc^{-3})	Inclination[5](°)	Type[6]
UGC10391	-	-	-	2438	40.9	47.86	OOPS
VCC1196	NA	1.0	0.7	909	16.5	61.95	OOPS
VCC1512	-	-	-	762	16.5	52.45	N
VCC1906	-	-	-	314	16.5	44.31	N

[1]Hubble type from UGC Catalog

[2]Heliocentric radial velocity (km s^{-1}) from NED

[3]Diameter is from UGC Catalog

[4]Distances are corrected for Virgo flow and the Great Attractor, from NED

[5]From UGC Catalog unless otherwise noted

[6]'OOPS': old outer population S0, 'N': not an OOPS

3.2.2 Observations

Our analysis of galaxy luminosity profiles is based on the images of S0 galaxies in § 2. Our database consists of deep H and/or J images of 22 nearby S0 galaxies. The NIR observations are from the ULBCam at the University of Hawaii's 2.2-m telescope. Nine galaxies were observed in the H band only, nine galaxies only in the J-band, and four galaxies were observed in both passbands. The decomposition analysis employs the NIR images because they minimize the effect of dust and follow the older stellar populations. However, we also use r band images as a useful check of our decompositions. The archival optical imaging is taken from the Sloan Digital Sky Survey (York et al. 2000, hereafter, SDSS). A full description of the sample selection, observations, reductions, and surface brightness profiles is presented in § 2.3 and 2.4.

3.3 Profile Fitting

3.3.1 Algorithm

In order to determine the contribution of the bulge and disk components to the galaxy light, we have developed an algorithm to decompose the 1D light distribution, using surface brightness profiles from § 2, into bulge and disk components. This program allows for a generalized Sersic bulge and an exponential disk. In this section the 1D fitting algorithm is described. We first discuss our choice of components and their functional forms, then our motivation for using the 1D method and our fitting routine are explained.

The Model Components

The analysis presented here uses a generalized sersic component for the 'bulge' and an exponential profile for the 'disk'. Previous work indicates that a general sersic law is a better fit to the bulge component than the special case of $n = 4$ (de Jong 1996a; Courteau et al. 1996; Carollo 1999; Graham 2001). In particular,

systems with lower bulge mass have been found to have, on average, lower Sersic n (de Jong 1996b; Graham 2001; Andredakis et al. 1995). The commonly used exponential profile for the disk is supported by the natural occurrence of an exponential profile in galaxy formation models (Dalcanton et al. 1997; Ferguson & Clarke 2001; Abadi et al. 2003). Our choice of fitting functions are restricted to a single bulge and a single disk component. Our sample does not contain prominent spiral arms, inner disks, rings, or bars that would warrant an additional or alternative component.

The first component is a spherically symmetric bulge with an generalized Sersic radial light distribution. Bulge parameters are normally expressed in effective parameters, giving the sersic law

$$I_b(r) \equiv I_e \; exp^{-B_n((\frac{r}{r_e})^{1/n}-1)}$$

or in magnitudes

$$\mu_b(r) \equiv \mu_e + 1.08574 \; B_n((\frac{r}{r_e})^{1/n} - 1)$$

where the effective radius (r_e) encloses half the total luminosity and I_e (μ_e) is the surface brightness in flux (magnitudes) at this radius. B_n is chosen to ensure that half the light is contained within r_e. Unfortunately, B_n cannot be solved for analytically. We have adopted the functional form used in MacArthur et al. (2003).

The second component, the disk, is described by an exponential law, which is a special case of the generalized Sersic law, with n=1. This component has the two free parameters, μ_o (central surface brightness) and h (disk scale length), and the form

$$I_d(r) \equiv I_o \; exp^{\frac{-r}{h}}$$

or in magnitudes

$$\mu_d(r) \equiv \mu_o + 1.08574 \; (\frac{r}{h})$$

We model the total galaxy luminosity profile as a sum of bulge + disk components:

$$I_{tot}(r) \equiv I_b(r) + I_d(r)$$

Observations of galaxies are distorted by wavelength dependent image blurring by the atmosphere and the model light distributions have to be corrected for this. To account for the seeing effects, the model profiles of the bulge were convolved with a Gaussian Point Spread Function (PSF). The PSF full width at half maximum (FWHM) for each galaxy frame is measured from the final stacked image in each bandpass and is the average of 5 individual foreground star PSFs. The uncertainty in the PSF is the standard error in the mean of the 5 individual PSFs.

The Fitting Routine

We have chosen to model the surface brightness profile in one dimension as it suffices for our goals of separating the major contribution of light between the bulge and disk. 2D fitting has the advantage to 1D fitting that non-axisymetric components can be fitted as well. However, the sample of S0 galaxies analyzed here do not contain prominent spiral arms, bars, or other non-axisymetric structure that would warrant the need for a more computationally intensive 2D B/D decompositions. These decomposition routines require additional free parameters, which are not necessary for our sample, providing larger room for uncertainty. MacArthur et al. (2003) show no improvements over using the 2D over the 1D decomposition method for axisymetric structure.

Our 1D bulge-to-disk decomposition algorithm reduces galaxy luminosity profiles into bulge and disk components simultaneously using a non-linear Levenburg Marquardt least-squares (Press et al. 1992) fitting routine. Profiles are fit in logarithmic intensities (i.e. magnitude units). The best fit parameters found from comparing the models to the data are those which minimize the reduced χ^2 merit function,

$$\chi^2_\nu \equiv \frac{1}{N-M} \sum_{i=1}^{N} \left(\frac{I_{gal}(r_i) - I_s(r_i; h_i, I_o, r_e, I_e, n)}{\sigma_i}\right)^2$$

Where N is the number of data points used, M is the number of free parameters, σ_i is the statistical intensity error at each surface brightness level, and I_{gal} and I_s are the galaxy data and simulated intensities, respectively. Whenever we quote a χ^2 in the remainder of the paper, we are are quoting this reduced χ^2 merit function.

Random errors are accounted for in the minimization, whereas systematic errors such as uncertainties in the sky background and determination of the image PSF are accounted for separately and described in § 3.3.3. The random errors used in the minimization algorithm are a standard deviation in the surface brightness around the best fit ellipse as described in § 2.4.4.

Of importance to our study is the relative light fraction contributed by the bulge and disk at various radii along the galaxies' light profile. We calculate a partial bulge-to-disk luminosity ratio, $(B/D)_{bin}$, where the "bin" indicates a radially binned region. $(B/D)_{bin}$ is derived by summing the luminosity of the bulge and disk components separately for each data point within the particular radial range. The ratio of the luminosity from the bulge to the disk defines $(B/D)_{bin}$. To compare with stellar population results of § 2, we chose the radial bins used in that paper, which are defined by total effective radii, R_e. Note that R_e is not the effective radius of the Sersic component, which we designate as r_e.

We have also calculated a total bulge-to-disk luminosity ratio, $(B/D)_{tot}$, derived by integrating the bulge and disk luminosity profiles to infinity,

$$I_b \equiv \int_0^\infty I_b(r) 2\pi r \, dr$$

$$I_d \equiv \int_0^\infty I_d(r) 2\pi r \, dr$$

and taking their ratio.

Both $(B/D)_{bin}$ and $(B/D)_{tot}$ are valid for face-on bulges and disks, or independent of projection, under the assumption that the bulge and disk density distributions have similar axes ratio (MacArthur et al. 2003). Our sample consists primarily of face-on galaxies with all inclinations < 70 degrees. Because our primary analysis focuses on

the change in $(B/D)_{bin}$ with radius, we do not believe inclination dependence to affect our results.

3.3.2 Initial Parameters and Fitting Procedure

In order to determine the best fit bulge and disk parameters, we need to provide the minimization program with the appropriate choices for initial parameter estimates. We obtained the disk initial parameters first, using the "marking the disk method" (Freeman 1970; de Jong 1996a; MacArthur et al. 2003). The linear part of the luminosity profile, plotted on a magnitude scale, was marked by eye and a linear least squares fit was made to the data points in the indicated range. The outer limit for the fitting region was set to the outer radial cutoff used in § 2 which was chosen there to minimize sky effects. This method is only used for initial estimates of disk parameters while the final fits are made on the entire galaxy image. The two initial estimates needed for a model exponential profile are disk scale length, h, and the central surface brightness, μ_o. In agreement with MacArthur et al. (2003), we found that the fits were robust to the choice of initial disk scale length. The determination for μ_o was based on extrapolation of the linear region (by eye) to the center.

Once a fit to the disk component was made, we fit a sersic profile to the inner region to obtain the bulge parameters. The best fit parameters found for the disk were held fixed while the inner region was fit. The residual from the "marking the disk" procedure was examined to determine the outer limit to the fitting region for the bulge; the fitting region begins at the center unless otherwise noted. We have tried other methods of bulge fitting, such as fitting only the residual from the marking the disk step, as well as fitting the entire galaxy while holding the disk parameters. We found that these later methods produce final fits with greater reduced χ^2. In 3 cases, we used the entire radial range for the fit because the bulge component only dominated at small radii. The bulge free parameters are the effective radii, r_e, and the effective surface brightness, μ_e. The initial r_e was chosen to be $0.15h$, based on work by MacArthur et al. (2003) and motivated by correlations in bulge and disk scale lengths

(Courteau et al. 1996). The initial μ_e was set to the best fit μ_o from the exponential fit. Although we have the option of letting n be another free parameter in our fits, to reach more stable results the fits were made with n fixed to values between 0.1 and 4.0, with increments of 0.1. The fit which gave the lowest chi squared from n=0.1 to 4.0 was chosen for the best fit parameters. This is essentially the same concept as letting n be a free parameter, while avoiding erratic solutions.

The luminosity profile at all radii is a combination of the bulge and disk light. To get correct results, both the bulge and the disk should be fitted simultaneously. Thus, once best fit parameters were found by fitting each component separately, the entire galaxy was modeled using these parameters as initial guesses, allowing each parameter, except for the Sersic index n, to vary. These fits are performed from the center of the galaxy to the outer cutoff that was used in "marking the disk". Again, the sersic n value was varied from 0.1 to 4.0 through iterations of the routine. The lowest chi squared from these were chosen as the final best fit parameters.

The motivation for setting our initial r_e to $0.15h$ is based off the work of Courteau et al. (1996) that outlines the correlations in scale lengths of the bulge and disk. Although the ratio of scale lengths was shown to be independent of galaxy type, S0 galaxies were not studied and these correlations may not be valid for our sample. Therefore, to determine the sensitivity of our final parameters to this setting, we have performed fits using more extreme values for r_e, namely $0.1h$ and h. We did not use an initial r_e greater than h because we do not consider such large bulges to be physical solutions. Fits were also performed by changing the initial μ_e. We have found that the best-fit μ_e values vary in our sample by ~ 4 magnitudes. Therefore, we varied the initial guess for μ_e by $\pm$ 2 mag. For each variation, the routine generally converged to the same result, independent of the initial values. Exceptions to this are discussed in detail in § 3.3.4. Because n was found from a grid search, no test was needed to estimate the sensitivity of an initial estimate of that parameter.

The best fit parameters are given in Table 3.3, along with the final radial range of the fit, the psf, and the reduced χ^2. The B/D ratios for total bulge and disk

luminosities and at various radial ranges are given in Table 3.4. Because not all galaxies share the same radial extent, the radial bins farthest from the center of the galaxy are not measured in some galaxies. An example decomposition is provided in Fig. 3.1 for UGC 4631. The surface brightness profile for the J band data is overlaid with the model containing the final, best-fit parameters in black and green, respectively. The error bars shown on the data at each radius designate the $\pm$ 1 σ errors in the surface brightness. Interior to the outer radial cutoff, surface brightnesses are not plotted for radii where the error in surface brightness exceeds 0.1 mag. It is clear in Fig. 3.1 that the model fits the data well at all points except the outermost region of the galaxy. Because the surface brightness error is greater at this region, the fitting routine did not place as much weight there. To demonstrate the contribution from the Sersic and exponential components, each separate component is plot in blue and magenta, respectively. The best-fit parameters for each component are provided in the upper right corner.

Table 3.2: Best Fit Parameters

Name	r_i(")	r_f(")	FWHM(")	χ^2	h	σ_h	μ_o	σ_{μ_o}	r_e	σ_{r_e}	n	σn	μ_e	σ_{μ_e}
OOPS														
UGC04631	0.00	36.00	1.25	18.19	8.87	0.24	18.57	0.04	1.94	0.07	1.70	0.11	17.32	0.09
UGC04916	0.00	39.00	1.19	2.50	10.23	0.31	18.96	0.04	2.94	0.03	1.50	0.00	17.08	0.02
UGC05182	0.00	50.00	1.63	13.62	11.94	0.66	18.49	0.15	3.75	0.19	1.90	0.07	16.88	0.09
UGC08997	0.00	48.00	1.32	4.40	14.14	1.02	18.81	0.12	4.28	0.25	2.00	0.07	17.63	0.09
UGC09156	0.00	80.00	1.30	7.13	16.26	0.41	18.73	0.18	10.75	1.45	2.90	0.16	18.67	0.20
UGC09280H	0.00	60.00	1.10	10.31	16.11	0.82	18.65	0.10	5.12	0.26	2.50	0.11	17.44	0.08
UGC09280J	0.00	65.00	1.14	5.80	17.34	1.24	19.60	0.15	5.82	0.55	2.70	0.14	18.46	0.17
UGC09321	0.00	75.00	1.50	223.53	72.52	10.31	21.76	0.12	10.70	0.16	3.00	0.05	18.04	0.03
UGC10391J	0.00	28.00	1.00	18.10	9.36	0.46	17.99	0.09	3.17	0.14	1.60	0.07	17.04	0.07
UGC10391H	0.00	36.00	1.10	22.14	8.57	0.13	17.16	0.03	2.97	0.02	1.60	0.00	16.31	0.02
VCC01196	0.00	55.00	1.20	2.98	15.00	0.64	18.55	0.12	8.26	0.73	2.20	0.07	18.71	0.10
Non-OOPS														
UGC04901	0.00	85.00	1.00	23.90	25.09	1.14	19.78	0.09	6.98	0.21	2.10	0.05	18.13	0.05
UGC04910	0.00	60.00	1.30	22.49	16.57	0.96	19.54	0.11	4.45	0.17	2.00	0.07	17.76	0.06
UGC05075	0.00	32.00	1.65	15.52	5.99	0.03	17.20	0.01	1.40	0.04	1.10	0.05	15.75	0.04
UGC05503	0.00	75.00	1.30	30.41	9.80	0.07	17.35	0.02	33.36	1.93	4.00	0.00	21.14	0.06
UGC05568	0.00	65.00	2.50	5.35	7.84	0.63	18.87	0.20	16.76	0.62	2.80	0.05	18.79	0.08

Table 3.2: Best Fit Parameters

Name	r_i(")	r_f(")	FWHM(")	χ^2	h	σ_h	μ_o	σ_{μ_o}	r_e	σ_{r_e}	n	σn	μ_e	σ_{μ_e}
UGC09212	0.00	60.00	1.30	28.48	19.55	1.35	20.41	0.15	5.72	0.20	2.10	0.07	18.26	0.06
UGC09400J	0.00	50.00	1.20	4.91	15.47	1.28	19.89	0.13	4.63	0.14	2.00	0.05	17.86	0.06
UGC09400H	0.00	60.00	1.10	22.76	15.05	0.18	19.15	0.02	4.69	0.03	2.00	0.00	17.15	0.01
UGC09514	0.00	55.00	1.35	15.20	15.18	1.01	18.99	0.12	4.42	0.15	2.00	0.05	17.13	0.05
UGC09999	0.00	75.00	1.10	31.16	16.04	0.60	18.41	0.08	4.73	0.19	2.30	0.05	17.10	0.06
UGC10048	0.00	40.00	1.45	12.35	15.30	1.58	19.69	0.11	4.35	0.03	1.90	0.00	16.61	0.01
UGC10084J	0.00	60.00	1.35	10.34	16.71	1.30	19.90	0.17	5.36	0.28	1.90	0.07	18.20	0.08
UGC10084H	0.00	60.00	1.35	8.79	14.95	1.18	18.84	0.15	4.90	0.22	1.80	0.05	17.32	0.07
VCC01512	0.00	24.00	1.42	2.63	6.03	0.19	17.63	0.04	1.89	0.06	1.00	0.10	18.02	0.09
VCC01906	0.00	17.00	1.10	2.20	3.95	0.04	17.08	0.03	2.00	0.10	0.70	0.05	18.90	0.05

Table 3.3: Bulge/Disk Ratios

Name	$(B/D)_{bin1}$	σ_1	$(B/D)_{bin2}$	σ_2	$(B/D)_{bin3}$	σ_3	$(B/D)_{bin4}$	σ_4	$(B/D)_{bin5}$	σ_5	$(B/D)_{bin6}$	σ_6	$(B/D)_{tot}$	σ_{tot}
OOPS														
UGC04631	2.50	0.12	0.07	0.01	0.00	0.00	0.00	0.00	—	0.00	—	0.00	0.42	0.01
UGC04916	9.66	0.27	0.79	0.02	0.05	0.00	0.01	0.00	0.00	0.00	—	0.00	1.12	0.02
UGC05182	10.63	1.24	1.12	0.17	0.17	0.04	0.05	0.01	0.02	0.01	0.01	0.00	1.20	0.08
UGC08997	10.60	1.18	1.54	0.21	0.33	0.06	0.11	0.03	0.05	0.01	0.03	0.01	0.75	0.04
UGC09156	9.08	1.57	1.92	0.43	0.82	0.24	0.58	0.19	0.51	0.19	0.51	0.20	1.47	0.33
UGC09280H	8.26	0.79	0.89	0.10	0.20	0.03	0.09	0.02	0.06	0.01	99.99	0.00	0.93	0.05
UGC09280J	9.46	1.39	1.10	0.19	0.28	0.07	0.14	0.04	0.09	0.03	0.08	0.03	1.01	0.09
UGC09321	210.88	21.53	27.69	2.48	6.76	0.62	2.67	0.26	1.31	0.14	0.74	0.09	2.18	0.50
UGC10391J	5.15	0.47	0.58	0.07	0.06	0.02	0.02	0.01	—	0.00	—	0.00	0.67	0.04
UGC10391H	4.44	0.09	0.47	0.01	0.05	0.00	0.01	0.00	0.00	0.00	—	0.00	0.64	0.01
VCC01196	3.10	0.40	0.58	0.11	0.20	0.06	0.14	0.05	—	0.00	—	0.00	0.72	0.10
Non-OOPS														
UGC04901	14.23	1.06	1.91	0.16	0.38	0.04	0.13	0.01	0.06	0.01	0.03	0.01	0.96	0.04
UGC04910	13.01	1.06	1.36	0.12	0.21	0.03	0.06	0.01	0.02	0.00	0.01	0.00	1.02	0.04
UGC05075	4.18	0.10	0.14	0.00	0.00	0.00	0.00	0.00	0.00	0.00	0.00	0.00	0.51	0.01
UGC05503	1.18	0.04	0.60	0.04	0.84	0.08	1.83	0.22	4.88	0.67	10.24	1.53	1.28	0.12
UGC05568	17.23	3.72	9.43	1.62	14.18	1.82	35.00	11.89	98.09	58.32	—	0.00	15.37	2.45
UGC09212	34.68	4.26	5.61	0.65	1.32	0.17	0.51	0.08	0.24	0.04	0.14	0.04	1.71	0.10
UGC09400J	18.77	1.71	2.41	0.23	0.46	0.06	0.15	0.03	0.07	0.01	0.04	0.01	1.57	0.08
UGC09400H	18.66	0.37	2.47	0.06	0.48	0.01	0.16	0.00	0.07	0.01	0.04	0.00	1.66	0.03
UGC09514	14.23	1.49	1.62	0.17	0.28	0.04	0.09	0.01	0.04	0.01	0.02	0.01	1.29	0.04
UGC09999	8.36	0.58	0.88	0.09	0.17	0.02	0.07	0.01	0.03	0.01	0.02	0.01	0.84	0.04
UGC10048	66.49	5.41	10.57	0.56	2.25	0.03	0.75	0.03	0.32	0.03	0.16	0.02	3.71	0.39
UGC10084J	13.78	2.21	1.83	0.33	0.33	0.08	0.11	0.03	0.04	0.03	0.03	0.01	1.30	0.10
UGC10084H	10.46	1.41	1.32	0.20	0.21	0.04	0.06	0.01	0.02	0.01	0.01	0.01	1.12	0.05
VCC01512	0.44	0.03	0.00	0.01	0.00	0.00	—	0.00	—	0.00	—	0.00	0.14	0.01

Table 3.3: Bulge/Disk Ratios

Name	$(B/D)_{bin1}$	σ_1	$(B/D)_{bin2}$	σ_2	$(B/D)_{bin3}$	σ_3	$(B/D)_{bin4}$	σ_4	$(B/D)_{bin5}$	σ_5	$(B/D)_{bin6}$	σ_6	$(B/D)_{tot}$	σ_{tot}
VCC01906	0.31	0.01	0.03	0.01	0.00	0.00	—	0.00	—	0.00	—	0.00	0.08	0.01

3.3.3 Uncertainties

The formal uncertainties on the final parameter values of the least squares fitting routine do not represent the overall uncertainties. Therefore, we ran follow up procedures to get reliable uncertainties from the systematic errors in sky subtraction and PSF measurement errors.

Once a satisfactory fit was found, we performed additional decompositions using data adjusted to using $\pm$ 1 σ systematic sky error, as defined in § 2.4.4. The largest change in final parameters was found to be the disk scale length, which varies by an average of 8.4% between + and - 1 σ systematic sky profiles. We consider the half of the difference in parameters of the two fits to be the sky systematic error in the best fit parameters.

In a similar manner, we have performed tests of the uncertainties due to PSF measurement errors. Additional decompositions were run using a model fitting function convolved with a PSF adjusted to $\pm$ 1 σ PSF error, as defined in § 3.2.2. The parameters with the largest difference were found to be the Sersic index, n, and the effective radius, r_e, which vary by an average of 2.2 % and 1.8%, respectively. The average difference in parameters between each adjusted psf fit and the original is considered to be the PSF systematic error in the best fit parameters.

The final error quoted for the disk and bulge parameters includes the formal model uncertainty, the sky systematic error, and the PSF systematic error, all added in quadrature. No formal error is available for the Sersic index n because we used a grid search to determine the final parameter, but the coarseness in the grid introduces an uncertainty in the parameter. Thus, we consider the step size in the grid, 0.1, to be the lower limit to the uncertainty in n. Errors on B/D ratios are calculated in a similar manner as bulge and disk parameters, however the final error only includes the sky systematic error and the PSF systematic error, added in quadrature. The final uncertainties for bulge and disk parameters are provided in Table 3.3 and for B/D ratios in Table 3.4.

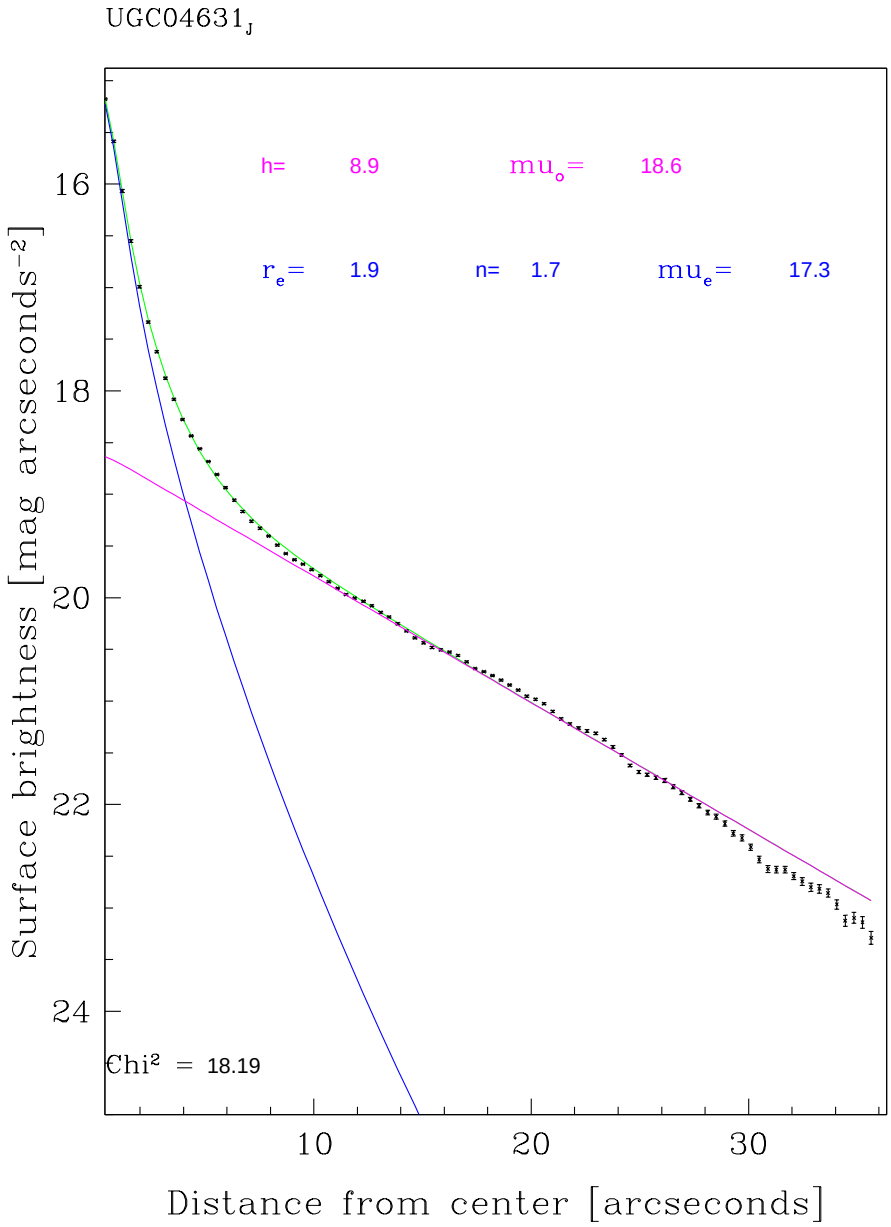

Figure 3.1 Model decompositions for an example galaxy, UGC 4631. Best fit model decompositions are shown in green and galaxy J band data points are shown as black x's. The model components are separated into the Sersic profile (blue) and the exponential (magenta) and their parameters are given in the top right corner. The χ^2 for the model is given in the bottom left corner. Surface brightness errors of 1 σ are shown on each radial point for the data.

3.3.4 Robustness of Fits

In addition to testing for systematic uncertainties due to sky subtraction and PSF measurement errors, we also examine the robustness of our profile decompositions through comparisons of J and H band model fitting, tests for degeneracies and the effects of nuclear star formation, and finally, comparison with decompositions in the literature.

First, we compare the profile fitting of galaxies that have both J and H band data available, namely UGC 9280, UGC 9400, UGC 10084, and UGC 10391. The best fit models for the J band data and the H band data are shown in the left and right panels of Fig. 3.2, respectively. The parameters, h, μ_o, and μ_e are found to always be greater in the J-band decomposition than the H-band, while the Sersic n value is nearly consistent. The largest difference between the H and J band decompositions is in the disk scale length, h, and the effective radius, r_e. The disk scale length is found to vary at most by 11% and the effective radius by 12%, in UGC 10084 and UGC 9280, respectively. For any following analysis where we wish to combine the results of the H and J band decompositions, we follow the action in § 2 where we quoted results for any galaxies that have H-band imaging to be based on that band alone (see § 2.7.1).

Non-linear fitting algorithms may be sensitive to the initial values provided; if the initial values are not reasonable, the fitting program can end up in a wrong local minimum. MacArthur et al. (2003) performed detailed tests on idealized galaxies to determine the reliability and limitations of 1D and 2D decompositions. They found that initial estimates for bulge and disk parameters are unimportant for galaxies with larger effective radii, r_e, and defined a specific parameter regime, dependent on n and the FWHM, where results are robust to initial estimates. We find that all of our final decompositions result in an r_e that is in this regime. Because our decomposition routine follows a similar prescription as MacArthur et al. (2003), we believe that this reliability holds for our estimates as well. Nevertheless, after the best fit parameters were found, we varied the initial estimates for the bulge component, as described in

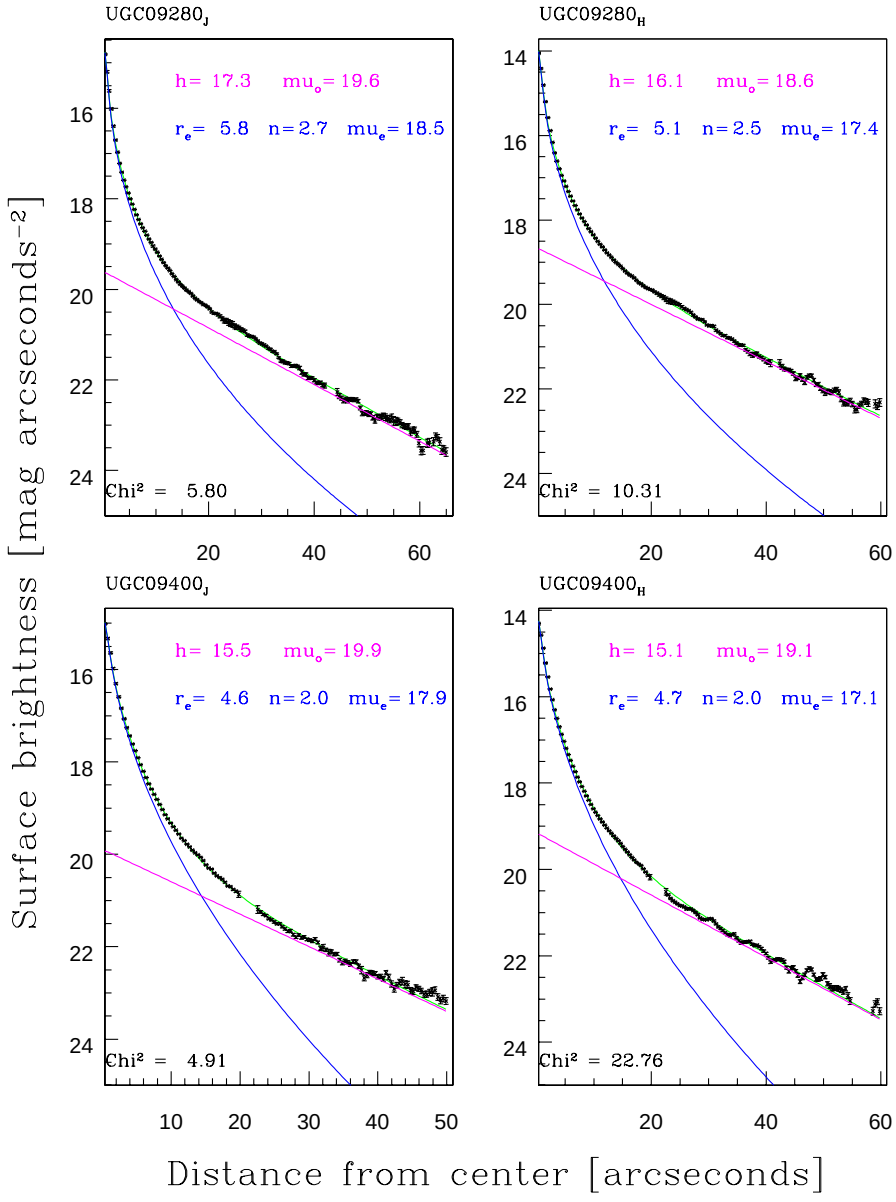

Figure 3.2 Model decompositions for galaxies with both J and H band data available. The left panel shows the J band images, and the right panel shows the H band data. Colors and symbols are as in Fig. 3.1.

§ 3.3.2, to provide our own test to the stability of the initial parameters. For all but one galaxy, UGC 5503 which is described below, the routine converged to the same result.

In one dimension, the galaxy bulge and disk may appear to merge smoothly, but there may actually be isophotal twists and ellipticity changes that can cause nonuniqueness in the decompositions. In 2 cases, UGC 10048 and UGC 5503, degenerate fits were found such that largely different parameters gave similar χ^2 values. We show both fits for each of these galaxies in Fig. 3.3. For UGC 5503, the fit on the left is the original fit found by following the procedure outlined in § 3.3.2 to find initial parameters. However, when we adjust the initial parameters by using a lower μ_e, a lower χ^2 is reached for a largely different set of parameters, as shown on the right of Fig. 3.3. There appears to be two difficulties in obtaining a satisfactory fit: the outer region of the galaxy drops in surface brightness around 67" and the inner region is steeply peaked to high surface brightness. We discuss the inner region below in terms of a nuclear component. The fit on the right has a central disk with a disk scale length much smaller than r_e, which we consider to be an unphysical solution. For UGC 10048, two local minima were found in the Sersic n plane while performing a grid search. Both are shown in the lower panels of Fig. 3.3. While the fit shown on the right has a lower χ^2 than the fit on the left, it is not as robust to changes in initial parameters or sky background adjustments. Therefore, we believe the fit on the left to represent the best choice of parameters for UGC 10048 and use that fit for remaining analysis.

Another source of uncertainty in our fits is the possible contamination of the central region from star clusters and nuclear disks, which can bias the bulge, and hence disk, parameters. For example, previous studies show that larger Sersic indices were found when using low-resolution ground-based data, which smear out the flux from the unresolved nuclear components (Balcells et al. 2007; Andredakis et al. 1995) than with higher resolution HST studies which accounted for these components (Balcells et al. 2003). We have examined the surface brightness profiles, by eye, for a sharp break in

brightness at small radii. We found 2 galaxies, UGC 9321 and UGC 5503, that indicate an additional nuclear component. For these galaxies, we have performed additional decompositions that avoid the inner 3". We show the resultant decompositions in the right panels of Fig. 3.4, while the left panel shows the original decompositions (starting at 0"). In both galaxies, avoiding the central region in the decompositions produces a model profile fit with lower r_e and μ_e and hence a larger disk dominance in the outer regions.

UGC 5503, which was discussed above in regards to degenerate fits, does not contain a degeneracy when avoiding the central radii in the fitting. All three decompositions for UGC 5503 (the two degenerate fits and the nucleus-excluded fit) produce a wide range in parameters. Hence, while the fit that avoids the nuclear region seems the most reasonable (and has the lowest reduced χ^2), we do not include this galaxy in future analysis due to the large uncertainties. This galaxy is likely to have a better fit using a more involved decomposition routine. UGC 9321 does not show as significant of a change as UGC 5503, but the radius of transition from bulge dominated to disk dominated light changes by $\sim 40\%$. Again, this galaxy might be better fit by a more involved decomposition routine. For consistency, we use the original fit for UGC 9321 in future analysis, but we consider the difference in parameters between the two fits to be an indication of possible errors.

Most of the galaxies in our sample do not have decompositions available in the current literature. However, Virani et al. (2000) has performed decompositions of UGC 9321 using an $n = 4$ bulge component and an exponential disk. They excluded the innermost pixels in their routine in order to avoid a contribution from any nuclear component. The data used by Virani et al. (2000) is in the Cousins R filter. Their best fits provide the following parameters: $h = 22.1 \pm 3.8$ kpc, $\mu_o = 23.00 \pm 0.24$ mag arcsec^{-2}, $r_e = 7.3 \pm 0.2$ kpc, $\mu_e = 20.50 \pm 0.03$ mag arcsec^{-2}. The difference in μ_e and μ_o is 2.5 mag arcsec^{-2}. To improve our comparison, we use the final parameters from the nucleus-excluded model fit. Converting our scale lengths to kpc, we find the best-fit parameters: $h = 21.2 \pm 1.26$ kpc, $\mu_o = 20.50 \pm 0.04$, $\mu_e = 17.75 \pm 0.01$,

$r_e = 5.00 \pm 0.02$ kpc, with a difference in μ_e and μ_o of 2.8 mag arcsec^{-2}. Our disk scale length and difference in μ_e and μ_o match that of Virani et al. (2000) within errors, but our effective radius is lower. As we discussed in the above paragraphs, UGC 9321 is a difficult galaxy to fit because it appears to have a central component that we are not fitting. Virani et al. (2000) fits a gaussian to the nucleus in addition to avoiding the inner few arcseconds. It is possible that our r_e is lower than that of Virani et al. (2000) because the fitting routine is trying to compensate for the additional central light. We note additional differences in our methods include choice of bandpass and allowing the Sersic n to vary. To better conform to their methods, we use the SDSS r band surface brightness profile for the fit and hold Sersic n to 4. In this case we find $h = 48.5$, $\mu_o = 24.0$, $r_e = 7.1$, $\mu_e = 21.07$, and a difference in μ_e and μ_o of 2.9 mag arcsec^{-2}. The effective radius of this fit agrees with that of Virani et al. (2000), within errors, but our disk scale length is now higher by a factor of two. We again attribute the offset in our values to the difficulty in fitting this galaxy.

3.4 Results

3.4.1 Best-fit Parameters

The main goal of our study is to determine whether the old regions of OOPS galaxies are disk or bulge dominated. Fig. 3.5 presents the best fit model from the two-component profile fitting routine for the 9 OOPS galaxies in both J and H passbands when available, while Fig. 3.6 presents them for the 13 non-OOPS galaxies. It is clear that nearly all galaxies in our sample show outer regions that are disk dominated. Exceptions to this are UGC 9156 and UGC 9321, both OOPS galaxies, which show a heavier bulge contribution in the outer region, and UGC 5503 and UGC 5568, neither OOPS galaxies, which are fully bulge dominated in the outer region.

The results from Fig. 3.5 suggests that the disk component is responsible for the old ages in most OOPS galaxies. Before further analysis into this claim, we discuss

the best fit bulge and disk parameters for all galaxies in our sample. The bulge and disk parameters and their correlations can be easily compared with those presented in the literature, allowing a useful check on our modeling procedures. As well, we use the bulge and disk parameters to search for any obvious differences in the OOPS galaxies from the other galaxies in our sample.

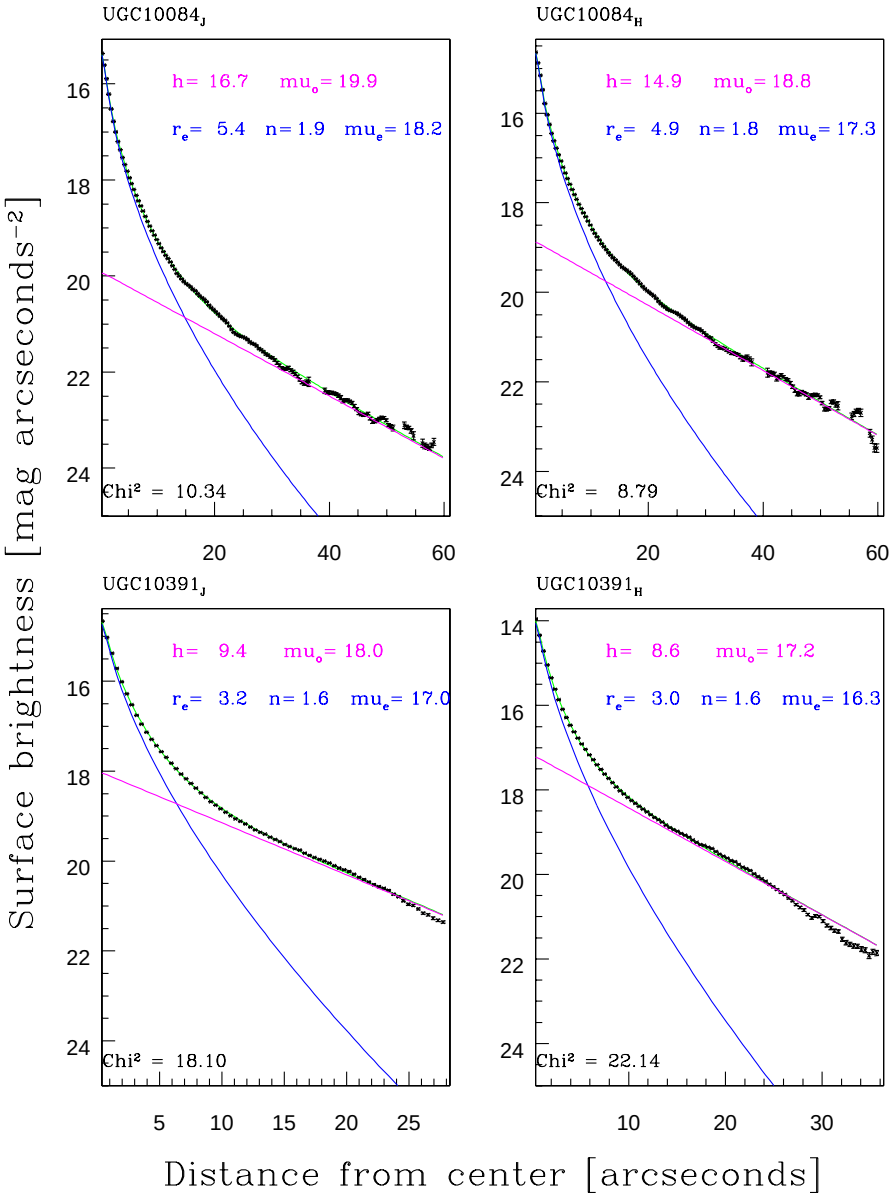
UGC10084J
h= 16.7 muo= 19.9
re= 5.4 n= 1.9 mue= 18.2
Chi² = 10.34
UGC10084H
h= 14.9 muo= 18.8
re= 4.9 n= 1.8 mue= 17.3
Chi² = 8.79
UGC10391J
h= 9.4 muo= 18.0
re= 3.2 n= 1.6 mue= 17.0
Chi² = 18.10
UGC10391H
h= 8.6 muo= 17.2
re= 3.0 n= 1.6 mue= 16.3
Chi² = 22.14
Surface brightness [mag arcseconds⁻²]
Distance from center [arcseconds]

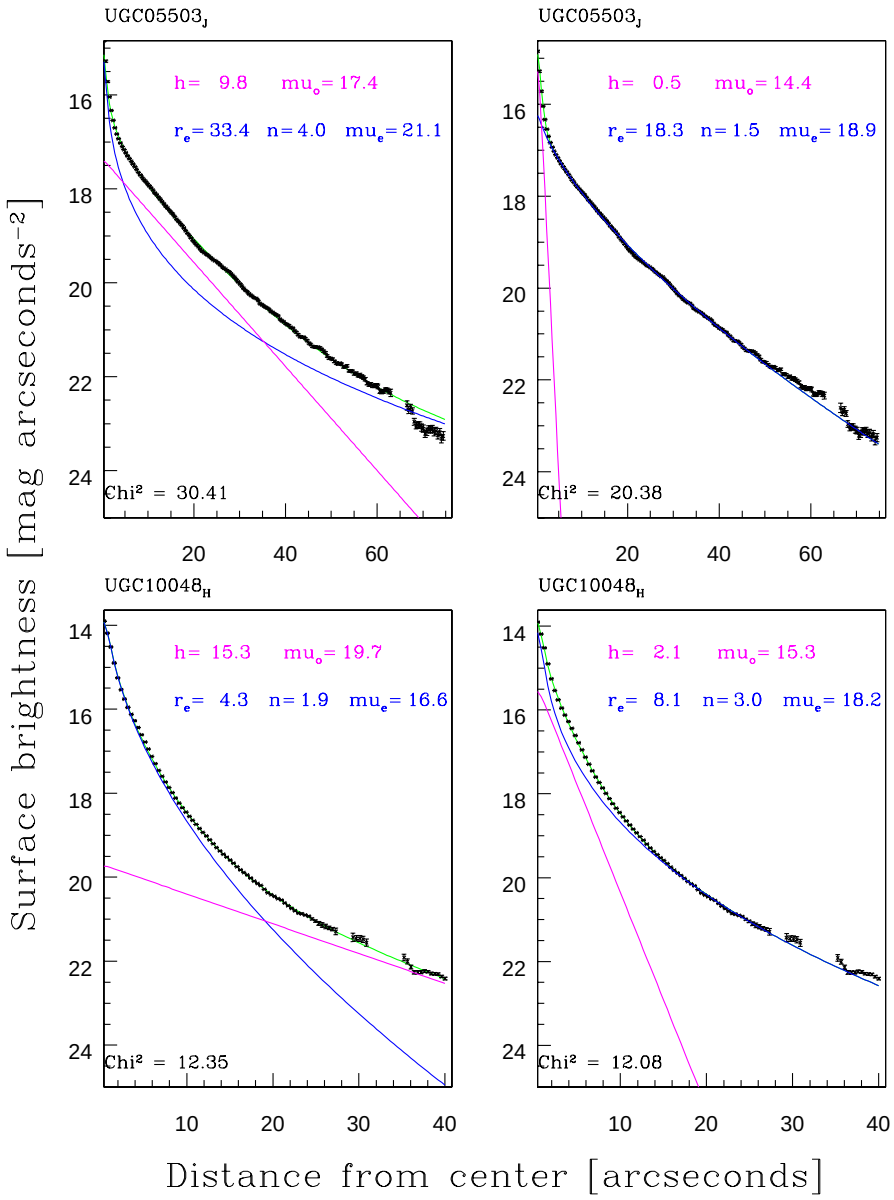

Figure 3.3 Model decompositions for galaxies showing degenerate fits. Colors and symbols are as in Fig. 3.1.

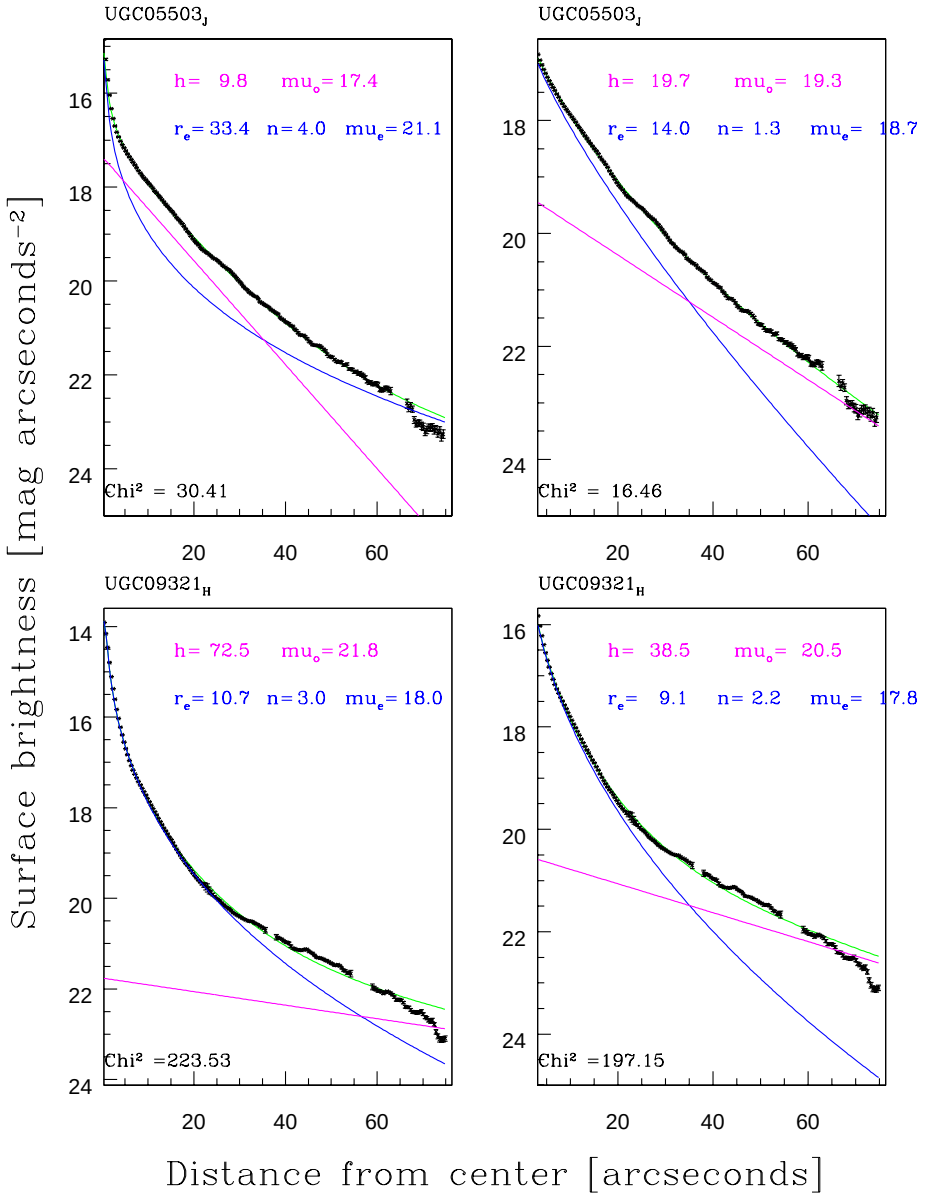

Figure 3.4 Model decompositions for galaxies showing a possible nuclear component. The left panel shows original fits starting at the center. The right panel shows a the resultant parameters when the nucleus is excluded. Colors are as in Fig. 3.1.

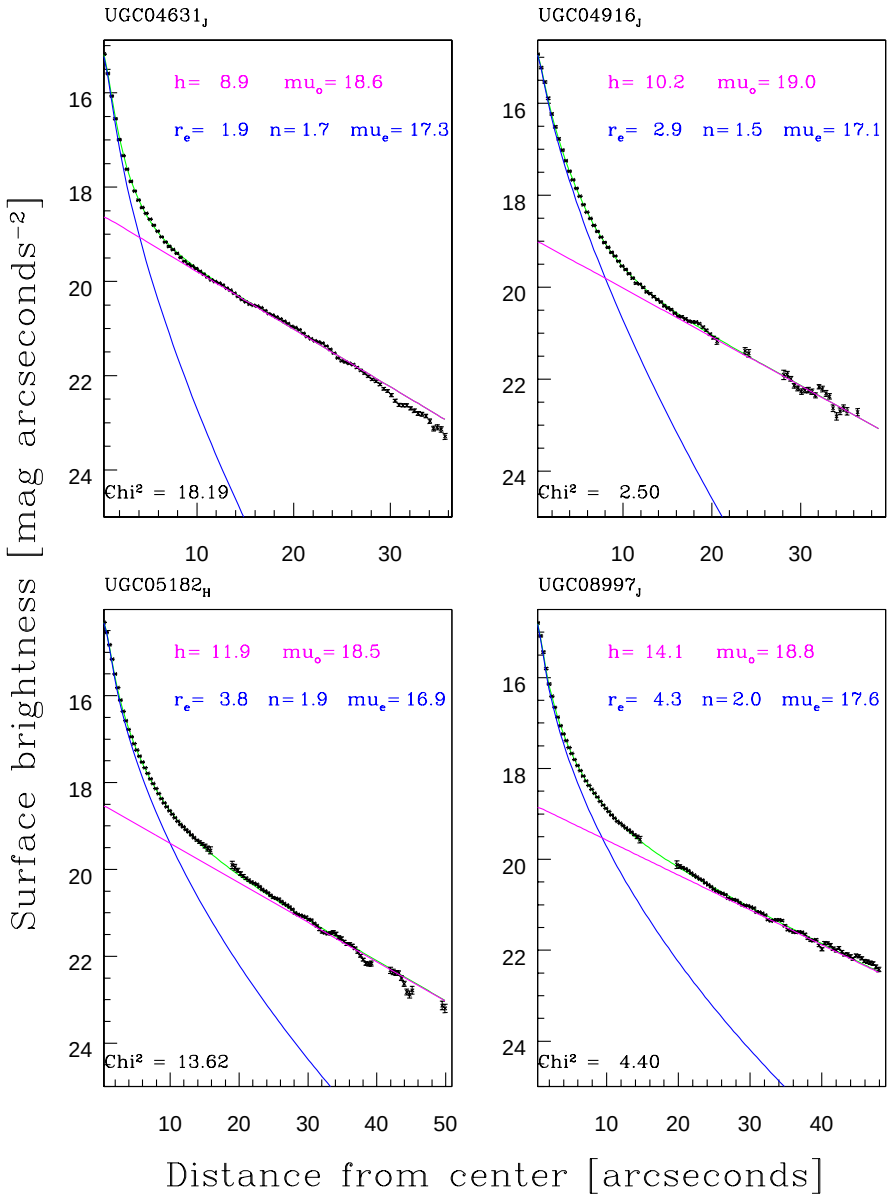

Figure 3.5 Profile fitting for OOPS galaxies. Best fit model decompositions are shown in green and galaxy data points are shown in black. The components are separated into the Sersic profile (blue) and the exponential (magenta) and their parameters are given in the top right corner. The χ^2 for the model is given in the bottom left corner.

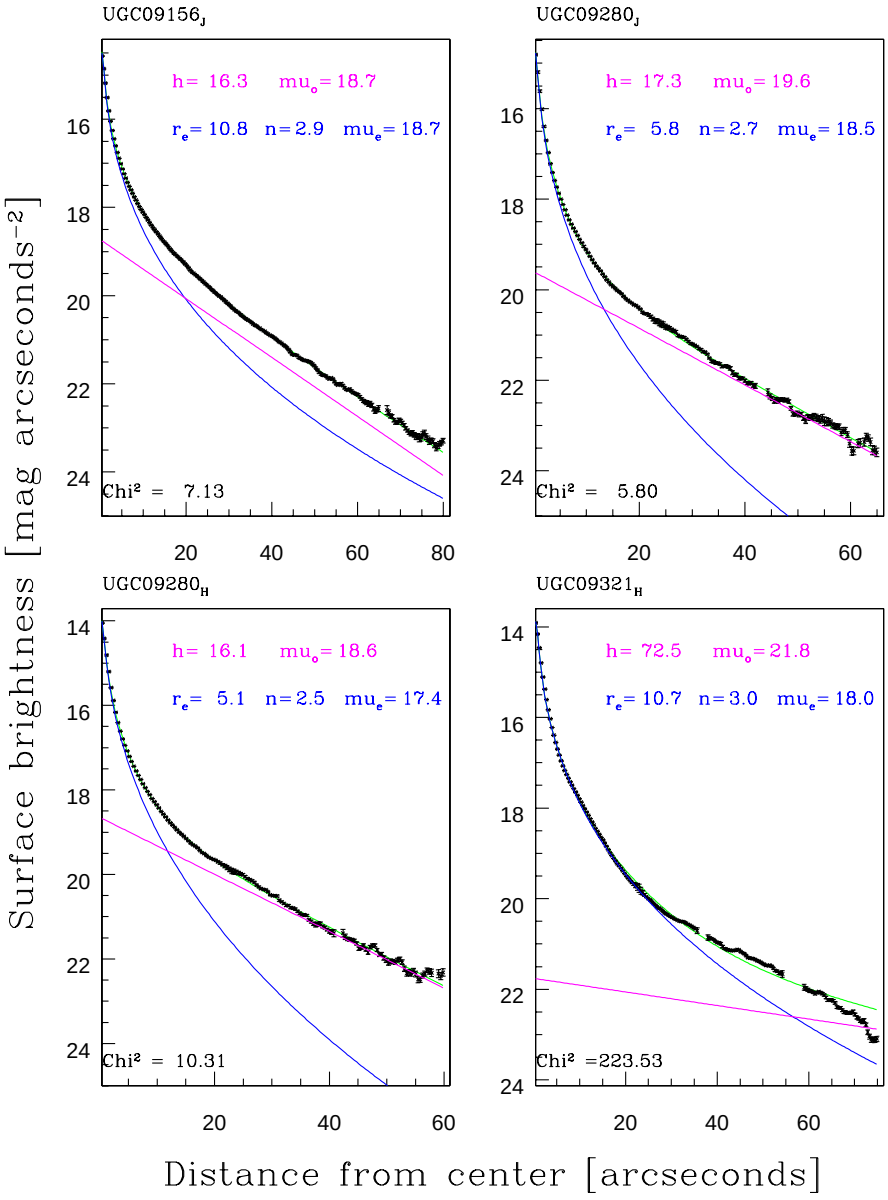
UGC09156J
h= 16.3 mu0= 18.7
re= 10.8 n=2.9 mue= 18.7
Chi² = 7.13
UGC09280J
h= 17.3 mu0= 19.6
re= 5.8 n=2.7 mue= 18.5
Chi² = 5.80
UGC09280H
h= 16.1 mu0= 18.6
re= 5.1 n=2.5 mue= 17.4
Chi² = 10.31
UGC09321H
h= 72.5 mu0= 21.8
re= 10.7 n=3.0 mue= 18.0
Chi² =223.53
Surface brightness [mag arcseconds⁻²]
Distance from center [arcseconds]

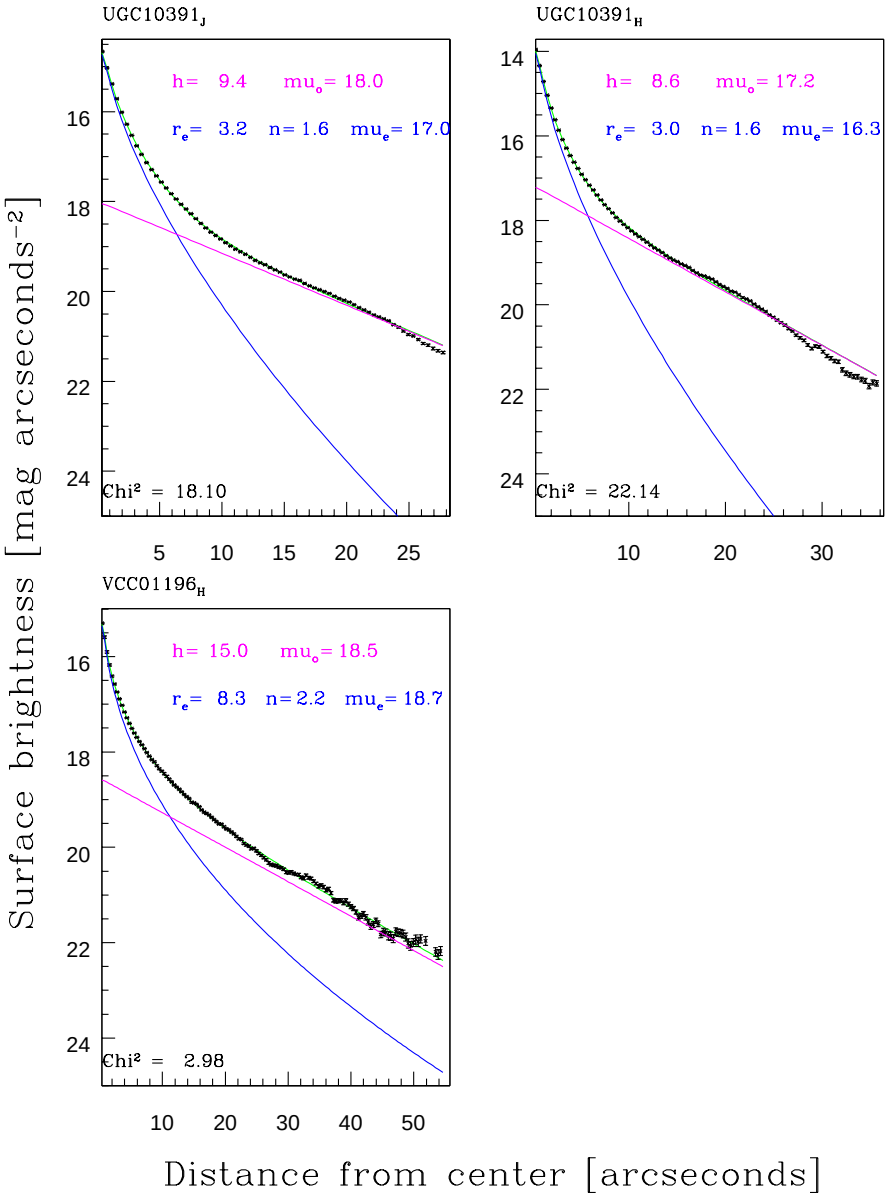
UGC10391J
h= 9.4 mu0= 18.0
re= 3.2 n= 1.6 mue= 17.0
Chi² = 18.10
UGC10391H
h= 8.6 mu0= 17.2
re= 3.0 n= 1.6 mue= 16.3
Chi² = 22.14
VCC01196H
h= 15.0 mu0= 18.5
re= 8.3 n= 2.2 mue= 18.7
Chi² = 2.98
Surface brightness [mag arcseconds⁻²]
Distance from center [arcseconds]

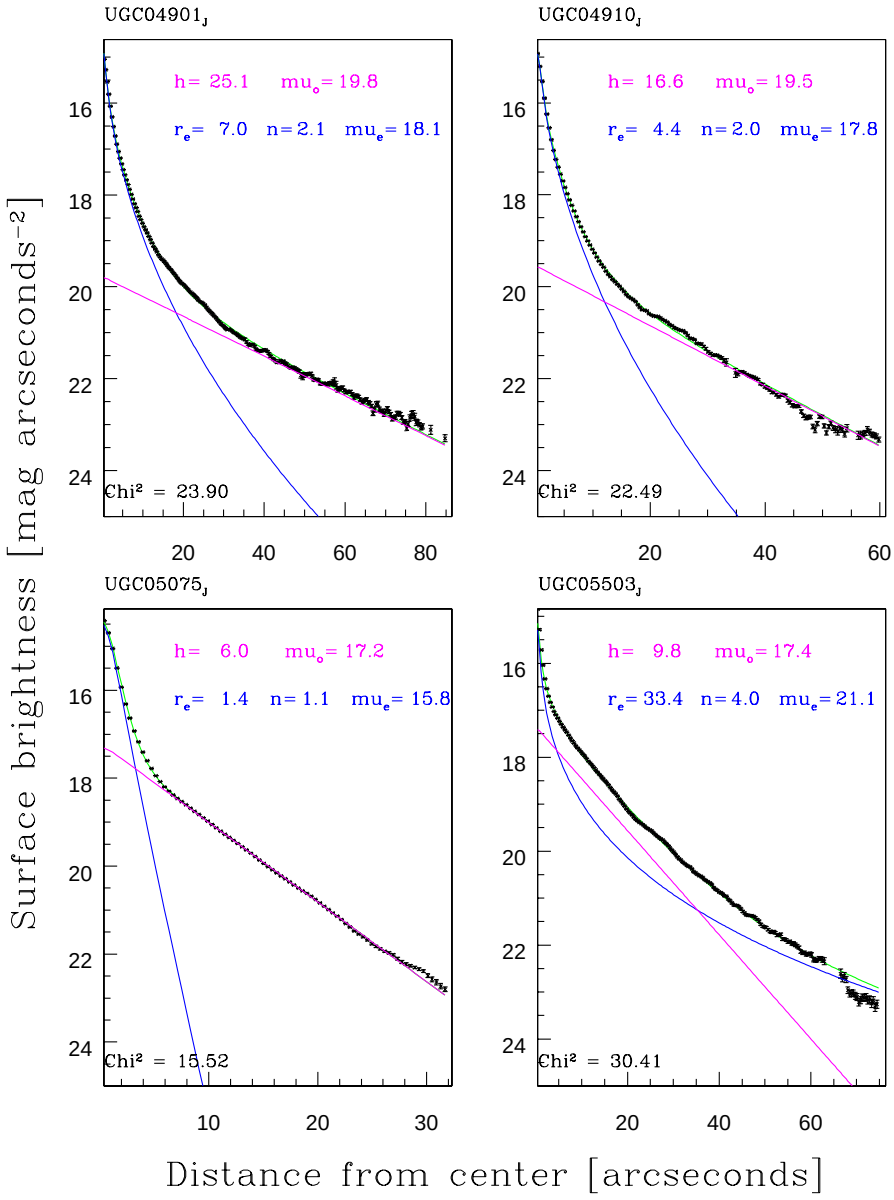

Figure 3.6 Same as Fig. 3.5, but for non-OOPS galaxies

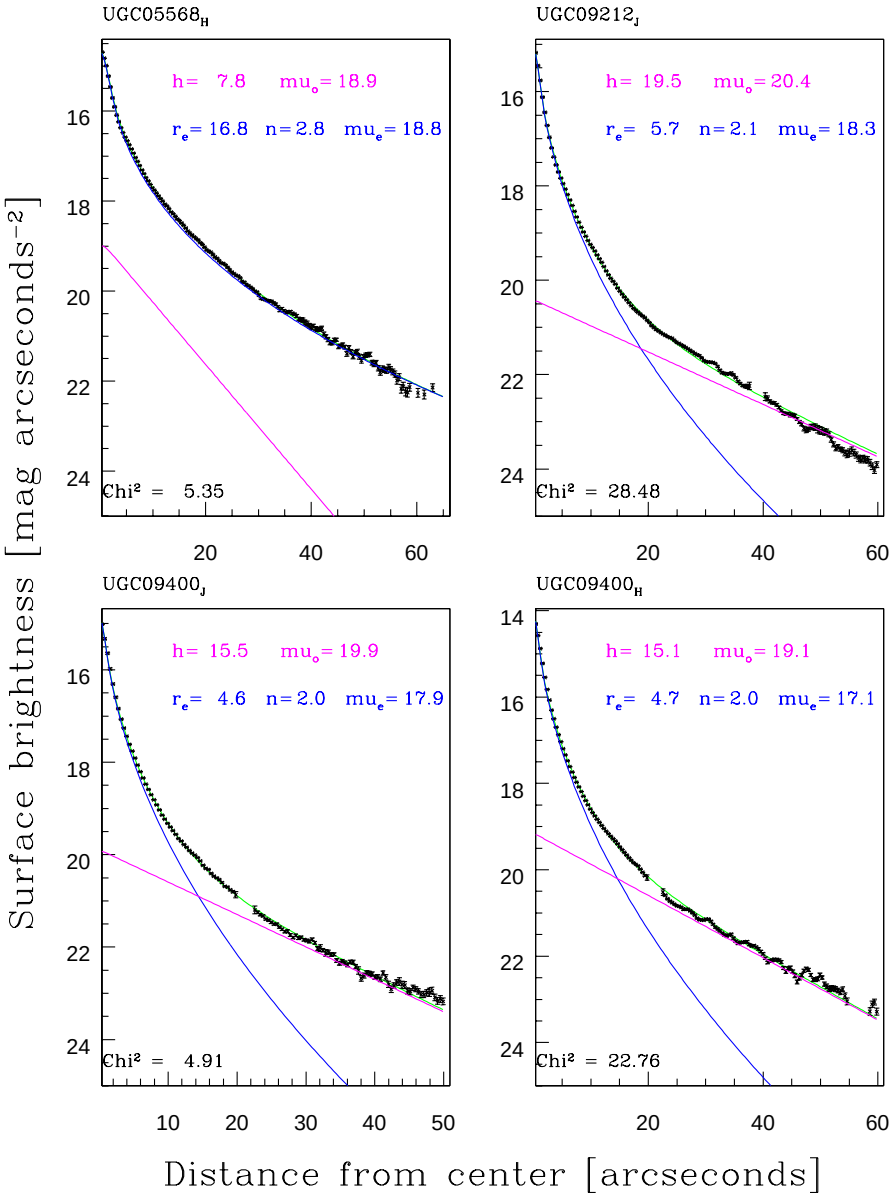
UGC05568H
h= 7.8 mu0= 18.9
re= 16.8 n= 2.8 mue= 18.8
Chi² = 5.35
UGC09212J
h= 19.5 mu0= 20.4
re= 5.7 n= 2.1 mue= 18.3
Chi² = 28.48
UGC09400J
h= 15.5 mu0= 19.9
re= 4.6 n= 2.0 mue= 17.9
Chi² = 4.91
UGC09400H
h= 15.1 mu0= 19.1
re= 4.7 n= 2.0 mue= 17.1
Chi² = 22.76
Surface brightness [mag arcseconds⁻²]
Distance from center [arcseconds]

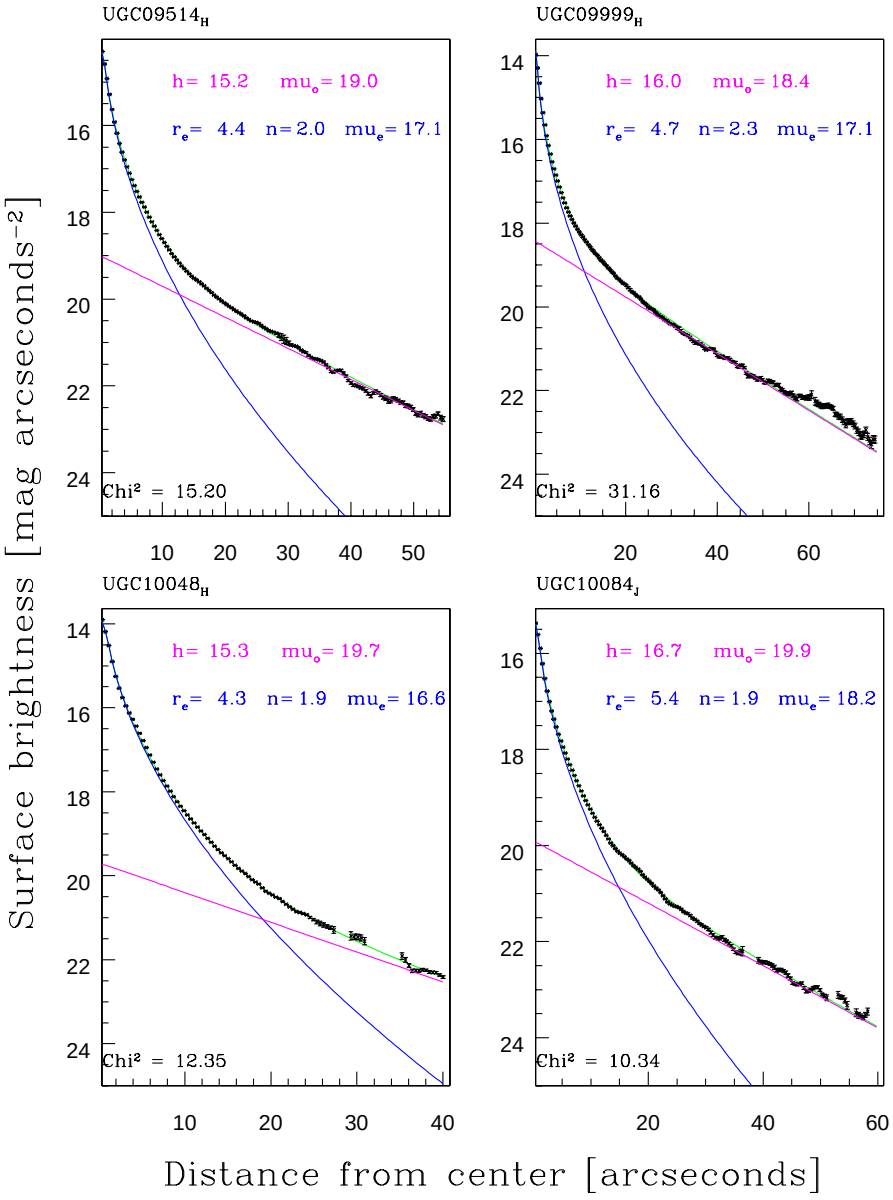
UGC09514H
h= 15.2 mu0= 19.0
re= 4.4 n= 2.0 mue= 17.1
Chi² = 15.20
UGC09999H
h= 16.0 mu0= 18.4
re= 4.7 n= 2.3 mue= 17.1
Chi² = 31.16
UGC10048H
h= 15.3 mu0= 19.7
re= 4.3 n= 1.9 mue= 16.6
Chi² = 12.35
UGC10084J
h= 16.7 mu0= 19.9
re= 5.4 n= 1.9 mue= 18.2
Chi² = 10.34
Surface brightness [mag arcseconds⁻²]
Distance from center [arcseconds]

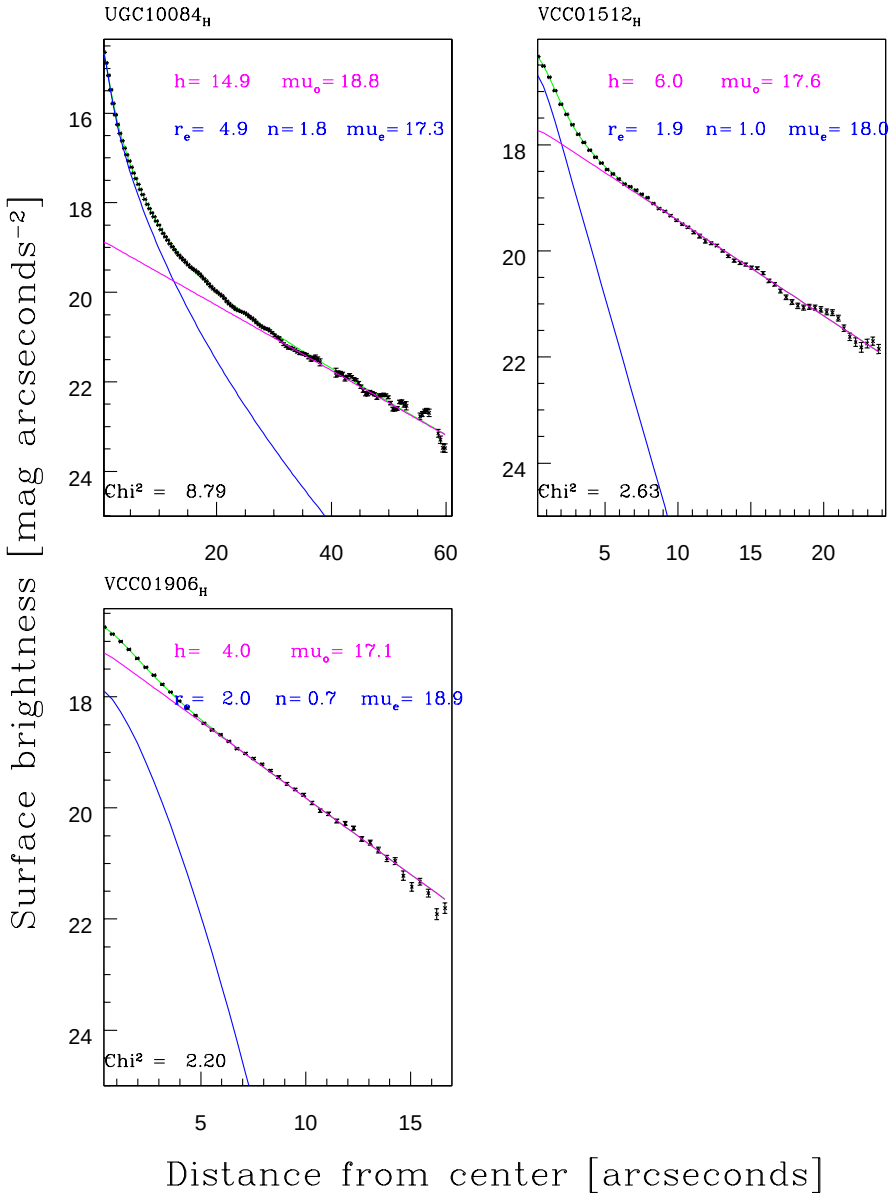
UGC10084H
h= 14.9 mu0= 18.8
re= 4.9 n= 1.8 mue= 17.3
Chi² = 8.79
VCC01512H
h= 6.0 mu0= 17.6
re= 1.9 n= 1.0 mue= 18.0
Chi² = 2.63
VCC01906H
h= 4.0 mu0= 17.1
re= 2.0 n= 0.7 mue= 18.9
Chi² = 2.20
Surface brightness [mag arcseconds⁻²]
Distance from center [arcseconds]

The Sersic index n is found to vary in our sample from 0.7 to 3.0, with a mean of 2.0 $\pm$ 0.6 (where the error indicates a standard deviation). The distribution of Sersic index n for our sample is shown in the left panels of Fig. 3.7, with OOPS galaxies shown in the bottom panel and the remainder of our sample shown in the top panel. The number of galaxies in each group are too low to draw a statistical result, but both groups show a similar distribution centered around $n = 2$. There are no OOPS galaxies with a purely exponential bulge, i.e. $n = 1.0$, and no galaxies in our entire sample with a pure $r^{1/4}$ law bulge. The ratio of bulge and disk scale lengths, r_e/h, varies in our sample from 0.15 to 2.1, with a mean of 0.41 $\pm$ 0.40 and a median of 0.29. The mean is weighted by UGC 5568, a bulge dominated galaxy. Excluding this galaxy gives a mean of 0.33 $\pm$ 0.12. The right panels of Fig. 3.7 show the distribution of r_e/h for our sample. Both subsamples show a smooth distribution around 0.3.

$(B/D)_{tot}$ ranges in our sample from 0.1 to 15.4, with a mean of 1.8 $\pm$ 3.1, and a median of 1.0. The mean is again offset by UGC 5568. Excluding this galaxy, our mean $(B/D)_{tot} = 1.1 \pm 0.7$. We use this value for literature comparisons below. On the other end of the spectrum are galaxies that are fully or nearly disk dominated throughout the entire galaxy: VCC 1906 and VCC1512. The distribution of $(B/D)_{tot}$ is shown in Fig. 3.8 for OOPS galaxies (bottom) and the remaining galaxies in our sample (top). We do not include UGC 5568 in the distribution for clarity of other galaxies. We find that $\sim 1/2$ of the galaxies of each group is disk dominated. There is no obvious difference in $(B/D)_{tot}$ for OOPS galaxies and other featureless S0 galaxies, except for a suggestion of a smaller range in $(B/D)_{tot}$ for the OOPS sample. The mean $(B/D)_{tot}$ for non-OOPS galaxies is 2.4 $\pm$ 4.0, although excluding UGC 5568 gives a mean of 1.2 $\pm$ 0.9. The OOPS galaxies have a mean of 1.0 $\pm$ 0.5.

We compare our derived mean values of best-fit parameters with those in the literature for other samples of S0 galaxies. We compare our results to four sources of bulge/disk decompositions of early type galaxies: Andredakis et al. (1995), Laurikainen et al. (2005), Noordermeer & van der Hulst (2007), and D'Onofrio (2001). There is a large overlap in luminosity of each sample with ours so that a luminosity

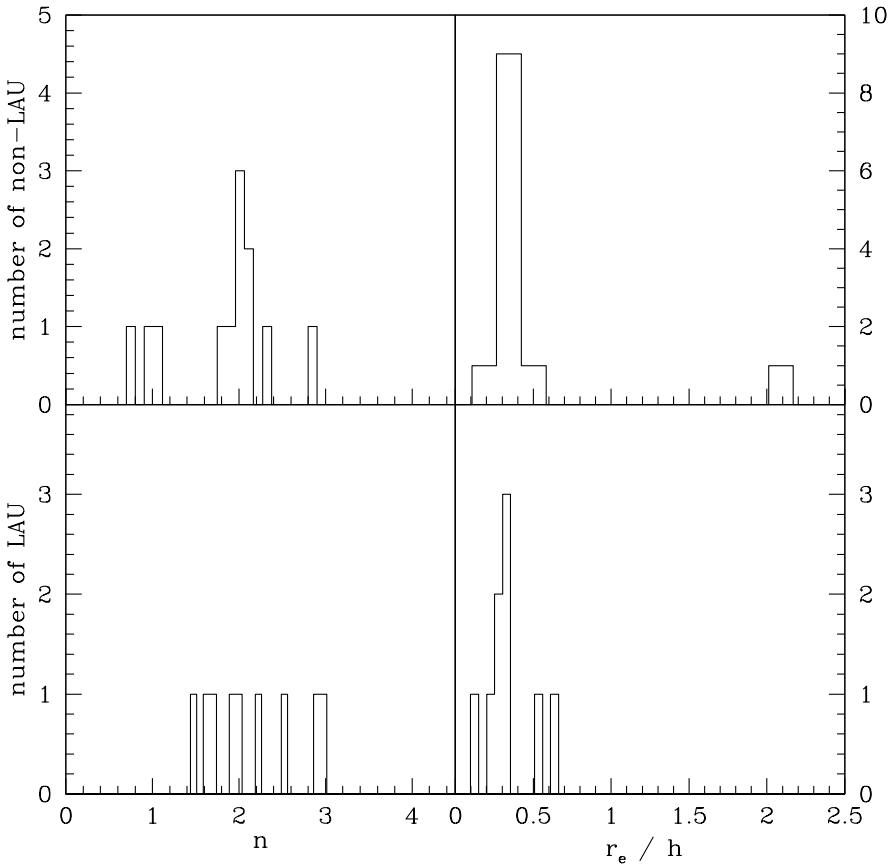

Figure 3.7 Left: The distribution of Sersic index, n for OOPS galaxies (bottom) and non-OOPS galaxies (top). Right: The distribution of scale ratios, r_e/h for OOPS galaxies (bottom) and non-OOPS galaxies (top).

difference between samples should not be responsible for any differences in parameters, but our sample does contain more of the lowest mass galaxies than other samples. Andredakis et al. (1995) and Laurikainen et al. (2005) have decompositions of galaxies in the K band, while D'Onofrio (2001) and Noordermeer & van der Hulst (2007) use the B band and R band, respectively.

The mean value of n for the 11 S0s in the Andredakis et al. (1995) sample is 3.7 $\pm$1.3, significantly higher than ours (2.0 $\pm$ 0.6). However, Laurikainen et al. (2005), D'Onofrio (2001), and Noordermeer & van der Hulst (2007) find n values more similar

to our values, with means of 2.1 ± 0.7, 3.4 ± 4.0, and 2.5 ± 1.1, respectively. The mean from D'Onofrio (2001) is heavily weighted by a few galaxies with large n (they did not set an upper limit at n=4). Our mean r_e/h (0.41 ± 0.40) matches that of Noordermeer & van der Hulst (2007) within errors, which found a mean of 0.51 ± 0.72, and is in between the r_e/h found by D'Onofrio (2001) of 1.6 ± 2.6 and Laurikainen et al. (2005) of 0.16 ± 0.12. Our sample appears to be, on average, more bulge dominated than the samples of Laurikainen et al. (2005), Andredakis et al. (1995), and Noordermeer & van der Hulst (2007), which find a mean B/D of 0.47 ± 0.37, 0.32 ± 0.12, and 0.59 ± 0.11, respectively. However, because our scatter is large, we have significant overlap with the B/D ratios of these samples. In summary, we believe our decomposition routine to produce similar parameters other works in the literature and we now move toward understanding the disk contribution to old ages in OOPS galaxies.

Fig. 3.9 shows a clear correlation of n with $(B/D)_{tot}$, such that higher n is found for larger $(B/D)_{tot}$. OOPS galaxies, in blue, and the remaining galaxies in our sample, in magenta, both show this trend, but it is stronger for the non-OOPS sample. These galaxies cover a wider range in $(B/D)_{tot}$. A least-squares fit to the OOPS sample reveals a slope of 0.3 ± 0.1 and to the remaining galaxies, 0.9 ± 0.3. The Pearson correlation coefficient is 0.7 and 0.9 and for the OOPS sample and non-OOPS sample, respectively. The difference in correlation of n with $(B/D)_{tot}$ is perhaps the clearest separation in physical parameters that we observe between OOPS galaxies and the remainder of our sample. The difference in observed n and $(B/D)_{tot}$ correlation of large and upturn galaxies from the rest of the sample may be suggesting different formation scenarios. Observations in the literature studying a range of Hubble types have also indicated a trend of n with B/D ratios (de Jong 1996b; Graham 2001; Andredakis et al. 1995). We show here that this holds for our sample of featureless S0 galaxies, as well. Comparing specific numbers, D'Onofrio (2001) find a slope of 0.5, in between the slope found for our 2 subsamples, and Graham (2001) find a Pearson correlation coefficient of 0.75, again in between the values of our 2 subsamples.

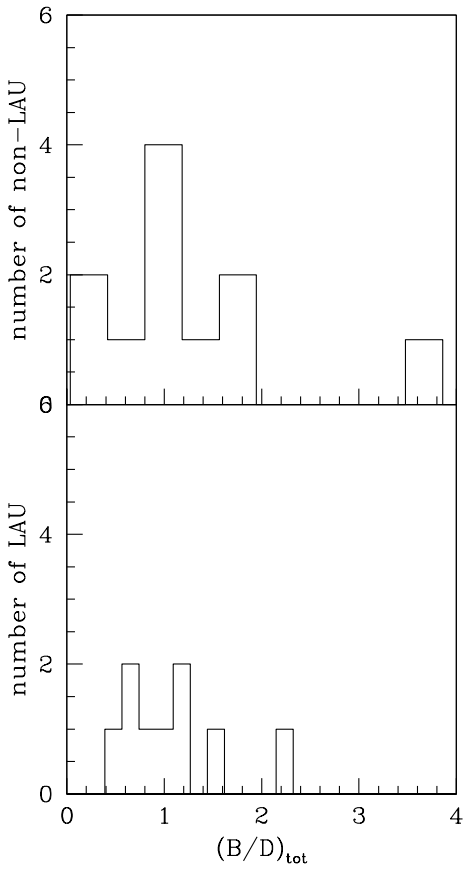

Figure 3.8 The distribution of the ratio of total bulge luminosity to disk luminosity, $(B/D)_{tot}$, is plotted. The top panel present galaxies that are not OOPS galaxies (excluding UGC 5568) and the bottom panel presents OOPS galaxies.

3.4.2 Radial Trends

The profile fits in Fig. 3.5 have indicated that the outer regions of OOPS galaxies are disk dominated. For a more quantitative analysis, we have calculated the ratio of bulge luminosity to disk luminosity for each radial bin, $(B/D)_{bin}$, for which we have stellar population information from § 2. We find that by the 4th radial bin, which coincides with $\sim 3.5\ R_e$ (this is a total, not sersic, effective radius), all OOPS galaxies have a mean light-weighted age for that bin greater than 7 Gyr, with most at their maximum age. To demonstrate the component contributing to the light at

that radius, we show the distribution $(B/D)_{bin4}$ in Fig. 3.10 for both OOPS galaxies (bottom) and non-OOPS galaxies (top). Because individual radial bins have a large range in B/D ratios, we plot the distribution in log space. In the non-OOPS sample, 2 galaxies, VCC 1512 and VCC 1906, have been excluded from this figure because their data does not extend to 3.5 R_e. Both of these galaxies are entirely disk dominated at the data limit. We find that at the radial range of the 4th bin, all but one OOPS galaxy, UGC 9321, is disk dominated (Log $(B/D)_{bin4} < 0$). In § 3.3.4, we discussed the decomposition for UGC 9321 and performed a profile fit excluding the nuclear region. For that decomposition, the 4th radial bin is disk dominated. Assuming the nuclear-excluded fit to be the better choice, we would then find that all OOPS galaxies are disk dominated by the 4th radial bin. Examining each radial bin of each OOPS galaxy, we do not find any radial regions in any galaxies that have a light-weighted age greater than 7 Gyr that are not disk dominated, except for UGC 9321. Thus, we can conclude that the old stellar populations of OOPS galaxies primarily belong to the disk component of these galaxies. Even the nuclear-excluded fit for UGC 9321 gives a bulge dominated light at radii where the age is $\sim$ 9 Gyr. This galaxy is an exception to the general trend observed. While the statistics are too low among the OOPS galaxies to draw any conclusions regarding the difference between these galaxies and the remainder of our sample, we find in Fig. 3.10 that both samples of galaxies are primarily disk dominated at radii around 3.5 R_e and see no obvious difference in the two distributions.

3.4.3 Relation to Radial Stellar Population Trends

Our major conclusion thus far is that the old regions of OOPS galaxies are disk dominated. We now wish to understand whether the radial trends in age are due solely to a transition from the bulge to disk dominated regions or whether there exists age gradients in disk or bulge components. In this effort, we examine the relation between radial stellar population trends and the relative contribution of the bulge and disk components. In Fig. 3.11 we plot the luminosity-weighted mean age, as blue circles,

versus radius. The galaxy colors have been averaged for each data point in various radial binning regions and then an age is calculated from each bin using the Bruzual & Charlot (2003) simple stellar population models. See § 2.6.2 for more details on age calculations. We also plot, using the right axis and red x's, the $(B/D)_{bin}$ for the same radial binning regions that the ages are calculated from. For visual ease, we have flipped the scale on the right axis so that the upper part of the plots designate a greater disk dominance. Each panel shows a separate OOPS galaxy. The error bars on $Log((B/D)_{bin})$ x's are due to sky subtraction and psf measurement errors, as described in § 3.3.3. Error bars are not shown for the age measurements when the derived age was close to 13.8 Gyr, or when the derived metallicity was close to 0.5 due to difficulties in calculating errors when the galaxy colors lie off the model age and metallicity grid (see § 2.6.2).

Some galaxies show that the average age and the disk contribution to the light are locked in step. For example, UGC 4916 shows a trend where the age becomes slightly older ($\sim$ 7 Gyr) just as the disk starts to dominate the light. Once fully disk dominated, the ages are at the maximum age for that galaxy. UGC 5182 shows a similar effect. On the other hand, other galaxies demonstrate that the ages and B/D ratios are out of sync. By the 3rd bin of UGC 10391 the light is already heavily dominated by the disk, but the age is still relatively young ($\sim$ 5 Gyr) compared to the age at the 4th radial bin. Similarly, VCC 1196 shows a large increase in age from the 2nd to 3rd radial bin ($\sim$ 8 Gyr) even though both the 2nd and 3rd bins are disk dominated. This seems to suggest that the old age is not uniform through the disk but the inner disk is younger. These results indicate that not only is the disk contributing to the large ages in the outer regions, but an age change within the disk is also contributing to the integrated radial age gradient. However, we are not able to discern whether there is an actual gradient in the disk rather than a discrete change.

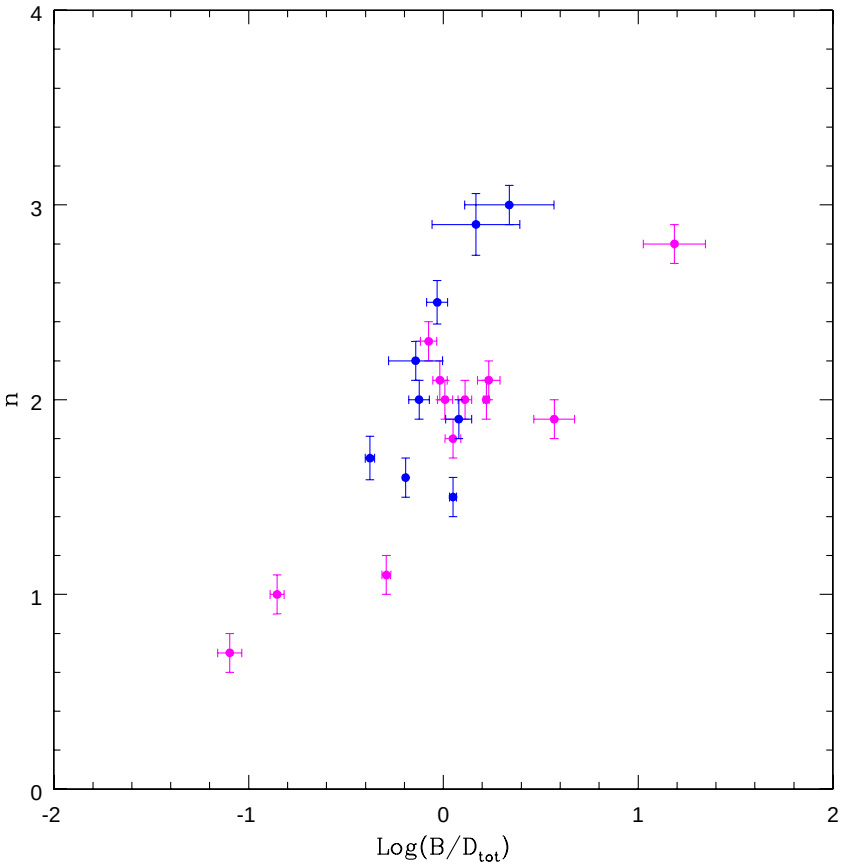

Figure 3.9 Log($(B/D)_{tot}$) plot against Sersic index, n for OOPS galaxies (blue) and the remaining galaxies in our sample (magenta). Error bars on n represent the formal errors from model fits added in quadrature to the shift in n from varying sky values and initial parameters. Error bars on $(B/D)_{tot}$ represent the shift in $(B/D)_{tot}$ from varying sky values and initial parameters, added in quadrature.

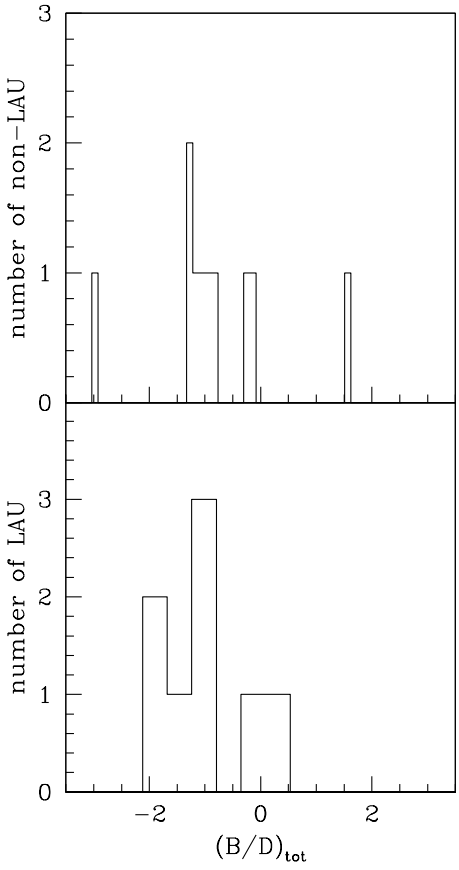

Figure 3.10 The distribution of the ratio of bulge luminosity to disk luminosity for the 4th radial bin (in Log $(B/D)_{bin4}$) is plotted. The top panel presents non-OOPS galaxies and the bottom panel presents OOPS galaxies.

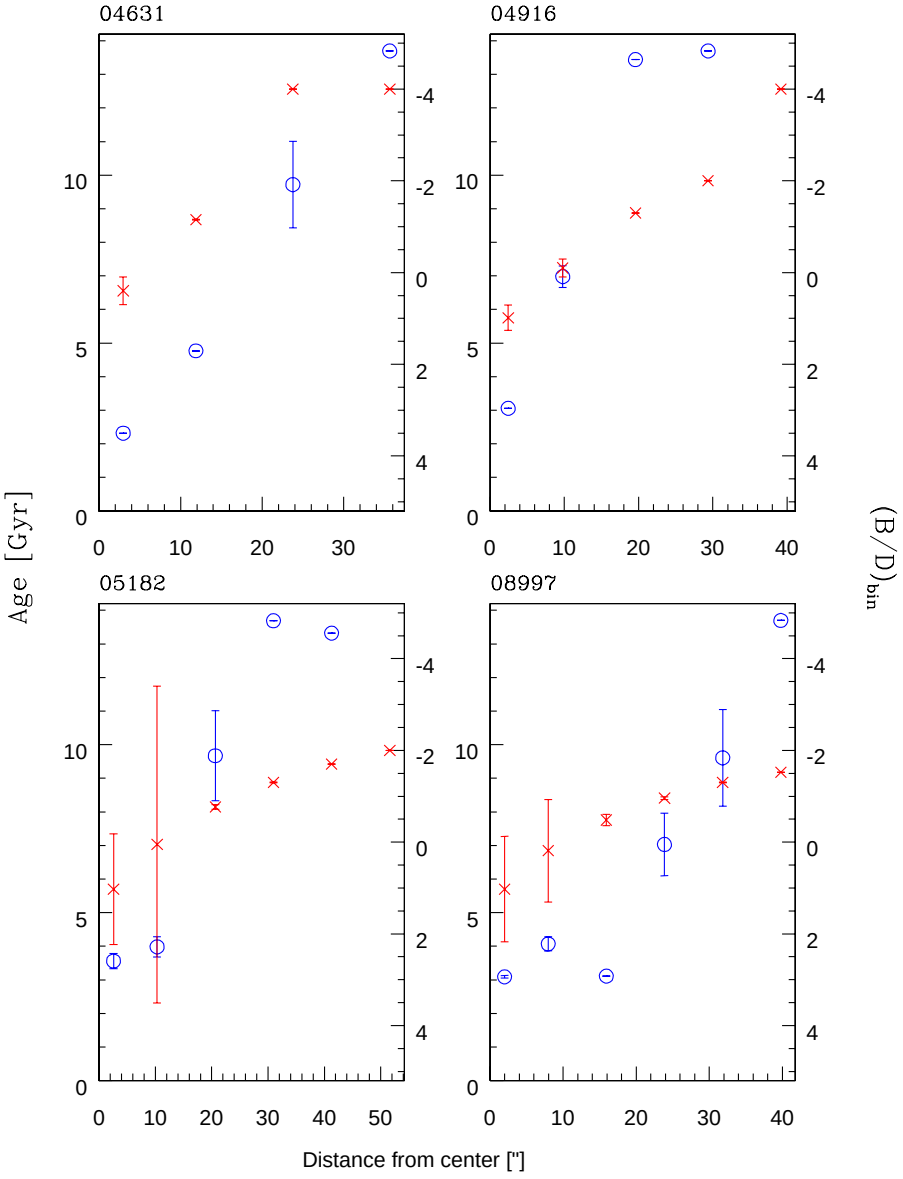

Figure 3.11 Radial trends in age and $Log((B/D)_{bin})$ are plotted. The left axis and blue circles denote the stellar population age. The right axis and red x's denote the $(B/D)_{bin}$. All parameters have been averaged for each radial bin. Error bars on $Log((B/D)_{bin})$ are due to sky subtraction and psf measurement errors.

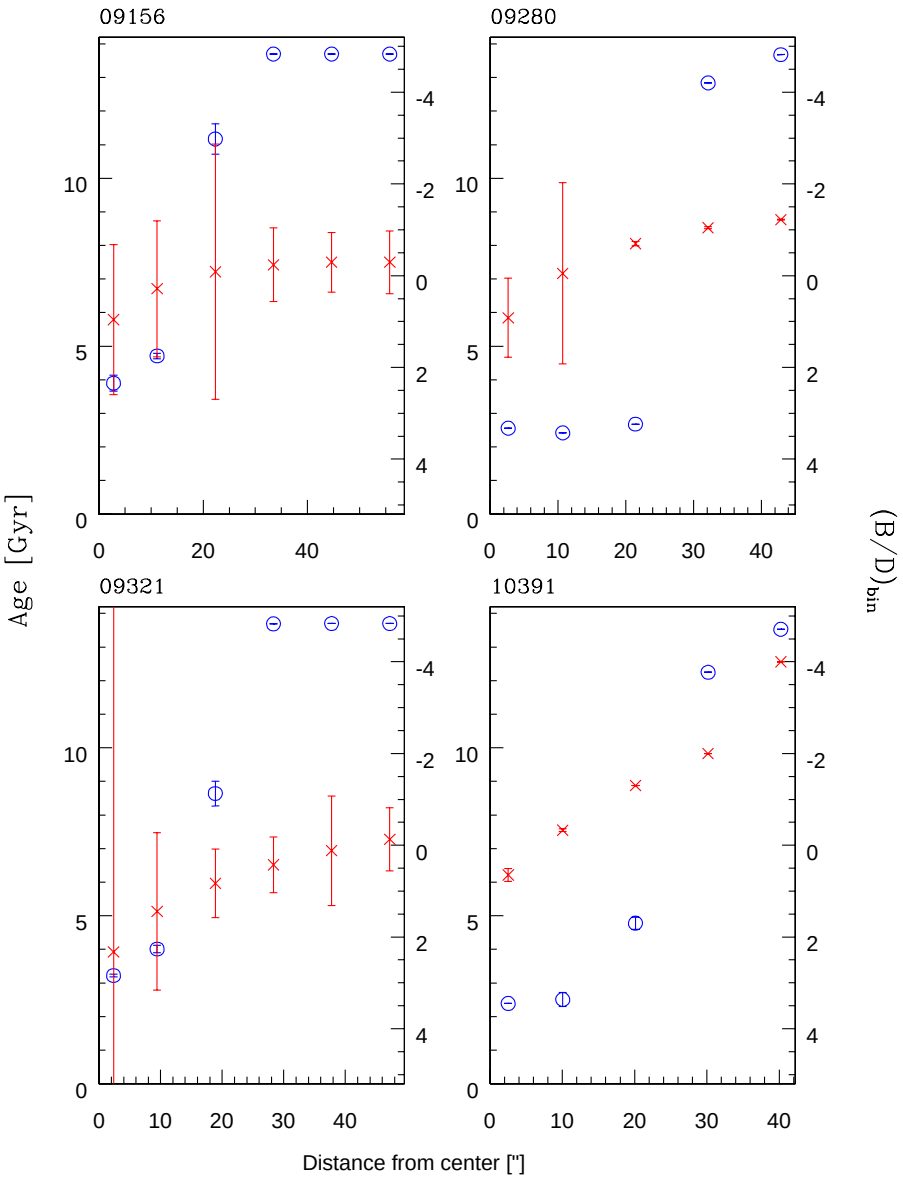
09156
09280
09321
10391
Age [Gyr]
(B/D)bin
Distance from center ["]

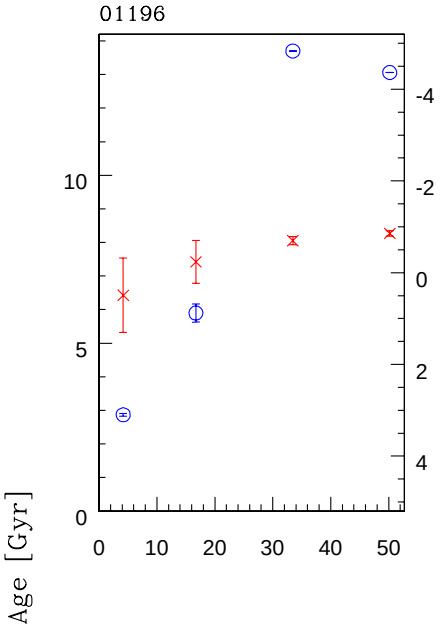
01196
Age [Gyr]
0
5
10
0
10
20
30
40
50
-4
-2
0
2
4
(B/D)bin
Distance from center ["]

3.5 Discussion

A significant result that we found in § 2 is a subsample of galaxies with large increases in light-weighted age from the center outward and significantly old outer regions (> 10 Gyr). These OOPS galaxies are found in primarily low density environments, with the exception of VCC 1196, which is the in the Virgo cluster. OOPS galaxies come in a variety of masses and concentrations. The main physical characteristic they have in common is the tendency to be featureless. In this paper, we aimed to determine if the outer regions of OOPS galaxies were disk dominated. We can conclude from our results that the old stellar populations of OOPS galaxies primarily belong to the disk component of these galaxies. In fact, except for UGC 9321, we find that all radial regions with a mean light-weighted age greater than 7 Gyr are disk dominated.

We have discussed potential observational and model dependent caveats for the result of old ages in the outer regions of OOPS galaxies in § 2. Assuming this result is robust, we explore tentative implications on galaxy evolution. In this aim, we raise two related questions: 1. Because stars are believed to form in the disk component (White & Rees 1978; Abadi et al. 2003), old ages in the disk imply that the disk formed long ago. How have the disks, which are fragile components, survived for so long? 2. Most disk galaxies show a decrease in light-weighted age with radius (Bell & de Jong 2000; MacArthur et al. 2004). What processes have created the reverse radial trend in OOPS galaxies?

Given uncertainties in NIR modeling it is difficult to set an absolute age on the formation of the disk, but it is clear that, for OOPS galaxies, the stars dominating the light in the outer regions formed long ago (possibly > 10 Gyr). Moderately old disks ($\sim$ 7 Gyr) have been predicted by theoretical models where the main infall phase precedes the onset of star formation (Ferguson & Clarke 2001). As well, Koo et al. (2005) find a few very red luminous disks at high redshift, implying that at z=1 not all massive disks are young and some old, massive S0s have already existed in the field.

For reference, stars formed at z=1 would be around 7 Gyr old at the present epoch. The presence of a disk component implies that no major, disk-destroying event has occurred since the formation of the dynamically fragile stellar disk; stellar disks are thought to be destroyed in merger of galaxies with a mass ratio $> 1/4$ (Steinmetz & Navarro 2002; Mihos & Hernquist 1996) while gas disks are shown to remain intact in gas rich major mergers (Hopkins et al. 2009). Thus, the very old ages of the outer regions of OOPS galaxies (possibly > 10 Gyr) places a constraint on models of hierarchical merging, requiring no major merger to have occurred for these galaxies in a very long time (since $z \sim 2$, using an age of 10 Gyr).

The positive age gradients observed in OOPS galaxies also offer clues to their formation. There are two ways to create an increase in light-weighted mean age with radius: (1) The dominant population (weighted by luminosity) in the disk is older than the dominant population in the bulge; or (2) Either the disk or the bulge has a positive gradient in light-weighted age. In § 3.4.3, we examined the relation between radial trends in age and radial trends in the B/D ratios, $(B/D)_{bin}$. Our results suggest that a transition from bulge dominated light to disk dominated light alone cannot explain the observed trends in age. The cause of radial age trends in OOPS galaxies is likely a complicated picture involving both a transition from bulge to disk light and a light-weighted age change in the disk component.

In order for the bulge (or the population dominating the light in the bulge) to have formed after the disk, the bulge would need to be created without either destroying the fragile disk or adding star formation to the disk. Internal secular evolution, as a way to build a bulge after the formation of the disk, has gained popularity. Internal secular evolution in gaseous galaxies is predicted to bring about SF in a centralized disk. While internal secular evolution may be contributing to a small percentage of the mass of the bulges and to the young light-weighted ages in the central regions of OOPS galaxies, other processes are likely at work to form the large bulges of some OPPS galaxies (internal secular evolution can reasonably produce a bulge with a B/D of 0.1) (Kormendy & Kennicutt 2004) and suppress the star formation in the disks.

An alternative explanation for young bulge ages is the formation of the bulge through minor accretion (external secular evolution). Galaxy encounters have been shown to enhance central star formation (Keel et al. 1985) and the observations of Kannappan et al. (2004) suggest external drivers are at play in bulge growth. The numerical simulations of Scannapieco & Tissera (2003); Eliche-Moral et al. (2005); Weinzirl et al. (2009) describe the growth of bulges following disk formation via satellite accretion. These models show an increase in both B/D and n of the bulge after accretion. We have found, in agreement with observations in the literature (de Jong 1996b; Graham 2001; Andredakis et al. 1995) a trend of n with B/D ratios such that higher n is found for larger B/D ratios for all galaxies in our sample. Interestingly, OOPS galaxies appear to have a different slope in n versus B/D, which may be indicating different merger histories for these galaxies.

A positive age gradient in the disk can be due to either the original formation of the disk or to a later event that transformed the galaxy into an S0. Several theories of S0 formation through external gas removal processes, such as theories of ram pressure stripping (Kawata & Mulchaey 2008; Kronberger et al. 2008; Quilis et al. 2000) and strangulation (Kawata & Mulchaey 2008), predict a trend of increasing light-weighted age with radius. Alternatively, a positive age gradient has been predicted in simulations of the dissipational collapse of gas embedded in a spherical dark matter halo by Roškar et al. (2008). After a particular radius, Roškar et al. (2008) finds a decrease in mean stellar age in his model disk galaxy.

3.6 Conclusion

This study focuses on the development of a reliable set of surface brightness profile decompositions based on a subsample of galaxies from § 2. We have performed galactic component decompositions of a sample of 22 S0 galaxies using a generalized sersic component for the 'bulge' and an exponential profile for the 'disk'. Our main goal was to understand whether the old outer regions of OOPS galaxies are disk or bulge

dominated.

For all galaxies in our sample, we derive a mean n of 2.0 $\pm$ 0.6, a mean ratio of bulge and disk scale lengths, r_e/h, of 0.41 $\pm$ 0.40, and a mean $(B/D)_{tot}$ of 1.8 $\pm$ 3.1. We find a correlation between n and $(B/D)_{tot}$ such that galaxies with larger n are more bulge dominated.

We have found that the old stellar populations of OOPS galaxies primarily belong to the disk component of these galaxies. In fact, except for UGC 9321, we find that all radial regions with a mean light-weighted age greater than 7 Gyr are disk dominated. The ages of the outer disks of OOPS galaxies place a constraint on models of hierarchical merging, requiring no major merger to have occurred for these galaxies in a very long time (since z $\sim$ 2, using an age of 10 Gyr).

This study was partially funded by NSF grant AST 04-06443 to the University of North Carolina. L.C. acknowledges the support of the Linda Dykstra Science Dissertation Fellowship and S.C. acknowledges the support of NSERC through Discovery grant.

Chapter 4

Discussion

We present optical (SDSS g and r) and near-IR (H and/or J) surface photometry for a sample of 59 S0 galaxies covering a range in stellar mass, light concentration, and environmental density. Radial age and metallicity gradients out to at least 5 effective radii are derived from comparison of the observed g-r and r-H (and/or r-J) colors to stellar population models. Galactic component decompositions are performed for a sub-sample of the 22 featureless S0 galaxies from the main sample. The decomposition uses a generalized Sersic component for the bulge and an exponential profile for the disk.

We find a mean central light-weighted age of $\sim$3 Gyr and central metallicity of [Z/H]$\sim$0.5 dex for all galaxies in our sample. Radial age trends are found to be heterogeneous: an increase in age with radius is found for 41% of our sample, a decrease for 17%, and little change for 42%. For most of the galaxies in our sample we find large negative metallicity gradients with an average of Δ[Z/H]/Δlog(r) = -0.5. In virtually all of the galaxy sample a negative metallicity gradient is found with a mean of Δ[Z/H]/Δlog(r) = -0.5.

We find that mean age correlates with both mass and concentration; for all radii, galaxies with both lower mass and lower concentration have, on average, younger ages than other galaxies in our sample. The strength of the metallicity gradient is not found to correlate with the global parameters of the galaxies in our sample.

For 20% of our sample, the outer regions are significantly old (> 10 Gyr) and there is a substantial increase in light-weighted age from the inner to the outer region of the galaxy. These galaxies, which we refer to as old outer population S0 (OOPS) galaxies, are found in a range of environments, masses, and concentrations covered by our sample, but seem to be rarer in galaxies with both low mass and low concentration. None of these galaxies are found to contain nascent spiral structure and many are entirely featureless in ground based images.

The focus of our surface brightness profile decompositions is to understand whether the old regions of OOPS galaxies are disk or bulge dominated. We have found that the old stellar populations of OOPS galaxies primarily belong to the disk component of these galaxies. In fact, except for one galaxy, we find that all radial regions of OOPS galaxies with a mean light-weighted age greater than 7 Gyr are disk dominated.

From decompositions of the sub-sample of 22 S0 galaxies, we derive a mean Sersic n of 2.0 $\pm$ 0.6, a mean ratio of bulge and disk scale lengths, r_e/h, of 0.41 $\pm$ 0.40, and a mean $(B/D)_{tot}$ of 1.8 $\pm$ 3.1. We find a correlation between n and $(B/D)_{tot}$ such that galaxies with larger n are more bulge dominated.

S0 galaxies display a wide variety of age trends, allowing for a range in formation mechanisms. By studying the galaxies' trends in stellar populations with radii and with their global properties and analyzing the component contributing to the majority of the light, we uncover important clues toward the main physical drivers governing the formation and evolution of S0s. Our main interpretations are the following.

A principal result of our study is that low mass, low concentration S0 galaxies have younger ages at all radii than S0s with high mass and/or concentration. Age/mass correlations in the central regions of galaxies are predicted in bulge formation scenarios of both a merger origin and a secular evolution (i.e. in situ bulge growth) origin. Observations supporting bulge growth through internal and external secular evolution have been noted in recent studies of late type spiral galaxies (Courteau et al. 1996; Ellis et al. 2001; Combes 2000; Kormendy & Kennicutt 2004; Kannappan et al. 2004; Barway et al. 2007). A small bulge, such as that in low mass and low concentration

galaxies, is more likely to contain associated star formation from secular evolution, even if some of the mass has been built up previously (Ellis et al. 2001). The merging scenario provides an alternative explanation of the age trend with mass and concentration. Recent semi-analytic modeling in hierarchical merging, containing enhanced feedback processes such as AGN, produce more extended SFHs in less massive galaxies, leading to positive correlations of mass with average age. (Cole et al. 1994; Bower et al. 2006; De Lucia et al. 2006; Croton et al. 2006).

Bedregal et al. (2008) has studied the central regions of S0 galaxies through analysis of [α/Fe]. Their results indicate that, for central regions at least, different star formation histories are responsible for the difference in mean ages. They find their results to be consistent with a scenario where faint S0s are descendants of spiral galaxies which have lost or exhausted their gas, while bright systems have star formation histories that resemble those of normal ellipticals. This dichotomy in S0 formation has been presented elsewhere in the literature (Jorgensen & Franx 1994; Mehlert et al. 2003; Barway et al. 2007). Our result of low mass and low concentration galaxies being younger on average than other galaxies suggests an extension to include concentration as a parameter in the dichotomy. The large B/D of S0 galaxies compared to spirals has been a concern for theories describing the transformation from spiral to S0 galaxies (Dressler 1980). However, if only low concentration S0 galaxies take this evolutionary path, this concern is relieved.

To understand the implications of OOPS galaxies on galaxy evolution, we have raised two questions: (1) How have the old disks, which are fragile components, survived for so long? (2) What processes have created the reverse radial trend in OOPS galaxies?

Because the existence of a stellar disk requires no disk-destroying mergers to have occurred since their formation, the very old ages of the outer regions of OOPS galaxies (possibly $>$ 10 Gyr) place a constraint on models of hierarchical merging, requiring no major merger to have occurred for these galaxies in a very long time (since z $\sim$ 2, using an age of 10 Gyr). Weinzirl et al. (2009) also find that spirals with low present

day B/D can by accounted for in their hierarchical models by requiring they have not undergone a major merger since the formation of the stellar disk. However, the preservation of gas disk in gas-rich major mergers (Hopkins et al. 2009), may account for this. Although the gas disk may not be destroyed in a major merger, the stars are predicted to be redistributed in the bulge through violent relaxation (Hopkins et al. 2009) so gas rich mergers will not remove our requirement of no major merger since z = 2. Alternately, old stars may have somehow been redistributed into the outer regions, while they actually originated elsewhere. However, because the integrated light is heavily weighted toward young SPs, the old light-weighted ages in the outskirts of OOPS galaxies imply that virtually no young stars exist in this region. This would require a massive migration of only old stars, not a reasonable scenario.

Internal secular evolution may play a role in creating the young bulges in OOPS galaxies, but other processes are required to explain the suppression of star formation in the disk. An alternative explanation is the formation of the bulge through minor accretion. Models of Hernquist & Mihos (1995) show that even a 10 to 1 merger can drive up to 50 % of the primary galaxy's gas into its center. Not only will this help to build up a young bulge, but it will suppress star formation in the disk. Observations in the literature support externally driven bulge growth (Kannappan et al. 2004) and models of galaxy encounters demonstrate enhanced central star formation (Keel et al. 1985). The numerical simulations of Scannapieco & Tissera (2003); Eliche-Moral et al. (2005); Weinzirl et al. (2009) describe the growth of bulges following disk formation via satellite accretion (i.e. minor mergers that do not destroy the stellar disk). These models shows an increase in both B/D and n of the bulge after accretion, which do match our results of a trend of n with B/D ratios.

In addition to an older disk in OOPS galaxies, it seems that a change in light-weighted age in the disk component is necessary to explain our results. A radial age increase in the disk can be due to either the original formation of the disk or to a later event that transformed the galaxy into an S0. Proposed theories of S0 formation through external gas removal processes (Kawata & Mulchaey 2008; Kronberger et al.

2008; Quilis et al. 2000) predict that the physical processes acting on the galaxy will strip the galaxy from the outside-in as it is more easily stripped at a larger radius. The resultant galaxy will have a lower light-weighted age inside the truncation radius than outside. Additionally, enhancement of star formation from several gas removal processes is expected in the central regions, again providing an increase in age with radius. The events that are expected to bring about this age difference, however, are also expected to be short-lived with a timescale around 500 Myr (Kronberger et al. 2008). To create the large difference in age we observe from the center out, the star formation must be sustained in the inner regions for a very long time.

Our results indicate a continual age trend that reaches the far outer regions of the galaxy. However, this difference seems to be a combination of a bulge younger than the disk and a disk that has a younger inner region. We are not able to determine whether a continuous gradient or a discrete age change exists in the disk. The existence of a discrete change in age in the disk would support gas truncation processes in the OOPS's past. However, even if a gradient is found, it is possible that the S0s that we observe to have large upturns have undergone multiple gas removal events. In fact, Kronberger et al. (2008) find that only 13% of gas is removed in their simulations of a single ram pressure stripping event.

The age increase in OOPS disks may instead be due to the original formation of the disk. Positive age gradients in disks are not exclusive to S0 galaxies. Taylor et al. (2005) has found that the outer regions of some late type spiral galaxies are redder and the inner regions are bluer than other galaxies in his sample and suggests that this could be an indicator of outside-in formation, with a relatively high amount of recent star formation in the inner regions and low amount of recent star formation in the outer regions. A positive age gradient has been predicted in simulations of the dissipational collapse of gas embedded in a spherical dark matter halo by Roškar et al. (2008). After a particular radius, Roškar et al. (2008) finds a decrease in mean stellar age in his model disk galaxy. However, in this scenario, we would expect to see a break in light-weighted age with radius. As discussed above, we are not yet able to

determine the existence of a discrete change in age with radius.

Chapter 5

Future Work

There remains additional research that could contribute to this work. Using the present data set, opportunities exist for further exploration of galactic component decompositions of old outer region S0 galaxies. Looking toward additional data, we can obtain clarification in existing results, such as trends with mass and concentration, as well as move the project toward new and interesting directions. A description of these research avenues follows.

With the present data set, we can extend our decompositions for all 22 galaxies analyzed thus far to the optical g and r bands. Using the g and/or r band, in combination with the H band will enable us to understand the variation in decomposition with wavelength. Ideally, we would like to map the color of the disk and the bulge to begin to understand the age trends of the disk and bulge as separate components. Using colors provided by simple stellar population models, we can model the age of integrated light from two-component stellar populations to mimic the bulge and disk contributions that we have found. This will help clarify whether our age trends can be matched by 2 components of a single age each or if a gradient in one of the components is necessary.

It would also be interesting to understand the relation of mass and concentration with the decomposition parameters. This might help us to better understand the formation of low mass, low concentration galaxies. Also, examining the decompositions

of high mass OOPSs and comparing them to low mass OOPSs may tell us whether there is a uniform formation mechanism for OOPS galaxies or if they are spurious cases.

There are several areas where a larger or varied data set would be useful. In some cases, this data is readily attainable. We have explored whether low-mass, low-concentration S0 galaxies seemed to form a distinct class of galaxies as opposed to there being a continuous trend in mass and concentration with age for all galaxies. Our results suggest that the inner ages appear to have a trend in both mass and concentration, while the outer ages suggest two distinct groups, but a larger galaxy sample is necessary to make concrete conclusions. Studies of a larger sample of S0 galaxies, particularly those with low mass and low concentration, will enable a decisive test of whether low mass low concentration S0s constitute a fundamentally separate class of S0 formation, or whether they are simply extreme examples of a basic correlation between mass/concentration and star formation history in a more unified evolutionary picture for S0 galaxies. To increase the sample, we can use archival imaging data from SDSS for the optical and UKIDSS for the near-IR. Searching the large data bases for low mass and low concentration S0 galaxies may turn up a large number of galaxies that can be studied immediately, with no new observations required.

Photometry at different wavelengths will provide information on the star formation histories of our galaxies. For example, because our analysis is based on luminosity weighted mean ages, the inner regions may consist of a sprinkling of very young stars with an underlying old population, as opposed to a consistently young population. This could be resolved through a multi-wavelength analysis in the central regions. I have already obtained deep U-band photometry for 15 galaxies in our sample from the SOAR telescope. This data, especially if combined with near and far UV data from GALEX archives, will provide a longer baseline and bandpasses sensitive to recent star formation that will hopefully separate star formation histories in the central regions of the galaxy.

An interesting avenue to explore that would require additional observations is a

spectroscopic analysis of S0 galaxies. Deep spectroscopy of S0 galaxies will allow a useful check on our results as well as offer additional information. Spectroscopy will provide a clearer discrimination in age and metallicity, which is beneficial in separating subtle age differences. As well, we will be able to study abundance ratios, such as [α/Fe], in order to better separate star formation histories. Unfortunately, to reach the outer regions of the galaxy, we would need to view edge-on S0 galaxies and could not use the same sample that we use here. Nevertheless, performing a similar analysis of stellar population trends in a sample of edge on S0 galaxies using deep spectroscopic analysis will be highly beneficial.

REFERENCES

Abadi, M. G., Navarro, J. F., Steinmetz, M., & Eke, V. R. 2003, ApJ, 591, 499

Andredakis, Y. C., Peletier, R. F., & Balcells, M. 1995, MNRAS, 275, 874

Athanassoula, E. 2003, MNRAS, 341, 1179

Balcells, M., Graham, A. W., Domínguez-Palmero, L., & Peletier, R. F. 2003, ApJ, 582, L79

Balcells, M., Graham, A. W., & Peletier, R. F. 2007, ApJ, 665, 1104

Balcells, M. & Peletier, R. F. 1994, AJ, 107, 135

Barnes, J. E. 2002, MNRAS, 333, 481

Barnes, J. E. & Hernquist, L. E. 1991, ApJ, 370, L65

Barr, J. M., Bedregal, A. G., Aragón-Salamanca, A., Merrifield, M. R., & Bamford, S. P. 2007, A&A, 470, 173

Barway, S., Kembhavi, A., Wadadekar, Y., Ravikumar, C. D., & Mayya, Y. D. 2007, ApJ, 661, L37

Bedregal, A. G., Aragón-Salamanca, A., Merrifield, M. R., & Cardiel, N. 2008, MNRAS, 387, 660

Bell, E. F. & de Jong, R. S. 2000, MNRAS, 312, 497

Bell, E. F., McIntosh, D. H., Katz, N., & Weinberg, M. D. 2003, ApJS, 149, 289

Bell, E. F., Wolf, C., Meisenheimer, K., Rix, H.-W., Borch, A., Dye, S., Kleinheinrich, M., Wisotzki, L., & McIntosh, D. H. 2004, ApJ, 608, 752

Benedict, G. F., Howell, D. A., Jørgensen, I., Kenney, J. D. P., & Smith, B. J. 2002, AJ, 123, 1411

Bertelli, G., Girardi, L., Marigo, P., & Nasi, E. 2008, A&A, 484, 815

Boselli, A., Boissier, S., Cortese, L., & Gavazzi, G. 2008, ApJ, 674, 742

Bothun, G. D. & Gregg, M. D. 1990, ApJ, 350, 73

Bower, R. G., Benson, A. J., Malbon, R., Helly, J. C., Frenk, C. S., Baugh, C. M., Cole, S., & Lacey, C. G. 2006, MNRAS, 370, 645

Bower, R. G., Lucey, J. R., & Ellis, R. S. 1992, MNRAS, 254, 601

Bruzual, G. & Charlot, S. 2003, MNRAS, 344, 1000

Buta, R., Treuthardt, P. M., Byrd, G. G., & Crocker, D. A. 2000, AJ, 120, 1289

Butcher, H. & Oemler, Jr., A. 1978, ApJ, 226, 559

Byrd, G. & Valtonen, M. 1990, ApJ, 350, 89

Caldwell, N. 1983, ApJ, 268, 90

Caldwell, N., Rose, J. A., & Concannon, K. D. 2003, AJ, 125, 2891

Carollo, C. M. 1999, ApJ, 523, 566

Charlot, S. & Bruzual, G. 2009, in preparation

Cole, S., Aragon-Salamanca, A., Frenk, C. S., Navarro, J. F., & Zepf, S. E. 1994, MNRAS, 271, 781

Combes, F. 2000, in Astronomical Society of the Pacific Conference Series, Vol. 197, Dynamics of Galaxies: from the Early Universe to the Present, ed. F. Combes, G. A. Mamon, & V. Charmandaris, 15–+

Conroy, C., White, M., & Gunn, J. E. 2009, ArXiv e-prints

Cooper, M. C., Tremonti, C. A., Newman, J. A., & Zabludoff, A. I. 2008, MNRAS, 390, 245

Courteau, S. 1996, ApJS, 103, 363

Courteau, S., de Jong, R. S., & Broeils, A. H. 1996, ApJ, 457, L73+

Croton, D. J., Springel, V., White, S. D. M., De Lucia, G., Frenk, C. S., Gao, L., Jenkins, A., Kauffmann, G., Navarro, J. F., & Yoshida, N. 2006, MNRAS, 365, 11

Dalcanton, J. J., Spergel, D. N., & Summers, F. J. 1997, ApJ, 482, 659

de Jong, R. S. 1996a, A&AS, 118, 557

—. 1996b, A&A, 313, 45

de Jong, R. S. & Davies, R. L. 1997, MNRAS, 285, L1

De Lucia, G., Springel, V., White, S. D. M., Croton, D., & Kauffmann, G. 2006, MNRAS, 366, 499

de Vaucouleurs, G. 1948, Annales d'Astrophysique, 11, 247

D'Onofrio, M. 2001, MNRAS, 326, 1517

Dressler, A. 1980, ApJ, 236, 351

Dressler, A. & Gunn, J. E. 1983, ApJ, 270, 7

Eliche-Moral, M. C., Balcells, M., Aguerri, J. A. L., & Gonzalez-Garcia, A. C. 2005, ArXiv Astrophysics e-prints

Ellis, R. S., Abraham, R. G., & Dickinson, M. 2001, ApJ, 551, 111

Eminian, C., Kauffmann, G., Charlot, S., Wild, V., Bruzual, G., Rettura, A., & Loveday, J. 2008, MNRAS, 384, 930

Erwin, P., Beckman, J. E., & Pohlen, M. 2005, ApJ, 626, L81

Falco, E. E., Kurtz, M. J., Geller, M. J., Huchra, J. P., Peters, J., Berlind, P., Mink, D. J., Tokarz, S. P., & Elwell, B. 1999, PASP, 111, 438

Fall, S. M. & Efstathiou, G. 1980, MNRAS, 193, 189

Ferguson, A. M. N. & Clarke, C. J. 2001, MNRAS, 325, 781

Fioc, M. & Rocca-Volmerange, B. 1997, A&A, 326, 950

Fisher, D., Franx, M., & Illingworth, G. 1996, ApJ, 459, 110

Fisher, D. B. & Drory, N. 2008, AJ, 136, 773

Freeman, K. C. 1970, ApJ, 160, 811

Fritze v. Alvensleben, U. 2004, in Astrophysics and Space Science Library, Vol. 319, Penetrating Bars Through Masks of Cosmic Dust, ed. D. L. Block, I. Puerari, K. C. Freeman, R. Groess, & E. K. Block , 81–+

Garnett, D. R. 2002, ApJ, 581, 1019

Giuricin, G., Marinoni, C., Ceriani, L., & Pisani, A. 2000, ApJ, 543, 178

Graham, A. W. 2001, AJ, 121, 820

Griffiths, R. E., Casertano, S., Ratnatunga, K. U., Neuschaefer, L. W., Ellis, R. S., Gilmore, G. F., Glazebrook, K., Santiago, B., Huchra, J. P., Windhorst, R. A., Pascarelle, S. M., Green, R. F., Illingworth, G. D., Koo, D. C., & Tyson, A. J. 1994, ApJ, 435, L19

Haynes, M. P. & Giovanelli, R. 1984, AJ, 89, 758

Hernquist, L. & Mihos, J. C. 1995, ApJ, 448, 41

Hinshaw, G., Weiland, J. L., Hill, R. S., Odegard, N., Larson, D., Bennett, C. L., Dunkley, J., Gold, B., Greason, M. R., Jarosik, N., Komatsu, E., Nolta, M. R., Page, L., Spergel, D. N., Wollack, E., Halpern, M., Kogut, A., Limon, M., Meyer, S. S., Tucker, G. S., & Wright, E. L. 2009, ApJS, 180, 225

Hogg, D. W., Blanton, M. R., Eisenstein, D. J., Gunn, J. E., Schlegel, D. J., Zehavi, I., Bahcall, N. A., Brinkmann, J., Csabai, I., Schneider, D. P., Weinberg, D. H., & York, D. G. 2003, ApJ, 585, L5

Hopkins, P. F., Somerville, R. S., Cox, T. J., Hernquist, L., Jogee, S., Kereš, D., Ma, C.-P., Robertson, B., & Stewart, K. 2009, MNRAS, 397, 802

Huang, S. & Gu, Q.-S. 2009, MNRAS, 398, 1651

Hubble, E. & Humason, M. L. 1931, ApJ, 74, 43

Hubble, E. P. 1936, Realm of the Nebulae, ed. E. P. Hubble

Icke, V. 1985, A&A, 144, 115

Jogee, S., Shlosman, I., Laine, S., Englmaier, P., Knapen, J. H., Scoville, N., & Wilson, C. D. 2002, ApJ, 575, 156

Jorgensen, I. & Franx, M. 1994, ApJ, 433, 553

Jorgensen, I., Franx, M., & Kjaergaard, P. 1996, MNRAS, 280, 167

Kannappan, S., Guie, J., & Baker, A. 2009a, AJ, submitted

Kannappan, S. J. & Gawiser, E. 2007, ApJ, 657, L5

Kannappan, S. J., Guie, J. M., & Baker, A. J. 2009b, AJ, 138, 579

Kannappan, S. J., Jansen, R. A., & Barton, E. J. 2004, AJ, 127, 1371

Kauffmann, G., Heckman, T. M., White, S. D. M., Charlot, S., Tremonti, C., Brinchmann, J., Bruzual, G., Peng, E. W., Seibert, M., Bernardi, M., Blanton, M.,

Brinkmann, J., Castander, F., Csábai, I., Fukugita, M., Ivezic, Z., Munn, J. A., Nichol, R. C., Padmanabhan, N., Thakar, A. R., Weinberg, D. H., & York, D. 2003, MNRAS, 341, 33

Kawata, D. & Mulchaey, J. S. 2008, ApJ, 672, L103

Keel, W. C., Kennicutt, Jr., R. C., Hummel, E., & van der Hulst, J. M. 1985, AJ, 90, 708

Kenney, J. D. P., Tal, T., Crowl, H. H., Feldmeier, J., & Jacoby, G. H. 2008, ApJ, 687, L69

Kent, S. M. 1985, ApJS, 59, 115

Kobayashi, C. 2004, MNRAS, 347, 740

Kochanek, C. S., Falco, E. E., Impey, C. D., Lehár, J., McLeod, B. A., Rix, H.-W., Keeton, C. R., Muñoz, J. A., & Peng, C. Y. 2000, ApJ, 543, 131

Koo, D. C., Simard, L., Willmer, C. N. A., Gebhardt, K., Bouwens, R. J., Kauffmann, G., Crosby, T., Faber, S. M., Harker, J., Sarajedini, V. L., Vogt, N. P., Weiner, B. J., Phillips, A. J., Im, M., & Wu, K. L. 2005, ApJS, 157, 175

Kormendy, J. 1993, in IAU Symposium, Vol. 153, Galactic Bulges, ed. H. Dejonghe & H. J. Habing, 209–+

Kormendy, J. & Kennicutt, Jr., R. C. 2004, ARA&A, 42, 603

Kronberger, T., Kapferer, W., Ferrari, C., Unterguggenberger, S., & Schindler, S. 2008, A&A, 481, 337

Kuntschner, H., Emsellem, E., Bacon, R., Bureau, M., Cappellari, M., Davies, R. L., de Zeeuw, P. T., Falcón-Barroso, J., Krajnović, D., McDermid, R. M., Peletier, R. F., & Sarzi, M. 2006, MNRAS, 369, 497

Kuntschner, H., Smith, R. J., Colless, M., Davies, R. L., Kaldare, R., & Vazdekis, A. 2002, MNRAS, 337, 172

Laurikainen, E., Salo, H., & Buta, R. 2005, MNRAS, 362, 1319

Lee, H.-c., Worthey, G., Trager, S. C., & Faber, S. M. 2007, ApJ, 664, 215

MacArthur, L. A. 2005, ApJ, 623, 795

MacArthur, L. A., Courteau, S., Bell, E., & Holtzman, J. A. 2004, ApJS, 152, 175

MacArthur, L. A., Courteau, S., & Holtzman, J. A. 2003, ApJ, 582, 689

MacArthur, L. A., González, J. J., & Courteau, S. 2009, MNRAS, 395, 28

Maoz, D., Barth, A. J., Ho, L. C., Sternberg, A., & Filippenko, A. V. 2001, AJ, 121, 3048

Maraston, C. 2005, MNRAS, 362, 799

Marigo, P. & Girardi, L. 2007, A&A, 469, 239

McDonald, M., Courteau, S., & Tully, R. B. 2009a, ApJ, in preparation (M09)

—. 2009b, MNRAS, 394, 2022

Mehlert, D., Thomas, D., Saglia, R. P., Bender, R., & Wegner, G. 2003, A&A, 407, 423

Mihos, J. C. & Hernquist, L. 1996, ApJ, 464, 641

Moore, B., Katz, N., Lake, G., Dressler, A., & Oemler, A. 1996, Nature, 379, 613

Navarro, J. F., Frenk, C. S., & White, S. D. M. 1995, MNRAS, 275, 56

Neistein, E., van den Bosch, F. C., & Dekel, A. 2006, MNRAS, 372, 933

Nelan, J. E., Smith, R. J., Hudson, M. J., Wegner, G. A., Lucey, J. R., Moore, S. A. W., Quinney, S. J., & Suntzeff, N. B. 2005, ApJ, 632, 137

Nilson, P. 1973, Uppsala general catalogue of galaxies, ed. P. Nilson

Noordermeer, E. & van der Hulst, J. M. 2007, MNRAS, 376, 1480

Norris, M. A., Sharples, R. M., & Kuntschner, H. 2006, MNRAS, 367, 815

Peletier, R. F. & Balcells, M. 1996, AJ, 111, 2238

Peletier, R. F., Balcells, M., Davies, R. L., Andredakis, Y., Vazdekis, A., Burkert, A., & Prada, F. 1999, MNRAS, 310, 703

Pfenniger, D. & Friedli, D. 1991, A&A, 252, 75

Pfenniger, D. & Norman, C. 1990, ApJ, 363, 391

Poggianti, B. M., Bridges, T. J., Carter, D., Mobasher, B., Doi, M., Iye, M., Kashikawa, N., Komiyama, Y., Okamura, S., Sekiguchi, M., Shimasaku, K., Yagi, M., & Yasuda, N. 2001, ApJ, 563, 118

Portinari, L., Sommer-Larsen, J., & Tantalo, R. 2004, MNRAS, 347, 691

Postman, M., Franx, M., Cross, N. J. G., Holden, B., Ford, H. C., Illingworth, G. D., Goto, T., Demarco, R., Rosati, P., Blakeslee, J. P., Tran, K.-V., Benítez, N., Clampin, M., Hartig, G. F., Homeier, N., Ardila, D. R., Bartko, F., Bouwens, R. J., Bradley, L. D., Broadhurst, T. J., Brown, R. A., Burrows, C. J., Cheng, E. S., Feldman, P. D., Golimowski, D. A., Gronwall, C., Infante, L., Kimble, R. A., Krist, J. E., Lesser, M. P., Martel, A. R., Mei, S., Menanteau, F., Meurer, G. R., Miley, G. K., Motta, V., Sirianni, M., Sparks, W. B., Tran, H. D., Tsvetanov, Z. I., White, R. L., & Zheng, W. 2005, ApJ, 623, 721

Press, W. H., Teukolsky, S. A., Vetterling, W. T., & Flannery, B. P. 1992, Numerical recipes in FORTRAN. The art of scientific computing, ed. W. H. Press, S. A. Teukolsky, W. T. Vetterling, & B. P. Flannery

Quilis, V., Moore, B., & Bower, R. 2000, Science, 288, 1617

Rickes, M. G., Pastoriza, M. G., & Bonatto, C. 2009, ArXiv e-prints

Roškar, R., Debattista, V. P., Stinson, G. S., Quinn, T. R., Kaufmann, T., & Wadsley, J. 2008, ApJ, 675, L65

Sánchez-Blázquez, P., Forbes, D. A., Strader, J., Brodie, J., & Proctor, R. 2007, MNRAS, 377, 759

Scannapieco, C. & Tissera, P. B. 2003, MNRAS, 338, 880

Schade, D., Lilly, S. J., Crampton, D., Ellis, R. S., Le Fèvre, O., Hammer, F., Brinchmann, J., Abraham, R., Colless, M., Glazebrook, K., Tresse, L., & Broadhurst, T. 1999, ApJ, 525, 31

Schiavon, R. P., Faber, S. M., Rose, J. A., & Castilho, B. V. 2002, ApJ, 580, 873

Schlegel, D. J., Finkbeiner, D. P., & Davis, M. 1998, ApJ, 500, 525

Sellwood, J. A. 1981, A&A, 99, 362

Serra, P., Trager, S. C., Oosterloo, T. A., & Morganti, R. 2008, A&A, 483, 57

Sersic, J. L. 1968, Atlas de galaxias australes, ed. J. L. Sersic

Shapley, A. E., Steidel, C. C., Erb, D. K., Reddy, N. A., Adelberger, K. L., Pettini, M., Barmby, P., & Huang, J. 2005, ApJ, 626, 698

Sil'chenko, O. K. 2006, ApJ, 641, 229

Skrutskie, M. F., Cutri, R. M., Stiening, R., Weinberg, M. D., Schneider, S., Carpenter, J. M., Beichman, C., Capps, R., Chester, T., Elias, J., Huchra, J., Liebert, J., Lonsdale, C., Monet, D. G., Price, S., Seitzer, P., Jarrett, T., Kirkpatrick, J. D., Gizis, J. E., Howard, E., Evans, T., Fowler, J., Fullmer, L., Hurt, R., Light, R., Kopan, E. L., Marsh, K. A., McCallon, H. L., Tam, R., Van Dyk, S., & Wheelock, S. 2006, AJ, 131, 1163

Steinmetz, M. & Navarro, J. F. 2002, New Astronomy, 7, 155

Strateva, I., Ivezić, Ž., Knapp, G. R., Narayanan, V. K., Strauss, M. A., Gunn, J. E., Lupton, R. H., Schlegel, D., Bahcall, N. A., Brinkmann, J., Brunner, R. J., Budavári, T., Csabai, I., Castander, F. J., Doi, M., Fukugita, M., Győry, Z., Hamabe, M., Hennessy, G., Ichikawa, T., Kunszt, P. Z., Lamb, D. Q., McKay, T. A., Okamura, S., Racusin, J., Sekiguchi, M., Schneider, D. P., Shimasaku, K., & York, D. 2001, AJ, 122, 1861

Tamura, N. & Ohta, K. 2003, AJ, 126, 596

Taylor, V. A., Jansen, R. A., Windhorst, R. A., Odewahn, S. C., & Hibbard, J. E. 2005, ApJ, 630, 784

Thomas, D., Maraston, C., Bender, R., & Mendes de Oliveira, C. 2005, ApJ, 621, 673

Tikhonov, N. A., Galazutdinova, O. A., & Aparicio, A. 2003, A&A, 401, 863

Tonini, C., Maraston, C., Devriendt, J., Thomas, D., & Silk, J. 2009, MNRAS, 396, L36

Trager, S. C., Faber, S. M., Worthey, G., & González, J. J. 2000, AJ, 119, 1645

Tremonti, C. A., Heckman, T. M., Kauffmann, G., Brinchmann, J., Charlot, S., White, S. D. M., Seibert, M., Peng, E. W., Schlegel, D. J., Uomoto, A., Fukugita, M., & Brinkmann, J. 2004, ApJ, 613, 898

van den Bergh, S. 1994, AJ, 107, 153

Vazdekis, A. 1999, ApJ, 513, 224

Vazdekis, A., Casuso, E., Peletier, R. F., & Beckman, J. E. 1996, ApJS, 106, 307

Virani, S. N., De Robertis, M. M., & VanDalfsen, M. L. 2000, AJ, 120, 1739

Weinzirl, T., Jogee, S., Khochfar, S., Burkert, A., & Kormendy, J. 2009, ApJ, 696, 411

White, S. D. M. & Rees, M. J. 1978, MNRAS, 183, 341

Wiklind, T. & Henkel, C. 2001, A&A, 375, 797

Worthey, G. 1994, ApJS, 95, 107

York, D. G., Adelman, J., Anderson, Jr., J. E., Anderson, S. F., Annis, J., Bahcall, N. A., Bakken, J. A., Barkhouser, R., Bastian, S., Berman, E., Boroski, W. N., Bracker, S., Briegel, C., Briggs, J. W., Brinkmann, J., Brunner, R., Burles, S., Carey, L., Carr, M. A., Castander, F. J., Chen, B., Colestock, P. L., Connolly, A. J., Crocker, J. H., Csabai, I., Czarapata, P. C., Davis, J. E., Doi, M., Dombeck, T., Eisenstein, D., Ellman, N., Elms, B. R., Evans, M. L., Fan, X., Federwitz, G. R., Fiscelli, L., Friedman, S., Frieman, J. A., Fukugita, M., Gillespie, B., Gunn, J. E., Gurbani, V. K., de Haas, E., Haldeman, M., Harris, F. H., Hayes, J., Heckman, T. M., Hennessy, G. S., Hindsley, R. B., Holm, S., Holmgren, D. J., Huang, C.-h., Hull, C., Husby, D., Ichikawa, S.-I., Ichikawa, T., Ivezić, Ž., Kent, S., Kim, R. S. J., Kinney, E., Klaene, M., Kleinman, A. N., Kleinman, S., Knapp, G. R., Korienek, J., Kron, R. G., Kunszt, P. Z., Lamb, D. Q., Lee, B., Leger, R. F., Limmongkol, S., Lindenmeyer, C., Long, D. C., Loomis, C., Loveday, J., Lucinio, R., Lupton, R. H., MacKinnon, B., Mannery, E. J., Mantsch, P. M., Margon, B., McGehee, P., McKay, T. A., Meiksin, A., Merelli, A., Monet, D. G., Munn, J. A., Narayanan, V. K., Nash, T., Neilsen, E., Neswold, R., Newberg, H. J., Nichol, R. C., Nicinski, T., Nonino, M., Okada, N., Okamura, S., Ostriker, J. P., Owen, R., Pauls, A. G., Peoples, J., Peterson, R. L., Petravick, D., Pier, J. R., Pope, A., Pordes, R., Prosapio, A., Rechenmacher, R., Quinn, T. R., Richards, G. T., Richmond, M. W., Rivetta, C. H., Rockosi, C. M., Ruthmansdorfer, K., Sandford, D., Schlegel, D. J., Schneider, D. P., Sekiguchi, M., Sergey, G., Shimasaku, K., Siegmund, W. A., Smee, S., Smith, J. A., Snedden, S., Stone, R., Stoughton, C., Strauss, M. A., Stubbs, C., SubbaRao, M., Szalay, A. S., Szapudi, I., Szokoly, G. P., Thakar, A. R., Tremonti, C., Tucker, D. L., Uomoto, A., Vanden Berk, D., Vogeley, M. S., Waddell, P., Wang, S.-i., Watanabe, M., Weinberg, D. H., Yanny, B., & Yasuda, N. 2000, AJ, 120, 1579